



UNIVERSIDAD MICHOACANA DE SAN NICOLÁS DE  
HIDALGO

---

---

INSTITUTO DE FÍSICA Y MATEMÁTICAS

ANÁLISIS DE LAS DISTRIBUCIONES  
LATERALES DE CHUBASCOS DE RAYOS  
CÓSMICOS CON HAWC

TESIS

QUE PARA OBTENER EL TÍTULO DE:  
**Maestro en Ciencias en el área de Física**

PRESENTA:

**Jorge Antonio Morales Soto**

DIRECTOR DEL TRABAJO:

**Dr. Juan Carlos Arteaga Velázquez**

Morelia, Michoacán, Agosto del 2019



## Resumen

Cuando un rayo cósmico interacciona con las moléculas de la atmósfera este produce una cascada o chubasco de partículas secundarias que se pueden detectar a nivel del suelo por medio de diferentes técnicas de detección, por ejemplo, usando redes de detectores de partículas, telescopios de fluorescencia o de aire Cherenkov. La distribución lateral de las partículas secundarias de un chubasco a nivel del suelo (LDF, por sus siglas en inglés) contiene información sobre la naturaleza del rayo cósmico primario, así como de su energía. Los estudios de la distribución lateral son difíciles de llevar a cabo debido a incertidumbres experimentales o fluctuaciones en el desarrollo del chubasco. El observatorio de rayos gamma HAWC es un arreglo denso de detectores de partículas ubicado en Puebla, México a 4,100 m s.n.m. dedicado al estudio de rayos cósmicos y rayos gamma. El detector está equipado con 1,200 fotomultiplicadores los cuales se encuentran distribuidos dentro de 300 detectores de agua Cherenkov, que en conjunto contienen un total de 60 ML de agua. HAWC tiene la capacidad de llevar a cabo mediciones detalladas, evento por evento, de la distribución lateral de chubascos de partículas con energías de varios TeV. En este trabajo se presenta un estudio sobre la distribución lateral de chubascos inducidos por rayos cósmicos medidos por HAWC en el año 2016 con energías entre 3 TeV y 1 PeV y ángulo cenital  $< 16.7^\circ$ . Los datos fueron usados para determinar la óptima parametrización de la distribución lateral en HAWC. De aquí el parámetro de edad es obtenido y su sensibilidad a la composición de los rayos cósmicos es analizada.

**Palabras clave:** HAWC, distribución lateral, rayos cósmicos, edad lateral, composición primaria.

## Abstract

When a cosmic ray hits the molecules of the atmosphere it produces a shower of secondary particles that can be detected at ground level through different detection techniques, such as particle detector arrays, and fluorescence or air Cherenkov telescopes. The lateral distribution of particles around the shower axis (LDF) at ground level posses information about the mass composition and primary energy of cosmic rays. Studies of the LDF are difficult to perform due to experimental uncertainties and fluctuations in the development of the air shower. The High Altitude Water Cherenkov (HAWC) observatory is a dense air-shower array located in Puebla, Mexico at 4100 m a.s.l. and it is dedicated to the study of cosmic- and gamma-rays. The detector is instrumented with 1,200 photomultipliers (PMTs) distributed in 300 close-packed water Cherenkov tanks, which in total contain a total of 60 ML of water. Due to its design, HAWC is well-suited to perform detailed event-by-event studies of the LDF of multi-TeV cosmic-ray showers. We present a study of the LDF of cosmic-ray air showers recorded by HAWC in 2016 with energies between 3 TeV and 300 TeV and zenith angle  $< 16.7^\circ$ . The data are used to determine the optimal parameterization of the LDF of the HAWC data. From here the lateral shower age is obtained and its sensitivity to the cosmic ray mass composition is analyzed. **Key words:** HAWC, lateral distribution, cosmic

rays, lateral age, primary composition.

A mi papá y a mi mamá,  
mi abuelita,  
mi familia,  
y mi segunda familia: mis amigos.

## Agradecimientos

Quiero agradecer en especial a mis papás por todo el apoyo brindado, su infinita paciencia y esfuerzo. Se que no ha sido fácil para ninguno de ustedes y siempre estaré agradecido por todo lo que me han dado. Todo lo que soy se los debo a ustedes.

Un agradecimiento especial a mi asesor, Juan Carlos Arteaga Velázquez, por el conocimiento brindado, el apoyo y la paciencia. También a Juan de Dios, gracias por el apoyo y la amistad.

A mis amigos que siempre me ah acompañado y apoyado: Atziri, Manolo, Dulcesito de mi alma, Fanita, Lari, Paquito, Kim, Prima, Naila y Bosco (y bebé), el amigo Isaac, Ariana, Leti y Gaby Fismat (aunque te enojas, Gaby Fismat). Y los que llevan aún más tiempo aguantándome: Mis hermanos del alma Nestor y Abraham, y Zianya (me debes unos tacos). Y obviamente no podían faltar Erick, Sebastian y Zhava, que el D&D nunca termine.

a mi segunda familia, mis amigos del IFM: Santi, Venecia, Sofi, Memo, Gonzalo, Misha, Gaby, Richi, César, Rube, mis amiguitos del alma Juan e Izamar, David, Pancho, Chucho, Anabel, Gabs (aunque eres fismat aún), Melanie, Mike. Amigues, los quiero mucho y les deso mucho éxito a cada uno de ustedes. Y en especial, gracias a mi compañera de cubo, Itzayana, aunque me saques canas nuevas cada 5 minutos, me acompañaes por chololates a la tienda y te quiera muy poquito.

Ceci y Teté, mil gracias por todo. Yo las canciones y ustedes la magia.

Por último, quiero agradecer a CONACYT por el apoyo brindado y a la colaboración de HAWC.

# Contents

<b>1</b>	<b>Cosmic Rays</b>	<b>1</b>
1.1	Historical introduction . . . . .	1
1.2	Brief historical review of cosmic ray research . . . . .	9
1.3	Cosmic rays . . . . .	10
1.3.1	Primary spectrum of cosmic rays . . . . .	12
1.3.2	Cosmic ray primary composition . . . . .	14
1.3.3	Sources . . . . .	15
1.3.4	Primary acceleration of cosmic rays . . . . .	16
<b>2</b>	<b>Extensive air showers</b>	<b>21</b>
2.1	Discovery of Extensive Air Showers . . . . .	21
2.2	Hadronic component . . . . .	23
2.3	Electromagnetic component . . . . .	23
2.4	Muonic component . . . . .	23
2.5	Heitler Model . . . . .	24
2.5.1	Heitler model for electromagnetic showers . . . . .	24
2.5.2	Heitler model for hadronic showers . . . . .	26
2.6	Hadronic interaction models . . . . .	27
2.7	Reconstruction of an air shower . . . . .	28
2.7.1	Arrival direction . . . . .	28
2.7.2	Shower core . . . . .	28
2.7.3	Shower age (s) . . . . .	28
<b>3</b>	<b>Detection methods of Cosmic Rays</b>	<b>32</b>
3.1	Direct measurements . . . . .	32
3.2	Indirect measurements . . . . .	33
3.2.1	ARGO-YBJ . . . . .	35
3.2.2	KASCADE . . . . .	37
3.2.3	TAIGA . . . . .	39
3.2.4	Observatories in process of upgrading . . . . .	40
<b>4</b>	<b>HAWC Observatory</b>	<b>43</b>
4.1	Science goals . . . . .	43
4.2	The HAWC detector . . . . .	46
4.3	Cherenkov Radiation . . . . .	48
4.4	Photomultiplier tubes, PMTs . . . . .	49

4.4.1	Data Acquisition System . . . . .	50
4.5	Air shower reconstruction . . . . .	51
4.5.1	Core position . . . . .	51
4.5.2	Arrival direction . . . . .	53
4.5.3	Age parameter, $s$ . . . . .	54
4.5.4	Energy reconstruction . . . . .	55
4.5.5	Simulation . . . . .	55
4.5.6	Simulated data . . . . .	56
4.5.7	Observables . . . . .	56
4.5.8	Gamma/Hadron separation . . . . .	61
4.5.9	Quality cuts . . . . .	62
4.6	Systematic errors . . . . .	62
4.6.1	Angular bias and resolution . . . . .	63
4.6.2	Energy bias and resolution . . . . .	63
4.6.3	Core position bias and resolution . . . . .	63
4.7	Experimental data . . . . .	65
<b>5</b>	<b>Analysis method of the lateral distribution of cosmic-ray induced showers</b>	<b>67</b>
5.1	Reconstruction of the lateral distribution of EAS in HAWC . . . . .	68
5.2	Parameterizing the LDF of cosmic-ray induced extensive air showers . . . . .	70
5.3	Description of the Analysis . . . . .	72
5.3.1	Fit of the lateral distribution of air showers . . . . .	72
5.3.2	Predicted lateral age parameter . . . . .	74
<b>6</b>	<b>Experimental analyses, results and discussion</b>	<b>78</b>
6.1	Study of the shape of the lateral distribution of EAS measured at HAWC . . . . .	78
6.2	Analysis of the age of air showers and primary composition . . . . .	78
6.3	PINCness . . . . .	82
6.4	Comparison of LDF data with model predictions . . . . .	82
6.5	Discussion . . . . .	85
6.5.1	Parameterization of the lateral distribution of EAS induced by cosmic rays . . . . .	85
6.5.2	Dependence of the age parameter on the parameterization of the LDF . . . . .	89
6.5.3	Study of the sensitivity of the age parameter to the composition of cosmic rays . . . . .	90
6.5.4	Analysis of PINCness as a mass composition parameter . . . . .	90
6.5.5	Test of the predictions of the QGSJET-II-03 hadronic interaction model using the $Q_{eff}(r)$ data . . . . .	91
6.5.6	Dependence of the anomaly in the shower age on the $Q_{eff}$ data close to the EAS core region and with large values . . . . .	91
<b>7</b>	<b>Conclusions</b>	<b>92</b>
	<b>Bibliography</b>	<b>93</b>

# Chapter 1

## Cosmic Rays

*“What I do is very theoretical. It won't necessarily have implications for anything anyone is doing tomorrow, yet you know that there's a sense of progress in science, and as we understand more, it just turns out that, somehow, the world evolves with us.”*

-Lisa Randall.

### 1.1 Historical introduction

The story of the discovery of the ionizing radiation coming from outer space seems to begin in the XVIII century, when Charles-Augustin de Coulomb studied the discharge of metallic conducting bodies [1, 2]. Coulomb observed that the charged body could lose its charge even when it was isolated from its surroundings. Many scientists after him tried to understand this outcome and, with the discovery of radiation in the XIX century, new theories came to light with the purpose of explaining this phenomenon.

On 1887 Sir Charles Vernon Boys, while performing studies on the isolating properties of different materials such as glass, observed the discharge of two very narrow gold electrically charged leaves that were hanging from an isolating support (see fig. 1.1). Isolated or not, the loss of charge of the pair of golden leaves was observed, and he concluded that this effect was due to convection through the air [3].

In the XIX century, the experimental devices employed for the measurement of charged bodies were not sophisticated enough and were a source of uncertainties between the experimental observations. Therefore, the development of more refined tools was needed to satisfy the necessities of the experimental research of the charge bodies phenomenon.

One of the most useful tools that was used in the past for the study of the discharge of electric bodies was the electroscope. The electroscope is a simple device that allows to detect the electric charge in a body, to measure the sign of the charge (positive or negative), and to determine its value with a certain degree of uncertainty. The simplest model of an electroscope is a glass recipient (or a case with glass walls) which contains a pair of metallic leaves hanging from a metallic rod that goes out of the recipient, being insulated from it (see fig. 1.2). The main charge loss of the metallic leaves occurs mainly through out the insulating sleeve that separates the metallic rod from the case. The loss of charge can be reduced almost to zero with a proper design of the electroscope, but even in this case it will

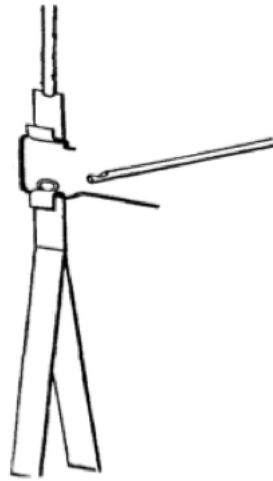


Figure 1.1: Charles Boy's experimental arrangement. The golden leaves (that separate from each other when they are charged) hang from a bent piece of glass (or quartz). *Image source:* [3].

not hold the electric charge for indefinite time.

By the end of the XIX century, the conductivity of the air was subject of study by the scientific community. Physicists like C. T. R. Wilson, H. F. Geitel and J. Elster joined to this effort. In that time it was already known that matter was made of atoms and that each chemical element is represented by a different atom, which posses the same number of positive and negative charges, making the atom neutral. Hence, the charge loss of an electroscope was explained by the fact that the air or gas that surrounds the metallic plates is always slightly ionized, which means that the gas losses its neutral nature. A molecule from the gas that looses an electron remains with a positive charge excess, while the electron may stay free or may attach to another molecule giving it a negative charge. Therefore, inside of the gas there is a small fraction of free electrons and charged molecules, which are called *ions*. Now, if the plates of the electroscope have a positive induced charge, they attract negative ions and the positive charge of the plates is gradually neutralized until the plates go back to its original position. In a similar way, if the plates have a negative charge, they will attract positive ions which ends up in with the discharge of the plates. As expected, several experiments were proposed and carried out in the effort to understand the nature of the discharge phenomenon inside the electroscope due to the air (or gas) ionization.

At the end of the XIX century, J. Elster and H. F. Geitel, in a series of experiments with a device named *Zerstreuungssapparat* (see fig. 1.3), measured the leakage of electricity in the atmosphere (in fact, what this instrument was measuring is the conductivity of air). With their results, they concluded that air conducts electricity and that the atmospheric air is slightly ionized. Later in 1901, they found that radiation causes the ionization of the air [5]. How did the radioactive material get into the air? Elster and Geitel stated that this radioactive material is emanated from Earth's surface in form of gas and it is the main source of air's ionization [2, 5].

If the radiation has its origins on Earth's surface, then its effect should be stronger near the



Figure 1.2: A model of an electrostatic balance similar to the ones used at the end of the XIX century. *Image source* [4].

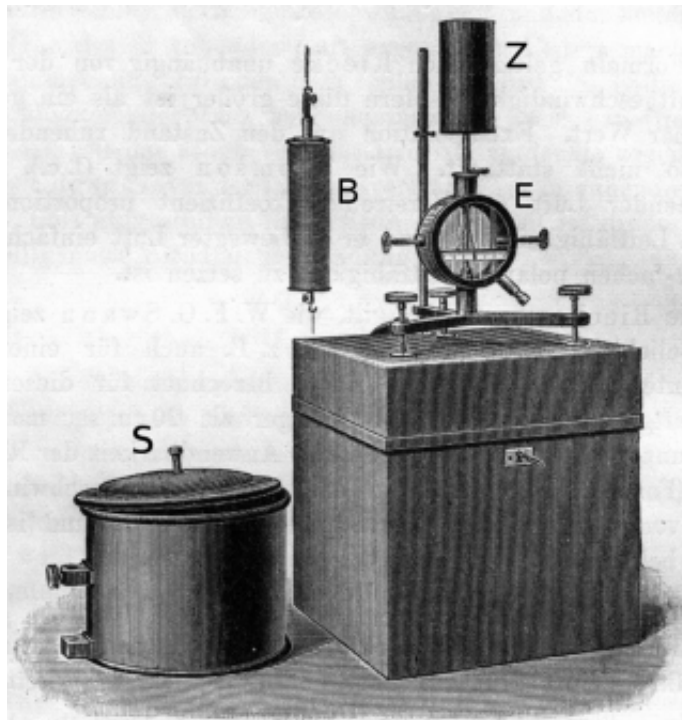


Figure 1.3: Dispersion instrument (*Zerstreuungsapparat*) used by J. Elster and H. F. Geitel in their experiments of air conductivity. *Image source*: [5].

ground and should decrease gradually by increasing the height. It should be easy to prove this hypothesis with measurements of radioactivity at different heights so, in order to prove it, many experiments were carried out, but the results were contradictory. Hermann Ebert was probably the first person to perform an air balloon flight with the aim to measure the electrical charge loss in a charged body at different altitudes [2]. He carried out a

total of three air balloon flights (on June and November of 1900 and January 1901) reaching a maximum altitude of 3,700 m. He found a change in the loss of charge of the charged body in relation with the altitude and he also observed that his measurements depended of climatological conditions.

In 1906, Heinrich Mache and Travis Rimmer studied the intensity of the penetration of the ionizing radiation and discovered that its intensity varied through out the day and depended of climatological conditions [2]. After that, in 1908, Mache concluded that the penetrating radiation was made by two parts: one part coming from chemical elements found on Earth's surface and the other part, from the decay of chemical elements that are distributed on the atmosphere [2]. By that time, scientist believed that the radiation could be explained in terms of gamma rays emitted by radioactive elements. This idea was based on the fact that gamma-rays were the most penetrating type of radiation known at the time<sup>1</sup>.

In 1907, Arthur Steward Eve speculated that the ionization over the ocean (5%) should be less than over the soil (95%), because in the sea waters the radium (radioactive element liberated from the surface of the Earth in form of gas) was present to a markedly less degree than in the sedimentary rocks on land. Also it was expected that the radiation would be attenuated in the air. The attenuation can be estimated with a very fast calculation, let's say that for an altitude of  $h = 300$  m:

$$\frac{I(h)}{I_0} = e^{-h/\lambda} = e^{-300m/98m} = 0.03, \quad (1.1)$$

where  $I(h)$  is the intensity of the transmitted radiation after crossing a distance  $h$ ,  $I_0$  is the initial intensity of the radiation and  $\lambda$  is the mean interaction length for  $\gamma$ -rays in air. The result of eq. (1.1) predicts that only 3% of the initial radiation on the ground remains at an altitude of 300 m a.s.l., which means that the radiation from the soil is almost fully attenuated.

Albert Gockel was a German physicist who spent most of his professional career in the study of atmospheric conductivity phenomena as a researcher at the Institute of Physics of the Freiburg University, Switzerland. Due to the tense relation with the head master of the Institute, Joseph de Kowalski, Gockel's research often found strong opposition and lack of funds<sup>2</sup> [6]. Due to the financial problems that Gockel faced, he didn't had access to the best technology and instruments available at the time, and that was reflected on most of his research.

On December 11 of 1909, funded by the East section of the Swiss Aeroclub, Albert Gockel performed the first of three air balloon flights to measure the ion density in the atmosphere reaching an altitude of 4,500 m after more than four hours of flight. At the beginning, Gockel's measurements showed a decrease of the ionizing radiation with altitude, as expected from the hypothesis of a terrestrial origin of the radiation, but at a smaller rate than predicted, and at higher altitudes Gockel recorded an increase of the radiation [7]. Gockel used a standard setup of Wulf's electrometer (see fig. 1.4) coupled to an ionization chamber [6] and he stated that due to the flight conditions he couldn't rule out instruments malfunctioning that could possibly spoiled his results. Gockel reported that "the results of

---

<sup>1</sup>In fact, back in 1929 the German literature still referred to cosmic rays as *Ultragammasstrahlung* [2].

<sup>2</sup>For more information on this topic see R. Cantinaud, Which physics for a new institute? Albert Gockel, Joseph Kowalski and the early years of the Fribourg Institute Of Physics, Communications of the Swiss Physical Society, nr 36, 2012, 24-27.

the measurements are thus that in free atmosphere there occurs indeed a decrease of the penetrating radiation, but by far not to the extent that one should expect if the radiation originated mainly from ground" [8]. As of the increase of the radiation at higher altitudes he concluded that these results shouldn't be considered as reliable due to possible malfunctions on the instruments at high altitudes [6].

On his second flight (October 15th, 1910), Albert Gockel intended to fill his balloon, the *Gotthard*, with hydrogen-gas instead of coal-gas with the aim to reach altitudes up to 7,000 m a.s.l., but due to funding reasons this wasn't possible. Despite the difficulties, Gockel performed his second flight and reached altitudes up to 2 km and the results of his second flight were in agreement with the measurements of his first flight. With this, Gockel had no doubts about the results and stated that "An influence of the altitude on the ionisation in the closed vessels was not seen. It can be concluded that a cosmic radiation, if it exists at all, can only be a negligible part of the penetrating radiation", were it is noticeable that he introduced the term *cosmic radiation (kosmische strahlung)* [9].

On the other hand, the Jesuit priest Theodor Wulf developed a more sophisticated electro-scope (see fig. 1.4) in the spirit to unveil the origin of the ionizing radiation in the air to prove the hypothesis of H. Ebert and A. Gockel that if the radiation comes from the Earth, then it should decrease with height. In 1910, Wulf made a series of measurements at the top of the Eiffel tower (330 m height) in Paris, France, to proof the hypothesis, but his observations led him to a different result [10]. Wulf's results showed that the radiation decreased nearly to half its value on the surface, which was not expected under the hypothesis of a terrestrial origin of the ionizing radiation. Even though, Wulf's results were considered the most reliable ones at the time because the measurements were performed with sophisticated instruments and at fixed altitudes and locations.

Not far from France and around the same time, between 1907 and 1912, Domenico Pacini was performing measurements of air conductivity on the ground, on the ocean on board of the Royal military ship *Folgore* and deep in the ocean in Italy. With his measurements he discovered that the intensity of the ionizing radiation was the same than that observed at land. Pacini repeated his measurements at the Bracciano lake, near Rome, where he also performed measurements under water, stating that the radiation was absorbed by water. He speculated about the causes of the ionization, proposing another source other than the outer layers of Earth's crust, suggesting an independent source present in the air [11].

The results of Gockel, Wulf and Pacini were the first evidences that the ionizing radiation was independent from the radioactive elements present in Earth's crust, and suggested that its origin was outside of Earth's atmosphere.

The austrian physicist Victor F. Hess studied Wulf's results and the coefficients of absorption for gamma-ray radioactivity in the atmosphere proposed by Eve to study the causes of air ionization. Hess found discrepancies between the theoretical predictions and the experimental data. Hess, an air balloon flight amateur, decided to continue his studies using balloon observations and he performed ten air balloon flights (most of them at night) with *two Wulf radiation detectors with three-millimeter thick walls, perfectly sealed and able to withstand all pressure variations during the ascents, for the observation of the penetrating radiation* [12]. In 1912, Hess did seven air balloon flights from which two of them were of great importance (see fig. 1.5). The first of these two flights was performed during a Sun eclipse, on April 17th, between 11 a.m. and 1 p.m. up to an altitude of 2,750 m. As T. Wulf found, Hess observed that near the ground the intensity of the radiation decreases and



Figure 1.4: Wulf's electroscop. The instrument mainly consisted on a pair of quartz fibbers attached at the bottom to a bend quartz fibber. The distance of the two fibbers is measured through a microscope. The company Günther & Tegetmeyer was in charge of manufacturing Wulf's electroscopes [10]. *Image source:* <https://commons.wikimedia.org/wiki/File:Originalwulf.jpeg>.

he also discovered that the radiation near 2,000 m height was greater than the radiation at sea level and the result was independent from the eclipse. Therefore, the Sun was ruled out as the main source of this radiation, suggesting that its origin was outside our solar system (although, nowadays it is known that there are cosmic rays of low energy coming from the Sun). The second flight took place in the morning of August 7 at 6 a.m., with a flight duration of approximately 6 hours and a maximum altitude of around 5,3000 m. The results of this flight (combined with his previous results) led him to the conclusion that the ionization increases significantly with altitude. On the other hand, his results from all the flights didn't show a difference between night and day [12–15]. After his 7th balloon flight Hess concluded [12]: *The results of the present observations seem most likely to be explained by the assumption that radiation of very high penetrating power enters from above into our atmosphere, and even in its lowest layers causes part of the ionization observed in closed vessels.*<sup>3</sup>

Victor Hess was awarded the Nobel prize in 1936 thanks to his ground breaking studies on cosmic radiation.

The German physicist Werner Kolhörster confirmed Hess's results about the increase in air ionization at higher altitudes by performing air balloon flights up to 9,300 m a. s. l. [18]. In the late 20's, the development of new instruments allowed to reach a better quality on the results, achieving important progress in the experimental study of cosmic rays.

Robert Andrews Millikan (see fig. 1.6) was a detractor from the hypothesis that the radia-

---

<sup>3</sup>A full translation to the English of Hess' article [12] can be found at [16]



Figure 1.5: Victor Hess before the departing of one of his flights in 1911 or 1912. *Image source:* [17].

tion had an extraterrestrial origin and he assumed that it had its origin on the radioactive substances present in the air. Millikan decided to corroborate the results reported by Victor Hess and W. Kolhöster. For this purpose, Millikan and his colleague H. Cameron positioned electroscopes at different depths inside water with the purpose of measuring the intensity of cosmic rays as a function of depth in water and at different altitudes to check whether the ionizing radiation was produced in air. The selected locations were the Mauir Lake (3,540 m a.s.l.) near the top of Mt. Whitney, and Lake Arrowhead (1,530 m a.s.l.) in Southern California. As the electroscopes were placed at large depths up to 27 m, they found a continuous decrease of the discharge rate of the electroscopes [2], from which they concluded that *within the limits of observational error, every reading in Arrowhead lake corresponded to a reading 6 feet (1.8 m) farther down in Muir Lake, thus showing that the rays do come in definitely from above, and that their origin is entirely outside the layer of atmosphere between the levels of the two lakes* [19]. As a conclusion of their results, A. Millikan was convinced about the existence of an extraterrestrial radiation and coined the term *cosmic rays* [20]

On July 7th, 1928, Hans W. Geiger and his student William Müller announced the creation of a radiation counting tube, which was used by many scientists in the studies of air's ionization measurements and in coincidence counting devices. Bruno Rossi described this instrument as *an open window to a new and unknown territory, with unlimited opportunities for exploration* [22, 23]. Bruno Rossi was an Italian physicist known for his research and experimental work on astrophysics and cosmic ray physics, specially on the study of the nature and behaviour of the cosmic radiation. Among his different contributions to the field, we found the discovery of the existence of two components in cosmic-ray radiation at sea level: the *hard* component (composed by muons), which is able to pass through 1 meter of lead, and the *soft* component (composed by electrons, positrons and gamma-rays), which is



Figure 1.6: Robert Andrews Millikan (1868 - 1953) [21].

generated high in the atmosphere by primary cosmic rays and can be stopped by a metal screen. It also generates groups of particles as it goes through a 10 cm thick lead screen [22]. On July 3rd, 1930, Rossi conjectured the existence of a geomagnetic effect on cosmic rays that would be observed as an increase in the incoming flux of positive charged particles from West to East and vice-versa if negative particles were more abundant on cosmic rays. Rossi's experiments about the East-West effect were delayed due to funding problems [22]. But Arthur Compton and Louis Alvarez [24], and Thomas Johnson [25] published results independently confirming Rossi's hypothesis of a geomagnetic effect on cosmic rays, and by doing so they discovered that cosmic rays are mainly positively charged.

On the autumn of 1933, Rossi performed experiments using coincidence counters in Eritrea<sup>4</sup>, a former Italian colony on Africa, where he observed the existence of *very extensive showers of particles*.

In 1938, W. Kolhöster reported the observation of a *Schauer* (shower) of secondary particles that were responsible of the coincidence between two particle counters separated by approximately 10 m. Later in 1938, Pierre Auger and his team started a study on the two components of cosmic rays proposed by Rossi (without knowing about his conclusions about the secondary particle showers), which turned into the rediscovery of extensive air showers [26]. Auger also used an array of coincidence counters for his studies of particle showers. At first the counters were separated from each other by tens of meters and they were progressively set wide apart in order to study more dispersed showers. Auger and his team speculated that these showers must be produced high in the atmosphere, that its branches could be separated by distances of several meters, and that the showers could cover surfaces of the order of 1,000 m<sup>2</sup> at ground level.

The credit for the discovery of the extensive air showers (EAS) was given to Auger and his collaborators. The discovery of the EAS opened a new window to the study of cosmic rays of PeV energies and above, giving birth to new theories about the origin of these energetic particles, which still remains as an open question nowadays [**RadioactivityBook**].

It is difficult to cover all of the history and relevant characters that played key roles on the

---

<sup>4</sup>At an altitude of 2,370 m and a geomagnetic latitude of 11° 30' N.

development of the theory and the experimental designs for cosmic rays research, therefore in the following section the most representative historic moments about cosmic rays physics will be summarized <sup>5</sup>.

## 1.2 Brief historical review of cosmic ray research

to end the historical review a chronological summary of other relevant historical facts in cosmic ray research is presented [RadioactivityBook, 2, 5, 14, 28]:

**1929** Dimitry Skobelzyn makes the first observations of cosmic rays passing through a cloud chamber. After that, Bothe and Kolhörster proved that the traces left by the passage of secondary cosmic rays inside the instrument are curved by magnetic fields. This was the proof that secondary cosmic rays observed at sea level are charged particles.

**1932** Carl David Anderson discovers the *positron* by performing studies at the California Institute of Technology (Caltech) of cosmic rays with a cloud chamber. Anderson also discovered the muon (1936) as a result of his studies on cosmic radiation.

**1934** Hans Bethe and Walter Heinrich Heitler developed a theory for the development of electromagnetic showers in the atmosphere.

**1941** Norman Hilberry calculates the energy distribution curve of cosmic rays in the energy range from  $1 \times 10^{10}$  eV to  $5 \times 10^{10}$  eV (see fig. 1.7).

Marcel Schein et al. published experimental results from an air balloon flight experiment performed at the campus of the University of Chicago, USA, which showed that cosmic rays are composed mainly by protons.

**1952** First observations of Cherenkov light in the night sky produced by extensive air showers are made with a parabolic mirror of 25 cm and a phototube of 5 cm at the UK Atomic Energy Research Establishment, Harwell, England. This observations were made by William Galbraith and his colleague, John V. Jelley.

**1953** W. Galbraith and J. Jelley developed the air Cherenkov technique for the detection of EAS. This technique gave rise to Cherenkov astronomy. It allows to estimate the arrival direction of primary cosmic rays and gamma rays with large precision.

**1979** Robert L. Golden et al. discovered antiprotons in the flux of cosmic rays.

**2000** It begins the construction of the Pierre Auger observatory in Argentina. The main goal of this observatory is to study EAS generated by ultra-high energy cosmic rays ( $E > 10^{18}$  eV). This is the first experiment that combines an array of water Cherenkov detectors and fluorescence telescopes for a simultaneous observation of EAS. The water Cherenkov array deployed on the surface works all day long making observations of cosmic rays, while fluorescence telescopes can only perform measurements under specific weather conditions and under moonless nights, but they allow better estimations of the energy of the extensive air showers than a base ground detector array.

---

<sup>5</sup>A more detailed description of the history of cosmic rays and related topics can be found at [RadioactivityBook, 2, 9, 10, 22, 27]

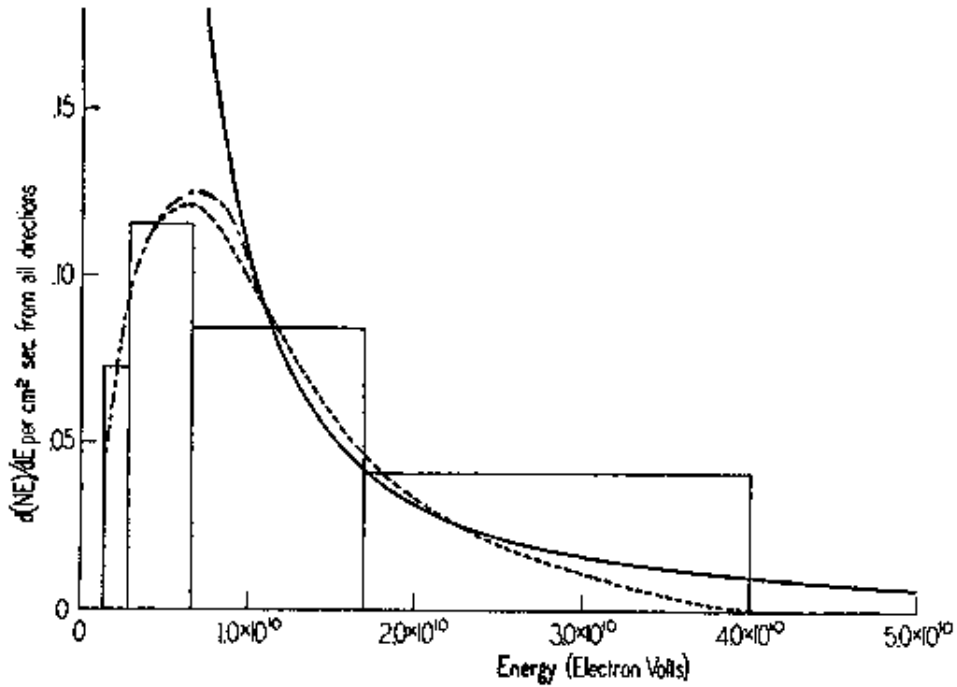


Figure 1.7: Energy distribution curve (solid line) of cosmic rays in the region of  $10^{10}$  eV calculated by N. Hilberry [29]. Hilberry obtained this curve by fitting experimental data from I. S. Bowen et al. [30] on extensive air showers with a power law. Hilberry found that the measurements can be described by an  $E^{-2.75}$  function. The fit of the data is represented by the solid curve and it describes a power-law  $E^{-2.75}$ . The dotted curve is the fit of I. S. Bowen, R. A. Millikan and H. V. Neher. *Source:* [29].

### 1.3 Cosmic rays

Cosmic rays can be considered as that extraterrestrial radiation composed by atomic nuclei, neutrons, relativistic electrons and even antiparticles that reach the top of Earth's atmosphere [14]. Its origin and propagation mechanism are yet unknown and are still under study by several scientific collaborations around the world, which base their work on physical models, numerical methods, simulations and measurements of cosmic rays, as well as the observation of the Universe with complementary astrophysical windows.

Some of the questions that are expected to be answered through the study of cosmic rays are:

1. What are the sources and acceleration mechanisms of cosmic rays?
2. What is the energy spectrum and mass composition of cosmic rays?
3. How do they propagate across the Universe?
4. What new physics can be learned from them and what can it be learned about the astrophysical environments in which they are produced?

Cosmic rays can be also used to infer the properties of the magnetic field of our Galaxy and study physical processes of high energy that occur in the Milky Way and beyond. On the other hand, cosmic rays offer also the possibility to analyse samples of matter from beyond our solar system too. These studies can be improved using gamma rays and high-energy neutrinos which are also produced in cosmic ray accelerators.

The astronomical observations of gamma rays, neutrinos and high energy cosmic rays, among others, have given clues about astrophysical objects that might be responsible for cosmic ray acceleration. The sources seem to be inside and out of our Galaxy. The sources of high energy cosmic rays include shock waves produced by stellar explosions such as supernova remnants (SNRs) [31] (see fig. 1.8), and may also include pulsars, superbubbles, etc. Meanwhile, the extragalactic sources include active galactic nuclei (AGN's) [32–34] and may be the so called *Gamma Ray Bursts* (GRB's) [35, 36].

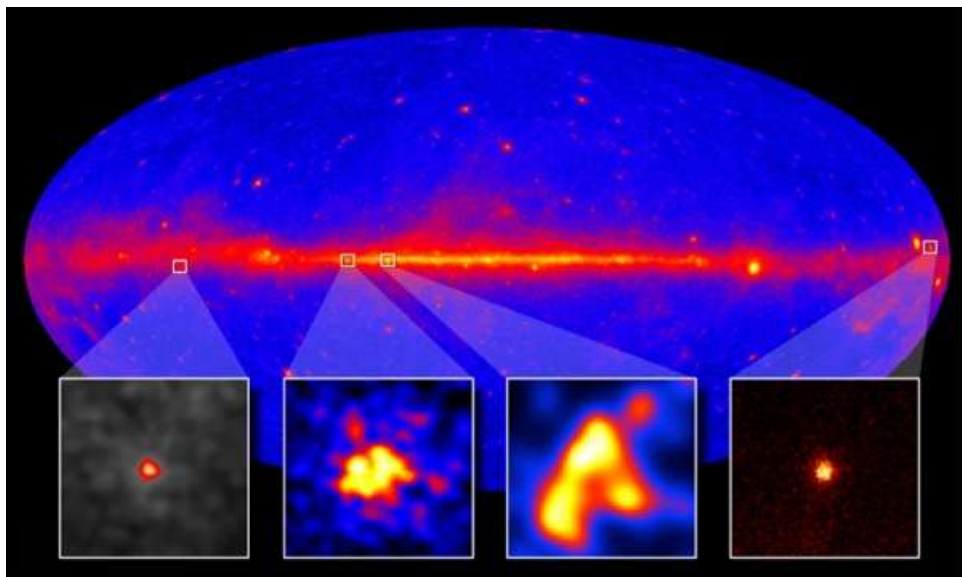


Figure 1.8: From left to right, the figure shows the gamma rays associated with SNRs Cassiopeia A, W51C, W44 and IC443 detected by Fermi's Large Area Telescope (Fermi-LAT) [37]. *Credit:* NASA/DOE/Fermi LAT Collaboration.

By identifying the spectrum of the different types of atomic nuclei that are present in the cosmic radiation, it is expected to find out clues about the mechanisms that produce them and to understand more about their propagation through the interstellar medium. The cosmic ray composition can also help to find out about the environment of the sources and the interstellar and intergalactic medium. Finally, cosmic rays have also information about secondary reactions such as fragmentation that cosmic rays undergo during their propagation in space.

In the following subsections there is a more detailed description about the sources, composition, acceleration and propagation of cosmic rays.

### 1.3.1 Primary spectrum of cosmic rays

Primary cosmic rays are those particles of high energies that are accelerated inside astrophysical sources. Among them there are electrons and atomic nuclei, for example, of hydrogen, helium, carbon, oxygen, neon, iron, and other chemical elements that are result of stellar nucleosynthesis. Secondary cosmic rays in general are referred as those that are produced from the interaction of primary cosmic rays with interstellar/intergalactic gas or with Earth's atmosphere, and are composed by different kind of particles and atomic nuclei, some of them are not abundant in stellar nucleosynthesis, like, lithium, beryllium and boron. Antiprotons and positrons are secondaries. Nowadays there is an interest in measuring the ratio between these secondary components are primaries in order to constrain the models of propagation of cosmic rays in the galaxy [38].

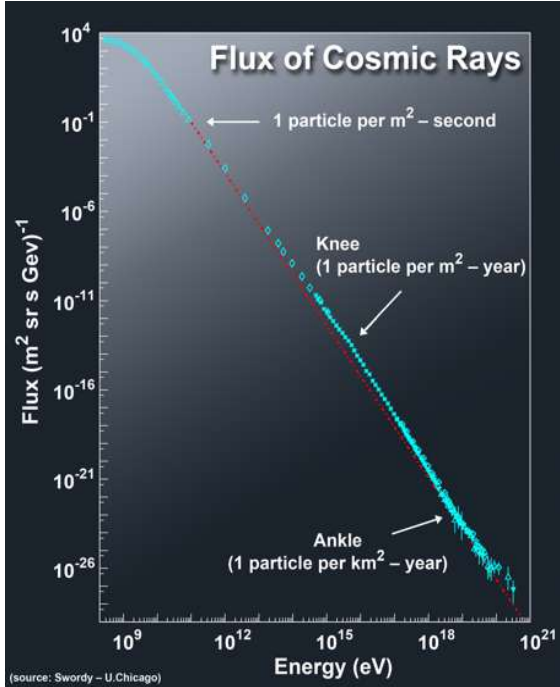
In 1949, Enrico Fermi made one of the first predictions on the energy distribution of cosmic rays assuming that cosmic rays are accelerated in collisions with magnetic clouds in the space (second order acceleration mechanism) [39]. Fermi found that this distribution of energy according to this model can be described by a power law, however the model didn't make predictions about the corresponding spectral index. In 1959, G. V. Kulinov and G. B. Khristiansen observed that the spectrum of cosmic rays was not featureless [40]. They discovered a kink in the spectrum around 1 PeV. This structure was called *the knee*.

It is of great importance to understand the energy distribution of cosmic rays. This knowledge is fundamental to validate any given theory about the origin and propagation of such radiation. The number of particles with energy  $E$  inside some certain differential energy interval  $dE$  is called the *spectrum* [15]. According to the experimental data, the total spectrum of cosmic rays (which corresponds to the sum of all spectra of individual nuclei) spans from a few MeV up to  $E \approx 10^{20}$  eV, and decreases following a power law of the type  $dN/dE \propto E^\gamma$ , where  $\gamma$  is known as the spectral index ( $\gamma \approx -2.7$ ). The differential intensity of cosmic rays is defined as the number of particles that arrive to the detector per unit area, per time unit, per solid angle  $d\Omega$  (in steradians), and per energy interval. In fig. 1.9 (left) a compilation of different measurements of the differential intensity of cosmic rays can be seen. The cosmic ray spectrum can be expressed as a function of [38]:

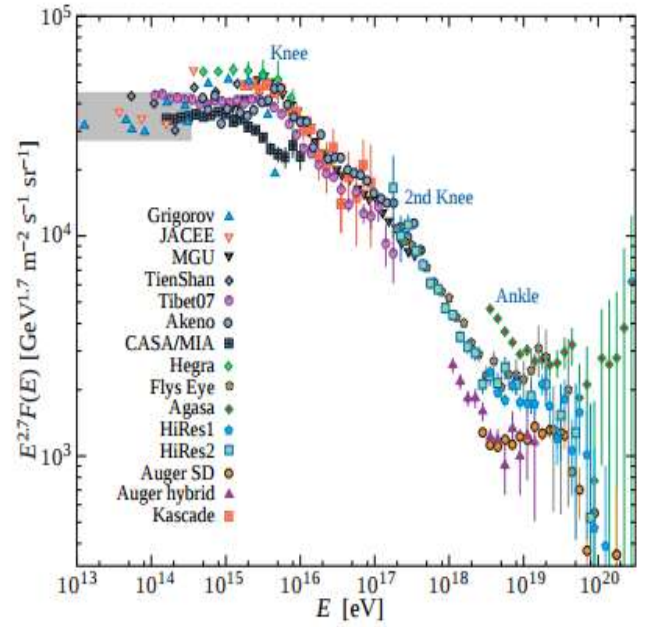
1. *Rigidity unit*,
2. *Energy per nucleon*,
3. *Energy per nucleus*.

The units of the differential intensity,  $I$ , are  $[m^{-2}s^{-1}sr^{-1}\epsilon^{-1}]$ , where  $\epsilon$  are the units of one of the previous variables.

In fig. 1.9 (right) the differential intensity is multiplied by a power of the energy to better appreciate the details of the spectrum. In this figure it can be seen three prominent structures in the cosmic ray spectrum above energies of  $1 \times 10^{14}$  eV, the *knee* at around  $3 \times 10^{15}$  eV, the *low energy ankle* at  $2 \times 10^{16}$  eV, the denominated *second knee* located at approximately  $1 \times 10^{17}$  eV, and the *ankle*, that is found at  $3 \times 10^{18}$  eV [42–44]. The spectral index of the all-particle spectrum is  $\gamma \approx -2.7$  just below  $E \approx 3 \times 10^{15}$  eV, before reaching the *knee*. The change in the spectral index above the *knee* is of  $\gamma \approx -3.1$ , and above the *second knee* the spectrum is even steeper ( $\gamma \approx -3.2$ ). After the *ankle*,  $\gamma \approx -2.7$  [45, 46].



a)



b)

Figure 1.9: a) Total energy spectrum of high energy cosmic rays [41]. At energies around  $10^{11}$  eV, the intensity is equal to 1 particle per  $\text{m}^2$  per second, at energies of approximately  $10^{15}$  eV, the intensity is equal to 1 particle per  $\text{m}^2$  per year and at energies of  $10^{18}$  eV, it is of 1 particle per  $\text{km}^2$  per year. b) The total energy spectrum of cosmic rays is multiplied by a scale factor [38],  $E^{2.7}$ , to enhance the structures present at energies of  $3 \times 10^{15}$  eV,  $1 \times 10^{17}$  eV and  $3 \times 10^{18}$  eV which are called the *knee*, the *second knee* and the *ankle*, respectively.

The results from different experiments of indirect measurements suggest that the change in the spectral index at the *knee* may be due to a transition in the acceleration mechanism or a change in the type of source, or even the loss of efficiency of the magnetic field that confines the high energy cosmic rays in the source or in the galaxy [42].

The *knee* might point out to the fact that most of the cosmic accelerators in the galaxy have reached their maximum energy, which might be reflected in a change in the mass composition and in an increment of the abundance of heavy nuclei [15]. It is known that in this energy region of  $3 \times 10^{15}$  eV the spectrum is dominated by the light and medium component of cosmic rays, i.e., protons and atomic nuclei of helium, carbon, oxygen, among others ( $A < 16$ ). In the region of the *second knee* the dominant component is the heavy one. This second knee is associated to the presence of a cut in the iron spectrum. The study of the spectrum of the mass groups of cosmic rays is of importance since it might throw new clues about the origin of the *knee*. In general, the knee is attributed to the loss of magnetic confinement that occurs at the acceleration regions of cosmic rays. This scenario predicts that all of the individual spectra of cosmic rays for different mass components should have a *knee* whose location depends of the electric charge [47]. The energy of each *knee* turns out to be proportional to  $Z \cdot E_{knee}$ , were  $Z$  is the electric charge of the cosmic ray nucleus and  $E_{knee} \approx 3 \times 10^{15}$  eV [48]. Such scenario seems to be supported by *KASCADE* [48] and

*KASCADE-Grande* [49–51] measurements.

### 1.3.2 Cosmic ray primary composition

Near 79% of primary nuclei inside the galaxy are protons and, approximately, around 20% are nuclei of He, and it is assumed that this is also valid for the Universe in a big scale. Studies about the elemental composition of cosmic rays with energies  $E \lesssim 10^{16}$  eV are mainly performed by detectors installed at air balloons which fly at the top of the atmosphere or satellites that orbit the Earth. The study of the composition of cosmic rays with energies  $E \gtrsim 10^{15}$  eV can also be done through the study of extensive air showers (EAS) in the atmosphere with based-ground experiments, but the information of the composition is more uncertain than in the direct case due to the uncertainties on the hadronic interaction models employed in the simulations of the EAS that are used to interpret the recorded data [42].

In general, the chemical composition of cosmic rays is similar to the abundance of elements in our Solar System (see fig. 1.10), suggesting a stellar origin of cosmic rays [52]. However, there are some differences on the relative abundances of some elemental nuclei (Li, Be, B, Mn, V, Sc) because there are other secondary mechanisms that also produce such elements, spallation reactions or fragmentation of cosmic rays in the interstellar medium.

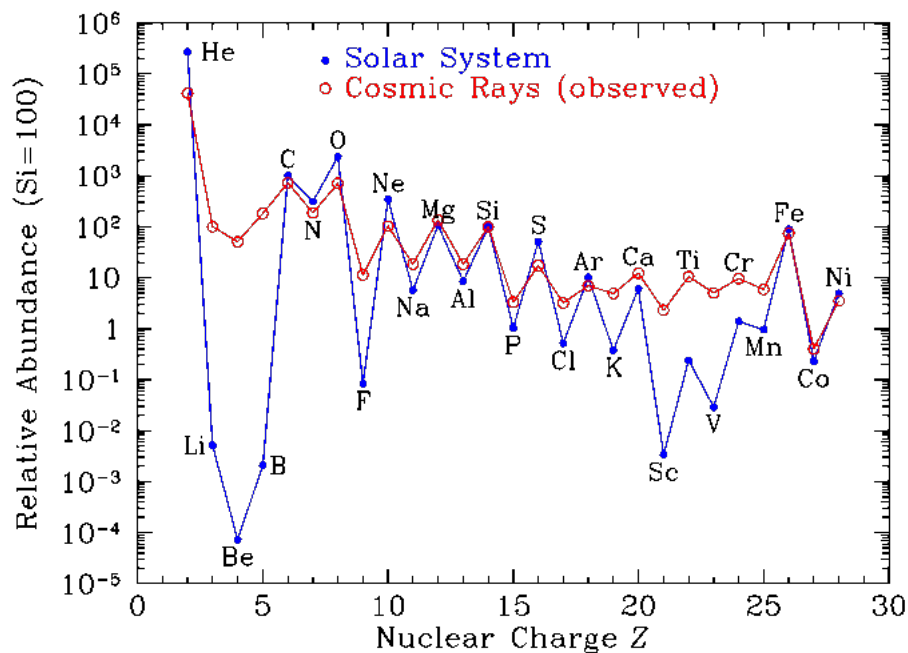


Figure 1.10: Relative abundances of chemical elements in galactic cosmic rays of energies below  $E < 10$  GeV and in the Solar system as function of the nuclear charge,  $Z$  [52].

As mentioned before, positrons and antiprotons are also components of cosmic rays. It is considered that these particles are mainly secondaries. The detailed study of the spectrum

of such component can reveal new insights about the propagation mechanisms of cosmic rays and set constraints on new physics scenarios [53].

Elements heavier than antihelium and antideuterium haven't been found on cosmic rays. The detailed studies of the flux of antiparticles on cosmic rays is important to test propagation and reacceleration models of cosmic rays, test physics beyond the standard model and search for antimatter stars [54]. Experiments like the Alpha Magnetic Spectrometer (AMS) have the mission to search for signals of dark matter and antimatter in the cosmic radiation, as well as to perform a detailed analysis of the composition and flux of low energy cosmic rays [55]. AMS studies the primary cosmic ray composition exploring a new frontier in the field of particle physics, searching for antimatter of primal origin and investigating the nature of dark matter.

### 1.3.3 Sources

#### Origin of galactic cosmic rays

The galactic cosmic rays have a wide distribution of energies, expanding up to  $E \lesssim 10^{18}$  eV. However, there are some questions regarding the sources and acceleration regions of the galactic cosmic rays.

The first assumption is that stars with small mass are responsible of injecting low energy cosmic rays into the interstellar medium given its coronary activity [15]. The stars with small mass are very active and therefore their contribution to the injection of cosmic rays is expected to be very significant. It is proposed that the injection mechanism begins with the acceleration of certain elements to supra thermal energies due to coronary activity, the particles are later expelled to the interstellar medium; after this, the particles are accelerated by shock waves which are produced by supernova remnants and/or other galactic sources [15].

Another supposition about the origin of cosmic rays implies the ionization of dust particles of the interstellar medium. In 1949, L. Spitzer pointed out that dust particles of the interstellar medium can be accelerated to velocities similar to that of light by the radiation pressure of supernova remnants [42]. In 1954, H. Alfvén noticed that cosmic dust gains charge in an ordinary way and that later it can be accelerated by the same electromagnetic processes that produce cosmic rays [42].

Alfvén's theory try to explain the abundance of chemical elements that compose the cosmic rays along with the mechanism of injection of cosmic rays into the interstellar medium.

Finally, massive stars can be consider as another possible source of injection of low energy cosmic rays. These stars can be classified into three types [15]:

1. Stars with a stellar mass between 8 and 15 solar masses, that shed most of their mass in the form of planetary nebulae or become a supernova.
2. Stars with a mass between 15 and 25 solar masses, which violently explode as supernovae enriching the stellar wind mainly with hydrogen.
3. Stars with a mass bigger than 25 solar masses. When these stars reach their blue giant phase, they explode as supernovae or core-collapse-supernovae.

In this scenario, the injection of low energy cosmic rays into interstellar medium is through stellar wind, explaining at the same time the variety of chemical elements in the cosmic ray flux, like super massive stars ( $> 25$  solar masses).

### Origin of extra-galactic cosmic rays ( $E \gtrsim 10^{18}$ eV)

Extra-galactic sources energized by massive black holes at the center of galaxies are abundant and powerful enough to be responsible of very high energy cosmic rays up to the ultra-high energy regime, these sources are known as active galactic nuclei or *AGN's* [56]. Another source of very high cosmic rays could be the Gamma Ray Bursts [57].

As mentioned before, cosmic rays are deflected by magnetic fields all over the cosmos due to its charged nature, meanwhile photons and neutrinos are electrically neutral particles and travel in straight trajectories from its origin. Gamma rays can be produced by hadronic interactions (for e.g. from the decay of  $\pi^0$ 's) or by electromagnetic phenomena like inverse Compton scattering or synchrotron radiation. On the other hand, neutrinos are produced only from hadronic interactions. High-energy neutrinos of extraterrestrial origin are most likely to be produced by the interaction of a proton with gas at or near cosmic ray acceleration regions, so the detailed study of this high-energy particles can throw new information about cosmic ray sources. The IceCube Neutrino Observatory, located at the South Pole, was built and designed to observe high-energy neutrinos and cosmic rays that interact with Earth's atmosphere. IceCube collaborates in multimessenger observations to unveil some of the questions about cosmic rays [58], such as the determination of their origin by measuring neutrinos of the highest energies. In 2018, IceCube confirmed the acceleration of cosmic rays up to PeV energies [34].

#### 1.3.4 Primary acceleration of cosmic rays

The acceleration mechanism of cosmic rays is one of the unresolved questions on cosmic rays, which makes this topic a very wide field of study [59]. There are many models that try to explain the acceleration mechanism and some of the principal models employed on the study of acceleration of cosmic rays are discussed below.

◇ Fermi acceleration mechanism of second order

Observations of cosmic rays suggest that the process of acceleration gives place to the formation of an energy spectrum of the power law-type. The spectrum of cosmic rays is of the form  $dN(E) \propto E^{-\delta}dE$ , where the  $\delta$  exponent lays between the range of 2 and 3.

In 1949, E. Fermi proposed a model in which charged particles gain energy through collisions with interstellar clouds, this way being accelerated to high energies [60]. In this acceleration model, charged particles are reflected by *magnetic mirrors* associated with anomalies of the galaxy's magnetic field. The *magnetic mirrors* move randomly with velocity  $V$ , thus the particles gain energy in a stochastic way in the collisions [61]. To recover a distribution of the power-law type, particles must remain at the acceleration region for some certain characteristic time  $\tau$  [61].

The mean energy gained per collision is:

$$\left\langle \frac{\Delta E}{E} \right\rangle = \frac{8}{3} \left( \frac{V}{c} \right)^2. \quad (1.2)$$

From eq. 1.2 it is clear that the increase in the energy is of *second order* in the  $V/c$  term. Hence this process is called Fermi acceleration of second order [61].

The final spectrum predicted by this model is:

$$N(E)dE = constant \times E^{-x}, \quad (1.3)$$

where  $x = 1 + (\alpha\tau_{esc})^{-1}$ , where  $\tau_{esc}$  is the characteristic time that a particle remains at the acceleration region due to the magnetic field's confinement,  $\alpha = \frac{4}{3} \left( \frac{V^2}{cL} \right)$ , and  $L$  is the distance the particle travels between the *magnetic mirrors*.

This model has some shortcomings, some of which are:

- The velocity of the interstellar clouds of the galaxy have small velocities compared to the speed of light,  $V/c \leq 10^{-14}$ , which ends up in a very small energy gain for the charged particles.
- Despite that this model manages to produce a spectrum of the power law form, there's nothing in this model that indicates that the spectral index should be approximately 2.7, which is the average value calculated through observations of the cosmic ray spectrum.

◇ First order Fermi acceleration mechanism

The goal of the Fermi's acceleration model of first order is to derive a linear energy gain on  $(V/c)$ , this is a condition that makes the acceleration process more efficient, specially for bigger values of  $V$ . This configuration occurs when relativistic particles collide with shock waves (for example, shock waves produced by SNRs, AGNs, etc.) that can reach supersonic velocities [62].

The energy gain is expressed as:

$$\left\langle \frac{\Delta E}{E} \right\rangle = \frac{4}{3} \left( \frac{V}{c} \right), \quad (1.4)$$

and the corresponding spectrum is:

$$N(E)dE = constant \times E^{-2}dE. \quad (1.5)$$

First order Fermi acceleration mechanism is very promising, despite the fact that the derive spectral index is different than the observed spectral index but it's more likely to be present in the Universe at different astrophysical environments and the spectrum is closer to the observed one. Unlike the second order Fermi's model, a fixed value for the spectral index is found and the difference with the observed value seems to be due to the propagation effects through the interstellar medium according to the standard model about the propagation of cosmic rays in the galaxy [62].

◇ Diffusive shock acceleration model

This is the more valid model for the acceleration mechanism of cosmic rays since the 70's and it is associated to the acceleration of charged particles at shock waves using the first order Fermi's acceleration mechanism [61].

The particles are accelerated in a sort of ping-pong at the front of the shock waves, for example, in supernova remnants. The cosmic ray trajectories are scattered due to fluctuations of the magnetic field at the shock wave front. If the local magnetic field would be uniform, the cosmic rays would easily escape the acceleration region through the field lines in the magnetic field. Cosmic rays travel in a random way through out the field lines inside the shock region, crossing the shock front multiple times and gaining energy in each cross.

### Acceleration regions

In 1984, A. M. Hillas found out that a cosmic ray acceleration region must be at least twice as big as the Larmor radius of the particles for it to accelerate cosmic rays up to high energies. When this region is of the size of the source the efficiency to accelerate particles is lost. This sets a limit on the maximum energy of the charged particles that can be accelerated at the sources [63] and is given by:

$$E_{max} \simeq Z \left( \frac{B}{\mu G} \right) \left( \frac{R_{source}}{kpc} \right) \times 10^{18} eV, \quad (1.6)$$

where  $Z$  is the particle's charge in units of  $e$ ,  $R_{source}$  and  $B$  are the size and magnetic field of the acceleration region. At the acceleration region, the proton spectrum will cutoff first, followed by helium, carbon and so on [64]. These cutoffs are reflected on the spectrum of cosmic rays and can be interpreted as a result of a magnetic rigidity cutoff in the source.

There are many different types of astrophysical sources that could meet the requirements to accelerate cosmic rays up to the observed high energies. In the so called *Hillas' plot* [65] (fig. 1.11), different astrophysical objects are shown in the phase space of the characteristic magnetic field at the site,  $B$ , against the typical size,  $R$ , of the source along with the limits needed to accelerate cosmic rays up to a given energy according to formula ([Eq:la\_que\_va\_abajo]).

With the Hillas' model it is possible to identify many potential populations of sources of high energy cosmic rays (see fig. 1.11).

The mass composition of cosmic rays is sensitive to their origin and propagation, therefore the importance of identifying their sources.

There are different models trying to explain the features that are observed in the energy spectrum of cosmic rays by assuming the existence of different types of sources with energy cuts that could correspond be responsible of the structures in the energy spectrum. For example, in [67] three types of sources with different  $E_{max}$  are used for the analysis of the cosmic rays spectrum. These sources are:

Population 1: It is associated with SNRs, using the *knee* as an indicator of the energy cut of this population.

Population 2: This population is considered as a component of high energy galactic cosmic rays of unknown origin. The energy cut of this population is at  $E = 3 \times 10^{17}$  GeV.

Population 3: It is assumed that this population of ultra high energy cosmic rays is of extra-galactic nature. This group has an energy cut at  $E = 1.3$  EeV.

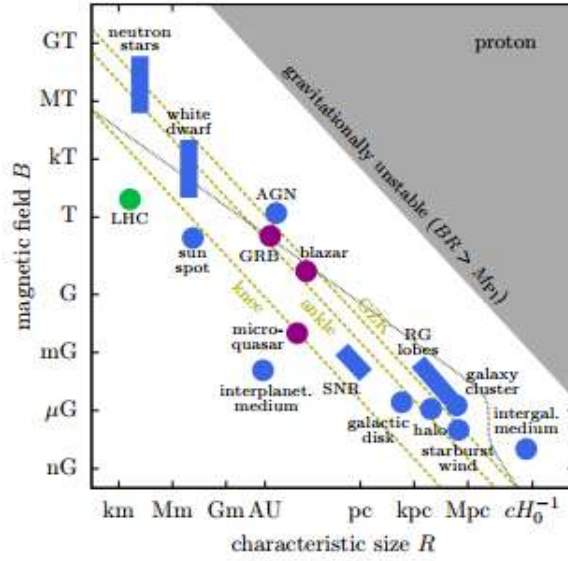


Figure 1.11: Hillas' plot for different possible acceleration sources of cosmic rays (blue). The dotted lines are upper limits for potential proton accelerators up to knee region, ( $\approx 10^{15}$  eV), the ankle ( $\approx 10^{18}$  eV), and up to the GZK limit ( $5 \times 10^{19}$  eV). Once the particle reaches its maximum energy, the magnetic field is no longer able to confine the particle at the source, therefore the particle escapes from the acceleration site [66].

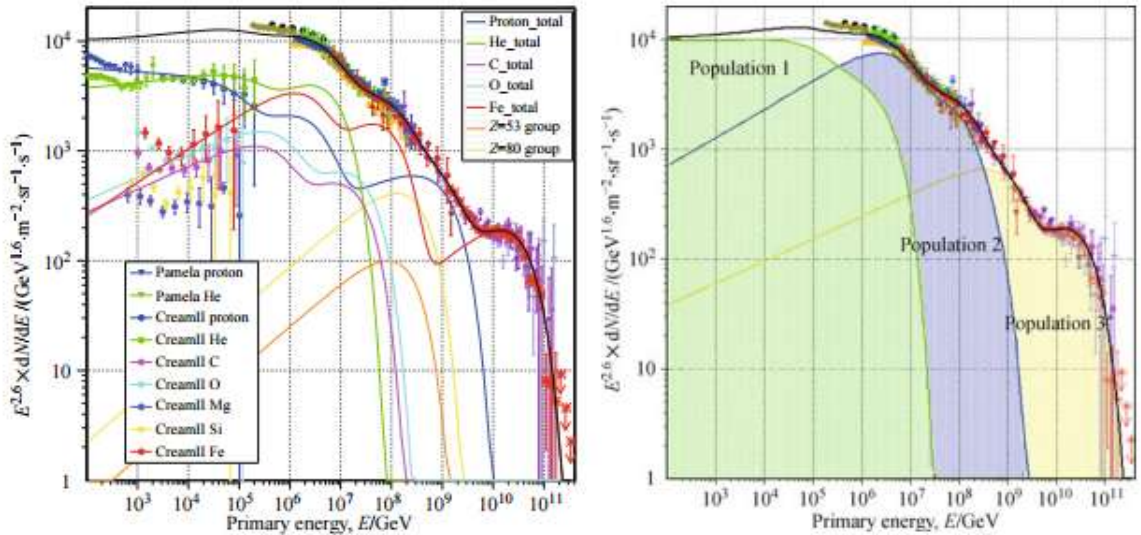


Figure 1.12: Three-population Hillas model that could explain the observed spectrum of cosmic rays [67].

## Propagation

Currently, the propagation mechanisms of cosmic rays through the interstellar medium are poorly understood. As the cosmic rays travel across the Universe, they are deviated by mag-

netic fields and interact with particles from the medium, such as interstellar gas. These interactions cause the emission of secondary particles which decay producing hadrons, gamma rays, neutrinos, and electron-positron pairs, pair production ( $p\gamma \rightarrow pe^+e^-$ ), pion production ( $p\gamma \rightarrow \pi N$ ), and compton like interactions among others [63]. The study of these emissions may give new insights about the propagation of cosmic rays in the interstellar space, and about their origins [55].

During their propagation, cosmic rays can also suffer energy losses and be subject to re-acceleration processes which change the shape of the initial spectrum of the particles.

In the *Leaky box* model [68] for the propagation of cosmic rays in the Milky Way, it is assumed that these particles are accelerated at astrophysical sources in the galactic disk and propagate inside a cylindrical box of height  $\sim 3 \text{ kpc}$  and radius  $\sim 15 \text{ kpc}$ . When cosmic rays arrive to the frontiers of the box, they are reflected. However, there is a small probability for the particles to escape at the moment they reach the frontier. The confinement inside the box is due to the presence of the galactic magnetic field in which they propagate diffusely. Diffusion in the interstellar medium is produced because the magnetic field modify the arrival direction of cosmic rays in a random walk way, causing that cosmic rays no longer point back to their source (except for the extreme energies,  $E \sim 10^{20} \text{ eV}$ ).

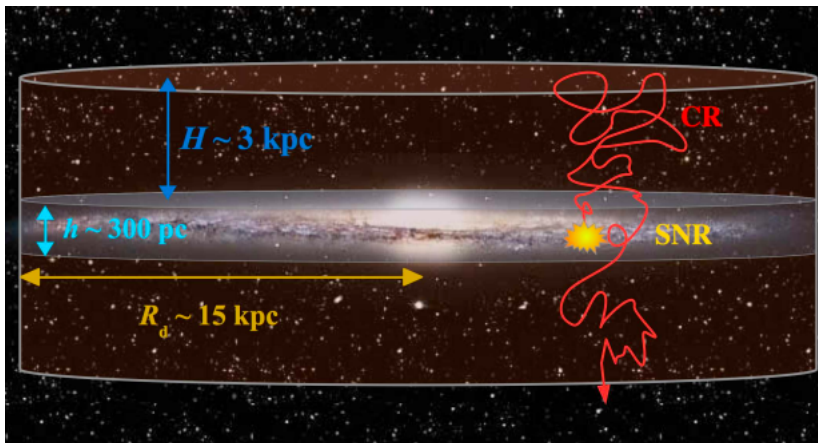


Figure 1.13: Simple model of the leaky box model. Cosmic rays travel in all directions in the galactic disk (described as a cylinder or radius  $R_d = 15 \text{ kpc}$  and height  $H = 3 \text{ kpc}$ ) interacting with the galactic magnetic field and the interstellar medium. Some particles manage to escape from the magnetic field confinement [68].

The propagation of cosmic rays can be simulated through numerical methods. GALPROP<sup>6</sup> is a public numerical code that simulates the propagation of cosmic rays, electrons, positrons and antiprotons [69]. GALPROP has an online service which allows the user to perform calculations on a dedicated high performance computing cluster at Stanford University and it is available at [70].

<sup>6</sup> The latest public version of GALPROP is 56.0.2870 and it was released on October 27th, 2017.

# Chapter 2

## Extensive air showers

*“The scientist does not study nature because it is useful to do so. He studies it because he takes pleasure in it because it is beautiful. If nature were not beautiful it would not be worth knowing, and life would not be worth living.”*

-H. Poincaré.

The observations of Extensive Air Showers (EAS) made by Bruno Rossi, Werner Kolhörster and Pierre Auger opened a new era in the research of high energy physics, particle physics and astrophysics. However, the study of EAS still represents a challenge given the difficulty of describing the hadronic interactions that take place in this phenomenon. This chapter focuses on the development of the EAS, as well in the principal parameters that are used for the detailed study of this phenomenon.

### 2.1 Discovery of Extensive Air Showers

At the beginning of the 1930s, the Italian physicist Bruno Rossi planned a series of experiments in Asmara, Eritrea, to study the East-West effect; but it was until the autumn of 1933 that Rossi and his team of collaborators were able to perform such experiments [22]. Based on his observations in Eritrea, Rossi stated that [71]: *it seems that once in a while the recording equipment is struck by very extensive air showers of particles, which cause coincidences between counters, even placed at large distances from one another* [22, 40].

Years later, on 1938, W. Kolhörster reported the relation between the simultaneous observations of two counters separated by a distance of 10 m, stating that such relation must be related to *secondary rays of the high-altitude radiation, i. e. to a shower*<sup>1</sup> [72].

Although previous studies of B. Rossi and Kolhörster reported the observation of the phenomenon known today as Extensive Air Showers, the credit for the discovery of the air shower phenomenon was given to Pierre Auger. Later on 1938, Pierre Auger (unaware of the work of B. Rossi and W. Kolhörster) and his collaborators placed several Geiger counters and cloud chambers separated by several meters and operating simultaneously at the Jungfrauoch in the Swiss Alps at 3450 m. Auger discovered that the counters registered the arrival of charged particles simultaneously, concluding that the phenomenon was due to

---

<sup>1</sup>Translation made by [22].

the production of large atmospheric showers, whose origin should be high in the atmosphere [26]. Nowadays it is known that this atmospheric showers are made of secondary particles created by the interaction of primary cosmic rays with atmospheric molecules.

When a gamma ray travels into Earth's atmosphere, it generates a pair production of electron-positron, which in turn generate less energetic photons, by different processes (e.g., *Bremsstrahlung*) throughout their way into the atmosphere. Then, the less energetic photons create new pairs of electron-positron. This process keeps going on until a certain energy threshold is reached. The result of this phenomena is called extensive air shower, EAS, and it can also be produced by cosmic rays.

The air showers generated by the interaction of primary cosmic rays with air particles have three main components, which are the following:

- Hadronic component: formed by mesons, neutrons and atomic nuclei derived from the spallation process of atmospheric nuclei and hadronic interactions.
- Electromagnetic component: composed by gammas, electrons and positrons.
- Muonic component: composed only by muons.

These components are going to be described next.

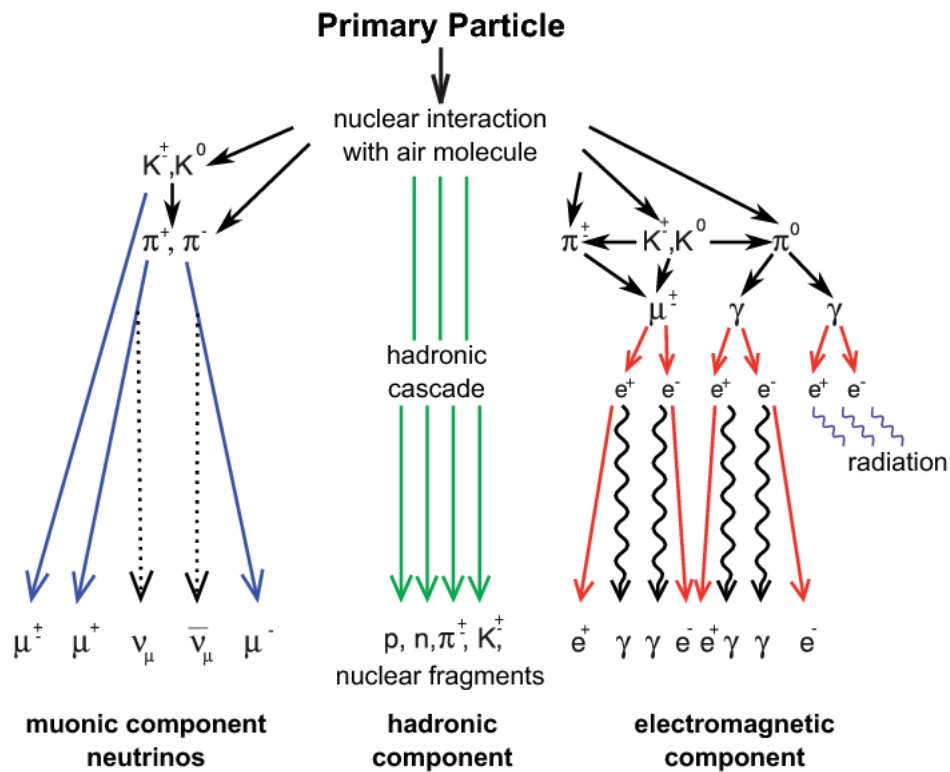


Figure 2.1: When a primary cosmic ray travels into the atmosphere and collides with the particles or molecules in it a shower of secondary particles is generated, which is composed by 3 main components: hadronic, electromagnetic and muonic ones [73].

## 2.2 Hadronic component

This component is the result of a copious process of successive collisions of primary cosmic ray, its fragments, and secondary particles with atmospheric nuclei of nitrogen and oxygen. The resulting secondaries from these collisions are mainly protons, neutrons, nucleon and antinucleon pairs, pions, kaons and charmed particles which end up decaying into other products.

The cosmic rays interact with atmospheric molecules (such as  $N_2$ ,  $O_2$ ,  $Ar$ , etc.) producing a shower of secondary particles whose collisions are dominated by hadronic processes (in the non-perturbative QCD region,  $Q^2 \sim 0$ ). The shower travels at the speed of light and propagates longitudinally along the direction of the initial momentum vector of the primary incident particle. These type of collisions are inelastic and the final momentum is approximately equal to the initial momentum, therefore the momentum difference is almost zero ( $\Delta\vec{p} = \vec{p}_f - \vec{p}_i \approx 0$ ). The air shower secondary particles also have a small transversal momentum, reason why some of the secondary particles travel sideways in a small fraction, creating at the same time a lateral development of the shower.

The composition of the particle population in the cascade changes as it propagates through the atmosphere and the different constituents propagate differently. The hadronic component is mainly dominated by pions ( $\pi^\pm$  and  $\pi^0$ ), which are fundamental for the development of the electromagnetic component. The electromagnetic and muon components of the cascade are products of the hadronic component, which are produced by the decay process of particles that emerge from the hadronic interactions.

## 2.3 Electromagnetic component

The electromagnetic component of an air shower is composed by photons, electrons and positrons mainly produced by the decay of secondary mesons such as pions or kaons. For example, the neutral pion decays into:

$$\pi^0 \rightarrow \gamma + \gamma. \quad (2.1)$$

The products from this decay feed a component dominated by photons and electrons which can reach large proportions if the primary particle is highly energetic. In general, the electromagnetic component dominates in the vertical air showers.

The electron-positron pair production of photons and the *bremsstrahlung* effect of the electrons are the most important processes in the development of the shower. However, the energy loss by ionization (by the collisions), photoelectric effect, Cherenkov radiation and radio emission are also present.

## 2.4 Muonic component

The most common decays of charged pions and charged kaons can be seen in Eqs. (2.2), (2.3) and (2.4), and they are mainly muons and neutrinos, which are very abundant in air showers. The charged pions and kaons commonly decay into:

$$\pi^\pm \rightarrow \mu^\pm + \nu_\mu^\pm, \quad (2.2)$$

$$K^\pm \rightarrow \mu^\pm + \nu_\mu^\pm, \quad (2.3)$$

$$K^\pm \rightarrow \pi^\pm + \pi^0, \quad (2.4)$$

feeding the muonic component. For a standard array of air shower detectors, the neutrinos are practically undetectable. Meanwhile, the muons are easier to detect, although they still present a challenge for their detection given their penetrating nature.

The majority of the muons are produced high in the atmosphere ( $\approx 15$  km). Muons that doesn't decay as they travel through the atmosphere have an energy loss of  $\sim 2$  GeV in the atmosphere before they reach the ground [38]. The muons that do decay contribute to the electromagnetic component of the air shower [59].

Despite the fact that a standard base-ground array of particle detectors can't detect neutrinos, its contribution to the total energy of the shower must be taken into account.

## 2.5 Heitler Model

The Heitler model gives a simple description of the EAS development with some basic parameters from the interaction of the secondary particles. The Heitler model was first developed to depict purely electromagnetic showers, although this model can be extended to the study of hadronic showers. In the following sections, the Heitler model is going to be described for both electromagnetic and hadronic showers [74].

### 2.5.1 Heitler model for electromagnetic showers

The properties of an EAS gives detailed information about the primary cosmic ray that induced it, thus is vital to develop models that accurately describe the properties of an air shower. In particular, the Heitler model gives a very simple depiction of the development of an electromagnetic shower and it doesn't cover all the details of an electromagnetic shower, nonetheless it predicts the most important features of purely electromagnetic showers.

Instead of using three particle types ( $\gamma$ ,  $e^-$  y  $e^+$ ), let us consider only one particle with energy  $E$  to make a simple description of the Heitler model for electromagnetic showers. After traveling a fixed interaction length,  $\lambda_e$ , such particle will produce two new particles with an energy of  $E/2$  each after one interaction as shown in fig. 2.2. Each of these new particles will split into two new particles after traveling an interaction length,  $\lambda_e$ . After  $n$  consecutive interactions or generations, the total number of particles in the shower is  $2^n$ . So, the total number of particles at a given depth ( $X = n \cdot \lambda_e$ ) is:

$$N(X) = 2^n = 2^{X/\lambda_e}. \quad (2.5)$$

The energy  $E$  per particle for a given primary energy,  $E_0$ , is:

$$E(X) = \frac{E_0}{2^{X/\lambda_e}}. \quad (2.6)$$

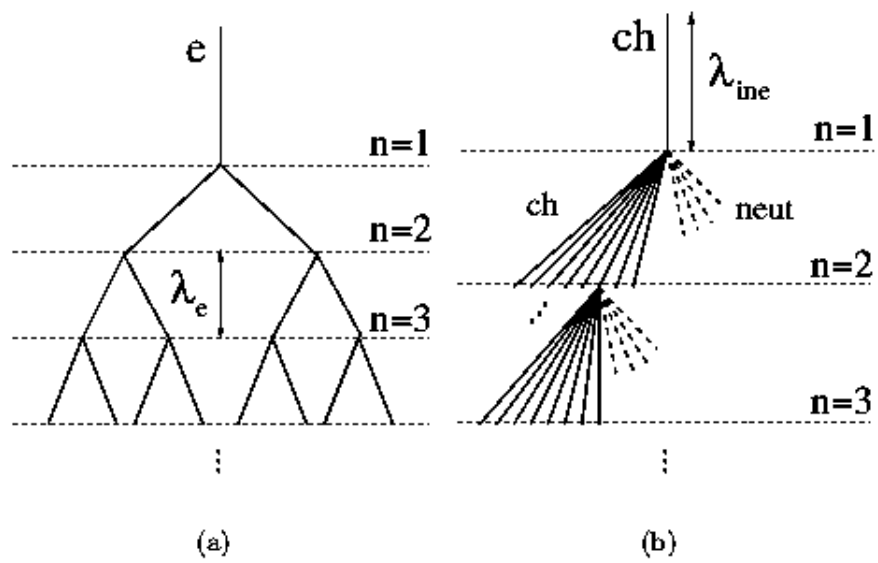


Figure 2.2: Diagram of the generation of an electromagnetic (left panel) and an hadronic (right panel) shower. The solid lines represent charged particles, while the dotted lines represent neutral particles, and  $\lambda_e$  and  $\lambda_{ine}$  are the electromagnetic and primary particle interaction lengths, respectively [74].

The energy at which the process of energy loss dominates over the production of secondary particles is known as *critical energy*,  $E_c$ . It can be assumed that the shower maximum is reached when the energy of the secondary particles reaches  $E_c$ . At this point, the number of secondary particles is [74]:

$$N_{max} = \frac{E_0}{E_c}, \quad (2.7)$$

meanwhile, the corresponding altitude is:

$$X_{max}(E_0) \sim \lambda_e \cdot \ln \left( \frac{E_0}{E_c} \right), \quad (2.8)$$

which is proportional to the logarithm of the ratio of the primary and the critical energies. Heitler's model for electromagnetic showers ends when the shower achieves its maximum [75].

## 2.5.2 Heitler model for hadronic showers

As it was mentioned before, the Heitler model was developed to describe air showers of electromagnetic nature, but this model can be extended to describe air showers induced by hadronic particles. The hadronic interaction of a particle with energy  $E$  is expected to produce  $n_{tot}$  new particles with energy  $E/n_{tot}$  and, in a simple picture of the modified Heitler model for hadronic showers, two thirds of these particles will be charged particles (charged pions) and the other third part will be neutral particles (neutral pions). A diagram of the production of this process is shown at fig. 2.2. The neutral pions quickly decay in electromagnetic particles ( $\pi^0 \rightarrow \gamma + \gamma$ ), while the charged pions decay in muons and neutrinos ( $\pi^+ \rightarrow \mu^+ + \nu_\mu$ ,  $\pi^- \rightarrow \mu^- + \bar{\nu}_\mu$ ) [74].

On each interaction, the electromagnetic component gets one third of the hadronic component energy. After  $n$  interactions, the corresponding energy for the hadronic and electromagnetic components are given by [74]:

$$E_h = \left( \frac{2}{3} \right)^n E_0, \quad (2.9)$$

$$E_{EM} = \left[ 1 - \left( \frac{2}{3} \right)^n \right] E_0, \quad (2.10)$$

respectively.

Even if the air shower was generated by a hadronic particle, after several interactions, the electromagnetic component will carry most of the energy ( $\sim 90\%$  for  $n=6$ ). Thus, the shower depth will correspond to the one of the electromagnetic component,  $X_{max}^e$ . Assuming that the first hadronic interaction produces electromagnetic particles with an energy  $\sim E_0/n_{tot}$ , we have [74]:

$$X_{max}(E_0) \sim \lambda_{ine} + \lambda_e \cdot \ln \left( \frac{E_0}{n_{tot} E_c} \right) \quad (2.11)$$

where  $\lambda_{ine}$  is the primary particle interaction length. eq. (2.11) is an approximate expression for the hadronic showers' maximum depth.

It is assumed that all charged hadrons decay into muons once the energy  $E_{dec}$  is reached. After  $n$  interactions, the charged hadrons will reach the decay energy [74]:

$$E_{dec} = \frac{E_0}{(n_{tot})^n}. \quad (2.12)$$

Now, given the fact that a hadron will produce a muon in its decay process it follows that [74]:

$$N_\mu = n_{ch}^n = \left( \frac{E_0}{E_{dec}} \right)^\alpha, \quad (2.13)$$

where  $\alpha = \ln(n_{ch})/\ln(n_{tot})$ , and  $n_{ch}$  is the number of charged pions in an interaction.

The superposition principle may be used in the case in which the primary particle is a nucleus. If so, making use of the superposition principle the air shower observables can be deduced. Under this hypothesis, a nucleus of mass  $A$  and  $E_0$  energy can be considered as a superposition of  $A$  independent nucleons with an energy  $E_h = E_0/A$ . And finally [74]:

$$N_{max}^A \approx A \cdot \frac{E_h}{E_c} = \frac{E_0}{E_c} = N_{max}, \quad (2.14)$$

$$X_{max}^A \approx X_{max}(E_0/A), \quad (2.15)$$

$$N_\mu^A \approx A \cdot \left( \frac{E_0/A}{E_{dec}} \right)^\alpha = A^{1-\alpha} \cdot N_\mu. \quad (2.16)$$

## 2.6 Hadronic interaction models

The air shower simulations allow to give an interpretation of the observations of EAS in terms of the properties of the primary particle.

The hadronic production parameters are of vital importance in the development of an air shower. Among these parameters are the hadronic cross sections ( $\lambda_{ine}$ ), the particle multiplicity ( $n_{tot}$ ), and the production ratio of neutral particles over charged particles. The predictions made by the hadronic interaction models considerably differ depending on the assumptions made to extrapolate the existing data from particle accelerators.

There are many hadronic interaction models available for the simulation of extensive air showers. All of the high energy interaction models reproduce the particle accelerators' data, but they all differ when it comes to the extrapolation at energies relevant for the study of cosmic rays [74].

Some high energy hadronic interaction models ( $E_{lab} > 100$  GeV) are listed below:

- DPMJET II.55 and III [76],
- QGSJET-II [77],
- SIBYLL 2.3 [78],
- EPOS-LHC [79].

And some low energy hadronic interaction models are:

- FLUKA [80],
- GHEISHA [81].

The differences between the hadronic interaction models are the main sources of uncertainties in the predictions of extensive air showers and in the study of the energy spectrum and mass composition of cosmic rays.

## 2.7 Reconstruction of an air shower

The procedures for the reconstruction of the properties of an air shower depend on the design and physical configuration of the detector. The detectors are set up in arrays and are required to cover wide surfaces to collect as much information from an air shower as possible. In general, the detector arrays are employed for the measurement of cosmic rays of energies  $E \gtrsim 10^{15}$  eV.

The process begins by estimating the core position of the air shower and its arrival direction. These observables depend on the measurement of the lateral distribution of the air shower and the arrival time of the shower front to the detector (see fig. 2.3).

The general procedure to reconstruct some of the most important air shower properties will be briefly described in the following subsections.

### 2.7.1 Arrival direction

The air shower arrival direction is perpendicular to the shower front and it is given by the zenith,  $\theta$ , and azimuth,  $\phi$ , angles. The values of  $\theta$  and  $\phi$  are estimated by the differences between the particles arrival time (see fig. 2.3). The fit of the shower will give the information about the trajectory of the primary cosmic ray, and it is portrayed as a plane traveling at the speed of light, but since the shower front has a curvature, to fit it to a plane the differences of the arrival time to the detectors between the secondary particles near the shower axis and those at the shower tail must be taken into account.

### 2.7.2 Shower core

The central region of the air shower is known as the shower core and this region has the biggest density of particles, which decreases fast far from the core. There are some air showers that have sub-cores or multiple cores due to the presence of nucleons or nuclei fragments created by the fragmentation of a heavy primary particle, or by highly energetic secondary particles. In general, the procedure to estimate a first assumption of the shower position is by assuming fitting the lateral density distribution function of the shower particles [42].

### 2.7.3 Shower age (s)

The age parameter gives a description of the stage of development of an air shower. This parameter arose from the study of the longitudinal and lateral development electromagnetic

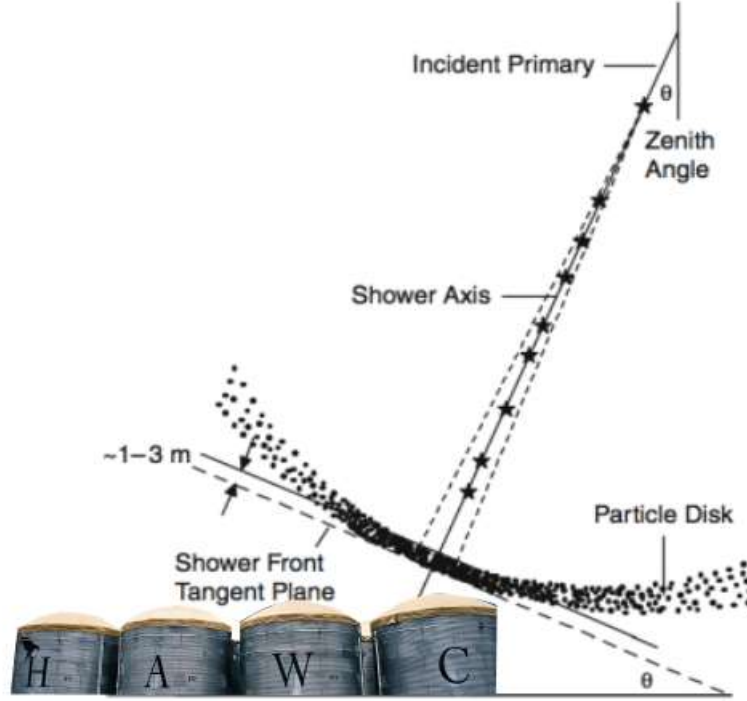


Figure 2.3: Sketch of the particle disk and the front of an extensive air shower arriving at an array of particle detectors [42].

extensive air showers [82]. Even though this concept appeared from the study of electromagnetic particles it can also be extended to describe air showers of hadronic nature.

The longitudinal age parameter was one of the firsts parameters employed to describe the stage of development of the electromagnetic air showers. This parameter is related with the increase and decrease of secondary particles in the extensive air showers and with the energy spectrum of photons and electrons [42].

In general, all the electromagnetic showers are similar to each other once they've reached their point of maximum development. The similarity between the electromagnetic air showers can be explained from the fact that the energy spectrum of photons and electrons have the same shape (longitudinal and lateral) at the shower maximum. Also, these particles have the same lateral distribution around the shower core.

The longitudinal age parameter depends on the production, energy spectrum and decay of secondary particles in the shower. In the case of an electromagnetic shower, the longitudinal age parameter is related with the atmospheric depth (see fig. 2.4),  $X$ , by [14]:

$$s = \frac{3t}{t + 2\beta}, \quad (2.17)$$

with  $\beta = \ln(E/E_c)$  and  $t = X/X_0$ , where  $E_c$  is the critical energy for the production of secondary particles, and  $X_0 = 1030 \text{ g/cm}^2$  is the atmospheric depth at sea level.

The values of the longitudinal shower age are:

- $s=0$  for the first interaction,

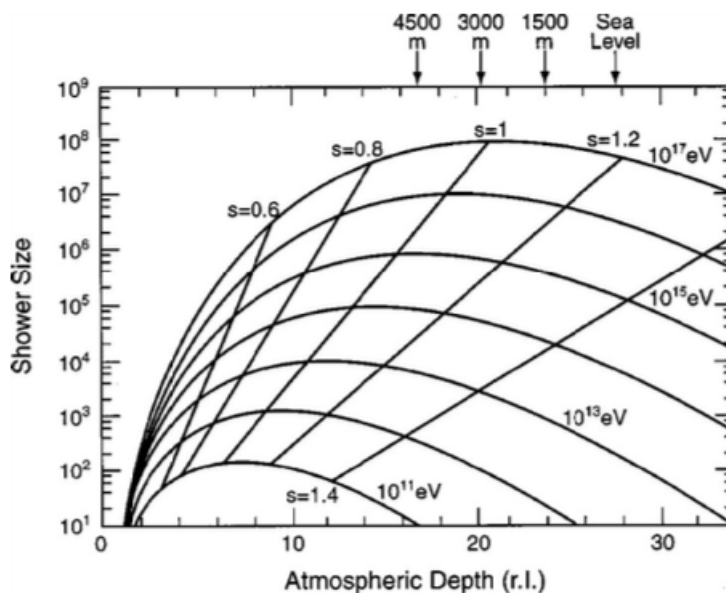


Figure 2.4: Longitudinal development of electromagnetic showers for different primary energy values [83].

- $s=1$  for the shower maximum, and
- $s>1$  for after the shower maximum.

The lateral age parameter of an electromagnetic EAS is related with the shape of the lateral distribution of particles at ground level and it is a function of the distance to the shower axis. It is given by the following equation:

$$s(r) = \frac{2 - \alpha + (6.5 - \eta)}{1 + 2r}, \quad (2.18)$$

where  $r = R/R_0$  and  $\alpha$  and  $\eta$  are parameters estimated from the fit of the lateral distribution of particles at ground level [84].

The lateral and longitudinal age parameters of an electromagnetic air shower are equal, but in the case of hadronic induced air showers these parameters doesn't agree, albeith both of them can still be used as parameters for the development stage of the hadronic air showers. The name lateral age expresses the relation between this parameter and the lateral distribution of electrons at the shower maximum. In particular, the value of the lateral age indicates the slope of the lateral distribution of shower particles at detector level [85, 86]. The showers that have an  $X_{max}$  at an altitude high in the atmosphere are called *old*, and are characterized by having large  $s$  values (flatter lateral distributions) and, in general, are produced by low energy events and heavy primaries. The *young* air showers have an  $X_{max}$ s at lower altitudes in the atmosphere, posses smaller values of lateral age (i.e., steeper lateral distributions) and are related to high energy events and light primaries. The mathematical relation between the lateral age and the lateral distribution is established through a lateral distribution func-

tion (LDF), first described by Nishimura, Kamata and Griesen. For a pure electromagnetic cascade, the compact form of the Nishimura-Kamata-Griesen (NKG) function is [85, 86]

$$\rho(r) = NC \left( \frac{r}{r_M} \right)^{s-\alpha} \left( 1 + \frac{r}{r_M} \right)^{s-\beta}, \quad (2.19)$$

where  $N$  is the number of electromagnetic particles at the observation level,  $C$  is a normalizing factor,  $r_M$  is the Moliere radius,  $\alpha$  and  $\beta$  are fixed parameters, and  $s$  is the lateral age parameter.  $\rho(r)$  gives the density of electromagnetic particles at a given distance,  $r$ , at the shower disk coordinates.

Frequently, the NKG function, or a modified version of it, it is used for the description of the lateral density distribution of other type secondary particles of the EAS, such as muons [87, 88].

# Chapter 3

## Detection methods of Cosmic Rays

The detailed study of the composition and spectrum of cosmic rays at low and high energies may give new insights about the acceleration mechanism, nature and interaction of cosmic rays with the interstellar medium and Earth's atmosphere. Nowadays, there are many international collaborations conformed by scientists of different institutions that have the goal of unveiling the mysteries about the cosmic radiation. In order to achieve this objective, such collaborations have built observatories specially designed to detect and study the cosmic radiation. In general, these observatories can be categorized into two types: of indirect detection or direct detection. We will briefly talk about them in this chapter.

### 3.1 Direct measurements

At low energies, the detection and the study of cosmic radiation can be performed by instruments placed completely or nearly outside our atmosphere, which can be installed at airplanes, air balloons, satellites or space ships. These instruments perform *direct measurements* of cosmic rays [42, 75].

The experiments that are installed at the space stations (or ships) have excellent energy and angular resolution, can have a very large duty cycle, and are able to measure the primary composition of cosmic rays, but their effective area ( $\leq 1 \text{ m}^2$ ) is constrained by the reduced size of the instruments on board [75]. Airborne experiments can have a larger effective area, but their duty cycle is very short. Due to the characteristics of the instruments employed, only cosmic rays and gamma rays of energies up to  $10^{15} \text{ eV}$  can be detected with direct measurements. The constrain on the effective area of these instruments directly restricts measurements to energies up to  $E \lesssim 10^{15} \text{ eV}$ , where the statistics is smaller due to the fact that the cosmic ray flux decays (for example, the flux of cosmic rays at energies of  $10^{15} \text{ eV}$  is just 1 particle per  $\text{m}^2$  per year). Hence, at energies  $> 1 \text{ PeV}$ , the measurements are performed indirectly. This is generally carried out with instruments designed to detect the particle showers generated at the top of the atmosphere by the collisions of primary cosmic rays or gamma rays.

At the present there are more advanced and sophisticated instruments for direct measurements of cosmic rays than in the past century. Some of the most common instruments utilized for direct measurements are:

- *Magnets*: They are used to curve the particle's path in order to calculate the par-

ticle's charge. In tracking chambers they are used to measure the charged particle's momentum [75].

- *Plastic scintillators*: When a cosmic ray interacts with the plastic scintillator a flash of light is emitted. Such flash of light is proportional to the particle's energy and electric charge and it comes from the energy deposited by the cosmic ray in the plastic scintillator as it goes through it. Plastic scintillators are of low cost and can be used to measure the primary particle's energy and time of flight among other variables [89].
- *Emulsion chambers*: An emulsion chamber is a stack of emulsion plates and other materials such as X-ray films and target plates. Emulsion chambers can identify the nature of the incoming particle, record its track, observe its nuclear interactions, and measure its energy. How does it work? When a cosmic ray interacts with an emulsion chamber it produces a shower of secondary particles inside the detector. The emulsion chamber has layers of targets (or dense material) where the cosmic rays interact and emulsion plates that record the particles. The paths of the particles are traced in the emulsion plates which are analyzed to determine the nature of the particles. The target layers and the emulsion plates are intertwined with each other. The top layers at the emulsion chamber are used to identify the primary particle, while the traces produced by the secondary particles are employed to reconstruct the arrival direction of the primary cosmic ray. The primary particle can be identified by the distinctive signature left by it inside the chamber. For example, an electron will produce a single cored shower within a few radiation lengths from the top of the emulsion chamber. The particle's energy is measured at the lower plates of the emulsion chamber and it is estimated either by the radiation length of the particles or by the particle density of the shower of secondary particles [89, 90].
- *Calorimeters*: The main utility of a calorimeter is to measure the primary cosmic ray energy, but it can also provide information about the particle's direction and the nature of the primary particle. The incoming particle's energy is deposited into a calorimeter through collisions with the detector. The calorimeter is composed by layers of very dense materials intertwined with detectors. Inside a calorimeter, the particles interact with the material through electromagnetic or hadronic interactions, depending on the nature of the particle. The energy of the primary particle is divided between the multiple secondary particles that are produced and part of their energy is dissipated via ionization and excitation of matter [75, 89].

Some of the most relevant experiments that have employed the direct measurement technique to study the cosmic ray spectrum above  $10^{13}$  eV are: JACEE [91], CREAM [92–94] and ATIC [95, 96]. On the other hand, among the new detectors used to explore nowadays the flux of cosmic rays up to  $10^{15}$  eV are: NUCLEON [97], DAMPE [98, 99] and CALET [100].

## 3.2 Indirect measurements

As explained before, at high energies the statistics on the direct measurements decreases since the flux of cosmic rays decays following a power law. This way it is necessary to

perform indirect measurements through air shower detectors with large area installed at ground level, which can compensate the small flux of cosmic rays at energies  $> 1$  PeV and gamma rays at energies  $> 1$  TeV thanks to their big size and coverage [42].

Different instruments have been developed over the years with the purpose of studying the EAS on Earth's surface. The detailed study of the characteristics of the air showers (such as lateral structure, size, age, energy, particle content, etc.) is an important activity inside the field of cosmic rays since it allows to obtain information about such extraterrestrial radiation at high energies.

How the measurements of the instruments are interpreted depends on the simulations of the interactions between the primary particles and the particles in the atmosphere. Such simulations depend strongly on the modeling of the hadronic interactions and their predictions at high energies have systematic uncertainties associated with them, which have an important influence on the measurement of the primary cosmic ray energy and the cosmic ray mass composition [101].

Over the last years, progress has been made to increase the sensitivity of the air shower detectors in the energy region of TeV that overlaps with the energy range accessible to direct measurement instruments [101]. This translates into the accumulation of much higher statistics and opens a new window to study the cosmic ray energy spectrum from 1 TeV to 1 PeV which has been barely explored. Such achievement was done thanks to the new generation of indirect experiments which employ more refined techniques for the study of cosmic rays. In the following, some of the techniques employed in the air shower detection of cosmic rays are briefly described [42]:

**Particle detector arrays** : This is the most common method employed in the detection of EAS and it is based on the observation and sampling, at ground level, of the particle disk generated by the cosmic rays when they interact with the atmosphere. The sampling is performed using particle detectors [42]. Unlike balloon borne or space borne instruments, the particle detector arrays can't measure the primary cosmic ray in a direct way. Instead, particle array detectors measure the secondary particles of air showers at ground with particle detectors such as: photomultipliers, scintillator detectors, resistive plate counters, among others. These instruments have a large effective area ( $10^5$  m or greater), which allow them to perform observations at energies above TeV where the flux of cosmic rays is low. Also these instruments have a very large duty cycle and doesn't require special climatological conditions for the measurements. The main disadvantage of this method is that it depends on hadronic interaction models to estimate the energy of the air showers and the nature of the primary particle. Some of the observatories that nowadays employ this method to detect cosmic rays at high energies are: IceTop [102], the Pierre Auger Observatory [33], the Telescope Array and TUNKA-Grande [103].

**Imaging Air Cherenkov Telescopes (IACT)** : For this method high angular resolution optical telescopes are used, which record the Cherenkov emissions generated in the air by the EAS. This technique offers a more sensitive and improved angular and energy resolution as compared to particle detector arrays. The air Cherenkov detectors only detect events within their field of view, which is very limited. The main disadvantage of this method is that it requires very specific climatological conditions, such as a clear

sky, no rain precipitation and low atmospheric pollution. Besides, these detectors can only be used mostly in clear moonless nights [42]. H.E.S.S. [104], VERITAS [105] and MAGIC [106] and TUNKA-133 [103] are experiments that implement this detection technique for studies of cosmic and gamma rays.

**Air fluorescence telescopes** : The air fluorescence is produced by the light emission of nitrogen's molecules in the atmosphere which are excited by the passage of air showers and it is mainly isotropically emitted in the range of  $\lambda=300-400$  nm, hence, air fluorescence can be detected (in principle) from all directions. The detectors that employ this technique can monitor a big volume of the atmosphere over a large surface. These detectors can estimate the energy of the air shower almost independently of the hadronic interaction model. But, just like the IACT's, this method requires clear moonless nights, no rain precipitation and low atmospheric pollution. The Telescope Array observatory employs this technique on the search for Ultra High Energy Cosmic Rays [107].

**Radio emission detection** : This technique focuses on the detection of radio frequency pulses produced by air showers [42]. The radio emission of an air shower provides additional energy calibration, particle track recovery and allows the detection of highly inclined air showers. The combination of radio detection techniques and particle detector arrays will provide a unique tool to study the energy spectrum and composition of cosmic rays over a broad energy range. The first detector to employ this technique for the study of cosmic rays was LOPES [108]. LOFAR [109], the Pierre Auger observatory [33] and TUNKA-Rex [103] are experiments that employ this technique for the detection of cosmic rays.

As it was mentioned before, the detailed study of the characteristics of the air showers is of great importance due to the information that they can provide on the primary particle. This work is focused on the analysis of the measurements taken by a particle detector array, the HAWC observatory. The HAWC observatory detects  $\gamma$ -rays with energies between 100 GeV and 100 TeV, and cosmic rays on the energy range from 10 TeV to 1 PeV. The science goals, design and detection technique and other important characteristics of this experiment are going to be described in detail in the next chapter. Meanwhile, in the following sections, some of the most relevant indirect method experiments that studied or are studying cosmic rays in HAWC's energy interval with indirect methods are going to be described.

### 3.2.1 ARGO-YBJ

The ARGO-YBJ experiment was a large coverage extensive air shower detector dedicated to the study of cosmic rays and gamma rays in the energy interval of  $E = 20$  TeV - 5 PeV. It was located at Yangbajing, Tibet, at an altitude of 4,300 m a.s.l. (see figs. 3.1) [110]. ARGO-YBJ began its activities on November, 2007 and finished operations on February, 2013 [110].

The ARGO-YBJ detector consisted of an array of Resistive Plate Counters (RPCs) distributed over a flat surface of  $\approx 7,000$   $m^2$ , which were designed to measure the particle densities and the arrival times of the shower front particles. The main array of ARGO-YBJ



Figure 3.1: Region of Yangbajing, Tibet. On the image, the facilities of the experiments *Tibet AS $\gamma$*  (at the center) and *ARGO-YBJ* (on the right) can be seen [111].

was surrounded by a ring of 288 RPC's ( $\sim 20\%$  of physical coverage) as shown in figs. 3.2. The active area of the central carpet was  $\sim 93\%$  [112].

The features of the ARGO-YBJ detector were exploited to perform detailed studies of the lateral distribution of charged particles around the shower axis [113], arrival direction and energy of the primary cosmic rays. According to [113] the LDF that best described ARGO-YBJ's simulated and experimental data was a NKG-like function:

$$\rho(r) = A \left( \frac{r}{r_0} \right)^{s-2} \left( 1 + \frac{r}{r_0} \right)^{s-4.5}, \quad (3.1)$$

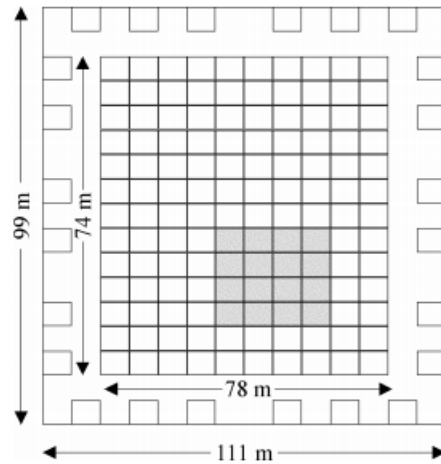


Figure 3.2: ARGO-YBJ detector layout. The central carpet of RPCs extends over 74 x 78 m<sup>2</sup> and it is surrounded by a partially cover guard ring of RPCs stations. [114].

where  $A$  is a normalization factor,  $s$  is the lateral age parameter, and  $r_0$  is a constant scale radius. Here,  $A$  and  $s$  were free parameters, and  $r_0 = 30$  m was found through fits over simulated and real data. To obtain information about the development stage of the shower (age parameter), the ARGO-YBJ collaboration performed fits over the lateral distribution of charged particles around the shower axis using eq. (3.1), as shown in Fig 3.3.

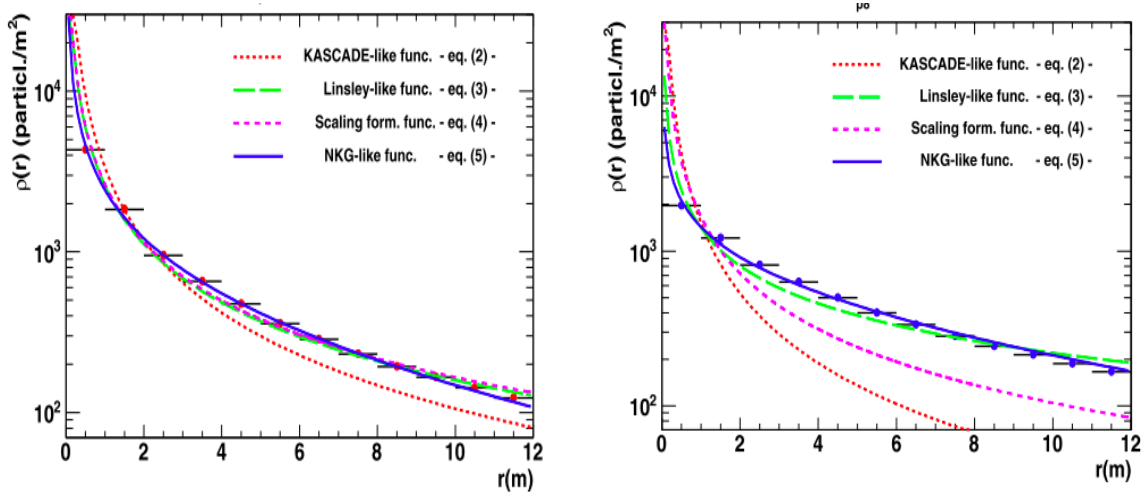


Figure 3.3: Average density distribution of particles around the shower axis as function of the distance to the shower core for a proton induced event (left) of an energy of  $E = 500$  TeV and zenith angle  $\theta < 15^\circ$ , and for an iron induced shower (right) with an energy of 1.4 PeV and zenith angle  $\theta < 15^\circ$  [113]. Both events are from a MC sample of the ARGO-YBJ observatory data. The lines represent fits from different lateral distribution functions chosen by the ARGO-YBJ collaboration for their studies. The solid line represents the fit made with eq. (3.1).

### 3.2.2 KASCADE

KASCADE (Karlsruhe Shower Core and Array Detector) was an array of detectors dedicated to the study of cosmic rays. It successfully collected data between the years from 1996 and 2013. KASCADE was located on the north campus of the Karlsruhe Institute of Technology, Karlsruhe, Germany, at an altitude of 110 m a.s.l. (see figs. 3.4). KASCADE performed cosmic ray measurements in the energy interval  $E = 100$  TeV - 100 PeV [115] to investigate the origin of the knee at  $\sim 4$  PeV in the spectrum of cosmic rays and to determine the composition of cosmic rays in this energy region. In 2003, KASCADE had an upgrade, called KASCADE-Grande [116], which performed measurements on the energy range from  $10^{16}$  eV to  $10^{18}$  eV. The upgrade consisted in the addition of an  $0.5 \text{ km}^2$  array composed of 57 scintillator detectors ( $10 \text{ m}^2$  each), which was called Grande.

The area of the KASCADE array detector was  $200 \times 200 \text{ m}^2$  (see figs. 3.4). KASCADE consisted of three main components: an array of 252 unshielded and shielded scintillation detectors separated 13 m each from each other to measure the electromagnetic and muon components of the air showers, respectively, a central detector equipped with a calorimeter, to measure the hadronic component, and a muon tunnel [115].

The KASCADE collaboration performed studies on the energy spectrum, anisotropies and the primary composition of cosmic rays to investigate the origin of the knee. They also performed tests of hadronic interaction models in the forward region (for which  $Q^2 \sim 0$ , where  $Q^2$  is the squared transferred momentum in the collision).

The KASCADE experiment was designed to measure the electromagnetic, hadronic, and muon components of the air shower [87]. The lateral distributions of electrons, muons and



Figure 3.4: The KASCADE experiment was located at 110 m above sea level ( $1022 \text{ g/cm}^2$ ). The central detector of KASCADE was located at the big central building of the image, it was surrounded by a rectangular array of 252 scintillation detector stations. The stations were distributed over an area of  $200 \times 200 \text{ m}^2$ , and were equally spaced by 13 m [117].

hadrons of the shower disk were studied with KASCADE in details at energies from  $10^{14} \text{ eV}$  up to  $10^{17} \text{ eV}$ . The KASCADE collaboration found that, at least for  $r = 10 \text{ m}$  to  $200 \text{ m}$ , the lateral density distribution of such components could be described by a NKG function,

$$\rho = N \cdot \bar{c}(s) \cdot \left(\frac{r}{r_0}\right)^{s-\alpha} \left(1 + \frac{r}{r_0}\right)^{s-\beta}, \quad (3.2)$$

where  $N$  is the number of charge particles,  $r_0$  is a scale parameter,  $\bar{c}(s)$  is a normalization factor given by

$$\bar{c}(s) = \frac{\Gamma(\beta - s)}{2\pi r_0^2 \Gamma(s - \alpha + 2) \Gamma(\alpha + \beta - 2s - 2)}, \quad (3.3)$$

and  $s$  is the lateral shower age. Here  $N$  and  $s$  are free parameters, while  $r_0$ ,  $\alpha$  and  $\beta$  are constants obtained from MC simulations.

According to MC data  $\alpha = 2$ ,  $\beta = 4.5$  and  $r_0 = 80 \text{ m}$  for electrons. Fig. 3.5 shows the measured lateral distributions for electrons with KASCADE for vertical data fitted with eq. (3.2).

The muon lateral distribution is also well described by eq. (3.2) as reported in [87, 88]. The KASCADE collaboration found that the optimum values for the constants in eq. (3.2) in case of muons are  $\alpha = 1.5$  and  $\beta = 3.7$ , when  $r_0 = 40 \text{ m}$  according to MC simulations. Examples of the reconstructed muon lateral distributions measured by KASCADE for vertical EAS along with the results of the fit with eq. (3.2) are presented in figs. 3.5.

The lateral particle and energy densities for hadron induced air showers at KASCADE were also studied (see figs. 3.6). Again, the fit that best represents the lateral distribution was obtained by applying eq. (3.2). The measured lateral distributions for the hadronic component with KASCADE for  $\theta < 18^\circ$  fitted with eq. (3.2) are presented in figs. 3.6 [87]. The KASCADE collaboration found that the optimum values for the constants in case of hadrons are  $\alpha = 2$  and  $\beta = 4.5$ , when  $r_0 = 10 \text{ m}$  according to MC simulations. A value for the scale radius was fixed to  $r_h = 10 \text{ m}$ .

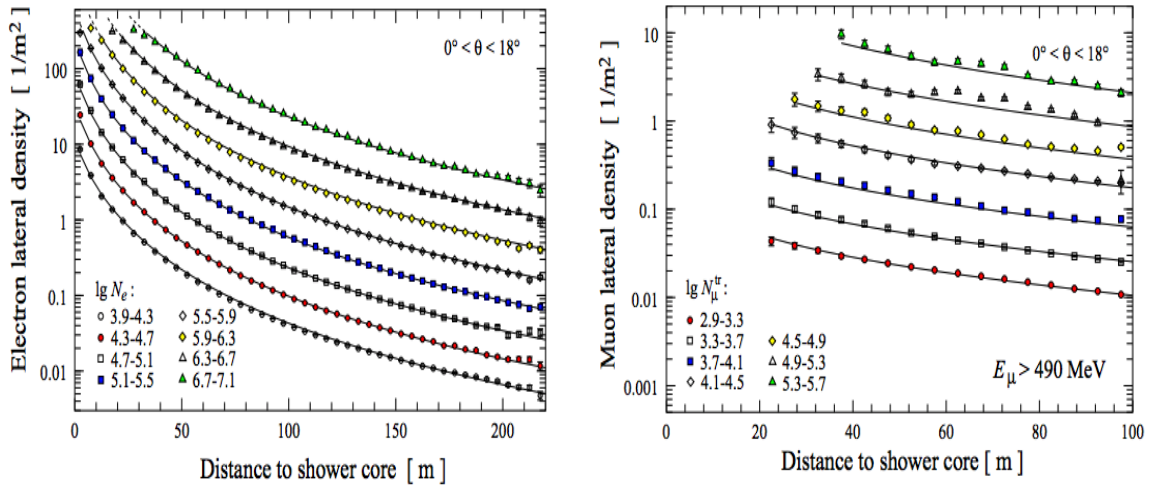


Figure 3.5: The lateral distributions of electrons above 5 MeV of kinetic energy measured with KASCADE for  $\theta < 18^\circ$  and different shower size ranges,  $N_e$ , are presented on the left panel, while the lateral density distributions of muons measured with KASCADE for an energy threshold of 230 MeV for EAS with  $\theta < 18^\circ$  and different truncated muon number ranges are shown at the right panel. The truncated muon number,  $N_\mu^{tr}$ , is the number of muons detected within a distance from 40 m to 200 m from the shower axis. The densities of particles are represented by data points. The lines represent the fits with the NKG function (3.2) to KASCADE experimental data (statistical errors are smaller than the size of the data point in most cases).

### 3.2.3 TAIGA

The TAIGA observatory (*Tunka Advanced Instruments for cosmic rays physics and Gamma Astronomy*) is located at the Tunka Valley, Russia at an altitude of 675 m a.s.l. and has a total area of about 3 km<sup>2</sup>. TAIGA has three different detector systems with distinct measurement techniques for the detection of cosmic rays on the energy range from 100 TeV to several 100's of PeV (see figs.3.7) [118]:

**TUNKA-133:** This is an air Cherenkov detector array composed by 175 wide-angle Cherenkov detectors distributed over an area of 3 km<sup>2</sup>.

**TUNKA-Rex:** It is a radio detector array, which consist of 63 antennas that are distributed over the area of TUNKA-133.

**TUNKA-Grande:** It is a particle detector built from part of the instrumentation left by the KASCADE-Grande experiment [116]. It is composed by 19 scintillation stations each with an area of 10 m<sup>2</sup>, also distributed within the area of TUNKA-133. All the stations of TUNKA-Grande operate simultaneously with the antennas of TUNKA-Rex.

So far, some of the main results that have been obtained by the TAIGA collaboration are related with the all particle energy spectrum and with the reconstruction methods of air showers using Cherenkov light [103].

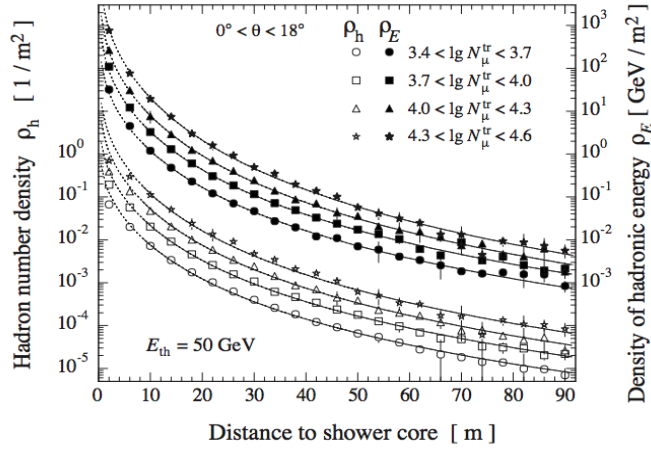


Figure 3.6: The open symbols represent the hadron lateral distribution density measured with KASCADE for  $\theta < 18^\circ$  (left scale), and the filled symbols represent the corresponding lateral energy density, while the curves corresponds to the respective fits with the NKG function (3.2) over the data. The full lines represent the fits applied to the data within the range of  $8 \text{ m} \leq r \leq 90 \text{ m}$ , while the dashed lines are extrapolations to smaller distances, where data was removed because of saturation effects near the shower core [87].

For cosmic ray ground observations, one of the most important observed features is the lateral distribution of air showers, from which most shower observables are derived, and for the TAIGA experiment this is not the exception.

The lateral distribution of charged particles and radio emission have been studied in TUNKA using TUNKA-Rex and TUNKA-Grande. An example of the lateral distribution of radio emission measured with TUNKA is shown in figs. 3.8. This information is useful for energy calibration of EAS in a model independent way [119].

### 3.2.4 Observatories in process of upgrading

Different experiments of PeV cosmic rays are now under upgrading. Some of them are listed below.

**IceTop** The IceCube observatory focuses on the research of high energy neutrinos, but thanks to its surface array, IceTop, it can also study cosmic rays. The IceTop array is under an upgrade wich will allow it to measure cosmic rays in the energy range from 100 TeV to 1 EeV with better precision. The IceCube collaboration will upgrade IceTop with scintillator detectors and radio antennas [120].

**LHAASO** The Large High Altitude Air Shower Observatory already completed its first construction stage and the collaboration of LHAASO reported its first results at the 36th International Cosmic Ray Conference [121]. The complete array of LHAASO will consist on an array of plastic scintillators distributed over an area of  $1 \text{ km}^2$ , an array of 1146 water Cherenkov tanks placed underground, a closed facility with a surface water

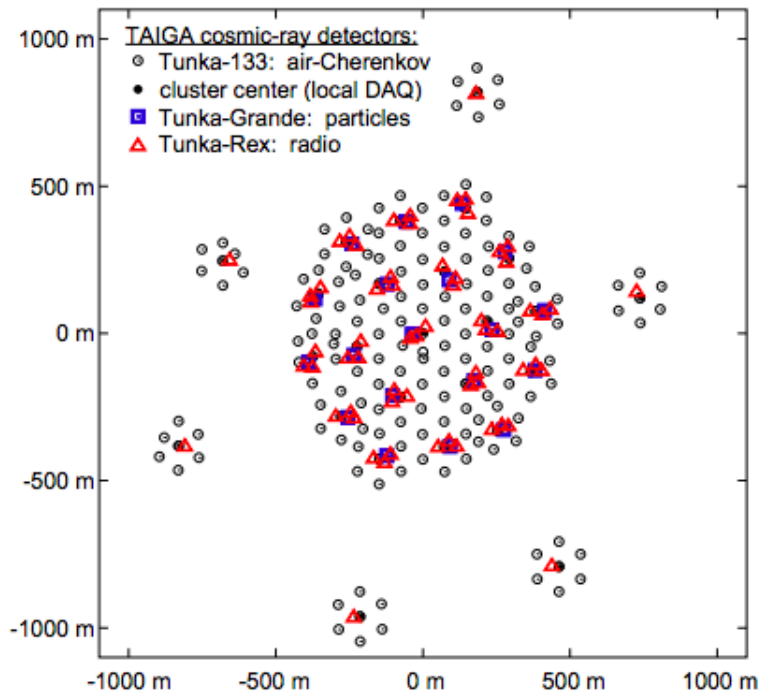


Figure 3.7: TAIGA is composed by 19 inner clusters and six outer clusters of cosmic ray detectors. Each of the inner clusters has three antenna stations (Tunka Radio Extension or TUNKA-Rex), seven photomultiplier detectors dedicated to the measurement of air Cherenkov radiation (TUNKA-133) and one scintillator detector for the measurement of electrons and muons (TUNKA-Grande). On the other hand, each of the outer clusters has only one antenna station and seven photomultiplier detectors [118].

Cherenkov and 12 IACTs. LHAASO will study cosmic rays of energies from 1 TeV to 1 EeV [122].

**Telescope Array** The construction of the Telescope Array low energy Extension (TALE) allowed the TA to reduce its energy threshold down to 4 PeV. TALE consists on ten fluorescence detectors. With this extension, the TA will study cosmic rays in the energy range between 4 PeV and 100 EeV [123, 124].

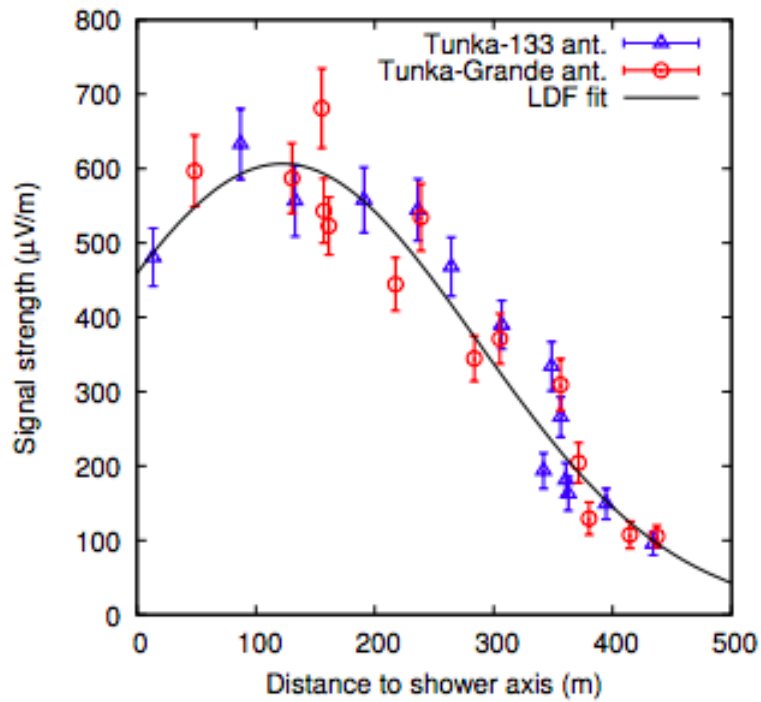


Figure 3.8: Lateral distribution of radio emission of an air shower event from a jointly measurement by TUNKA-Rex and TUNKA-Grande for energies above 100 TeV to 1 EeV. The curve represents the best lateral distribution function fit that best describes the shape of the data [119].

# Chapter 4

## HAWC Observatory

*“Space, is big. Really big. You just won’t believe how vastly hugely mind-bogglingly big it is. I mean you may think it’s a long way down the road to the chemist, but that’s just peanuts to space. Listen...”*

-Douglas Adams, *The hitchhiker’s guide to the galaxy*.

The High Altitude Water Cherenkov (HAWC) gamma-ray observatory is a ground-based air shower detector designed to study the sky in gamma-ray energies between 100 GeV and 100 TeV, however thanks to its location and design it can also measure cosmic rays up to 1 PeV. HAWC is located on the Pico de Orizaba National Park at 4100 m a.s.l., between the Citlaltepétl (Pico de Orizaba) Volcano and the Sierra Negra Volcano, in the state of Puebla, Mexico (see fig. 4.1). On March 20th, 2015, HAWC entered officially into operation, although the observatory had been already performing measurements along different development stages thanks to its modular design. HAWC will end its data taking period on 2025 and then the whole instrument will be dismantled to ensure the preservation of the Pico de Orizaba National Park’s protected area.

### 4.1 Science goals

The main science goals of HAWC are to survey the sky in gamma rays through different astrophysical windows, to search for Galactic TeV sources of gamma rays and to understand how the high energy cosmic rays are accelerated and propagate through the Galaxy and the Universe.

HAWC’s science objectives are broad and involve the study of key areas of astronomy, astrophysics and particle physics, in particular [125–128]:

- To extend the gamma ray observations up to 100 TeV.
- To discover and to study galactic and extra-galactic gamma ray and cosmic ray sources.
- To investigate the acceleration of primary cosmic rays at astrophysical sources.
- To explore the energy spectrum of cosmic rays in the energy interval between 10 TeV and 1 PeV.



Figure 4.1: HAWC is an air shower detector designed to study the sky in gamma rays ( $E = 100 \text{ GeV} - 100 \text{ TeV}$ ), and cosmic rays (up to  $1 \text{ PeV}$ ). The experiment is located at  $4100 \text{ m a.s.l.}$  (below the shower maximum,  $640 \text{ g/cm}^2$ ) on the slopes of the Pico de Orizaba Volcano in Puebla, Mexico. Thanks to its high altitude, HAWC can measure air showers with energies as low as  $100 \text{ GeV}$  (*Image source: HAWC collaboration*).

- To search phenomena related with physics beyond the Standard Model, such as Lorenz invariance violation, primordial black holes and signals from dark matter.

The detailed study of the sky at high energies by measuring different wavelengths (multi-wavelength astrophysics) and different types of particles (multi-messenger astrophysics) are essential to understand the Universe around us. HAWC, as a high energy gamma ray and cosmic ray detector, is involved in multi-wavelength and multi-messenger campaigns, sharing its observational data with different experimental collaborations such as: VERITAS [105], MAGIC [106], HESS (air Cherenkov telescopes) [104], IceCube [102], ANTARES (neutrino telescopes) [129], SWIFT (X-ray telescopes) [130], Fermi-LAT (GeV gamma-ray telescope) [131], and LIGO [132], Virgo (gravitational wave observatories) [133].

On the field of gamma rays, the HAWC science program is dedicated to monitor galactic

and extra-galactic sources and to study the gamma ray energy spectra of the objects. This later helps to distinguish between leptonic and hadronic scenarios for the production of gamma rays. This knowledge can contribute to the understanding of cosmic ray acceleration mechanisms. On the galactic side, HAWC surveys astrophysical sources such as the Crab nebula (see fig. 4.2), supernova remnants (SNRs), binary systems [134], extended regions such as Cygnus, the Galactic plane [135], young star clusters and Fermi Bubbles [136], among others.

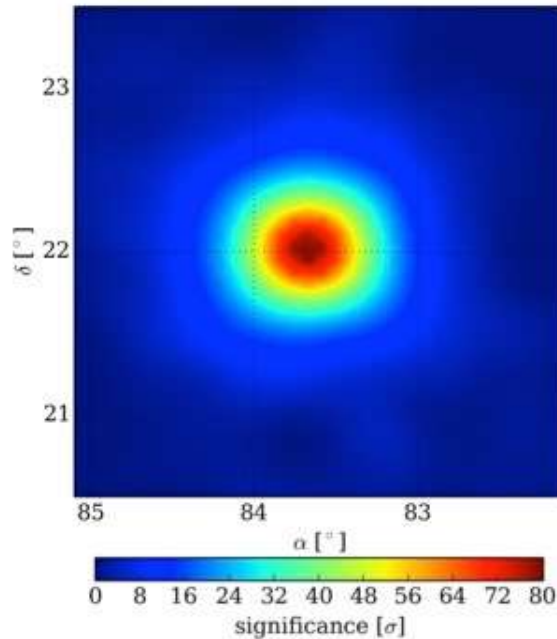


Figure 4.2: The first TeV gamma-ray source to be detected in the story of the gamma-ray astronomy was the Crab Nebula [137]. It is a steady source of TeV gamma rays, making of it a standard candle to validate the performance of any ground-based gamma ray detector. The image is a significance map of gamma ray signals detected by HAWC in the direction of the Crab nebula. *Image source:* [138].

On the other hand, on the extra-galactic area, the HAWC collaboration measures the emission of photons on the energy range of TeV coming from Active Galactic Nuclei (AGNs). It is also expected that it could detect new gamma ray sources and Gamma Ray Bursts (GRBs).

The HAWC collaboration also focuses on the research of cosmic rays. In this regard, the studies involves the investigation of the composition and the energy spectrum of primary cosmic rays [139, 140], which is important to comprehend the nature of the nearby astrophysical sources, as well as the acceleration and propagation of cosmic rays. HAWC's collaboration also expects to contribute on the search for high energy cosmic ray sources and in the understanding of the acceleration mechanisms of primary cosmic rays in the Universe. HAWC is also capable of measuring the cosmic ray anisotropy at TeV energies [141]. HAWC has

an instantaneous 2 sr field of view, which is equal to a 15% of the sky. After a cycle of 24 hours HAWC maps two thirds of the celestial vault. Thanks to it's wide field of view, the HAWC observatory is able to make detailed maps of the sky on gamma rays with unprecedented statistics, albeit with a lower angular resolution compared to an IACT. With HAWC's data it is possible to create stellar maps, like the one in fig. 4.3, where some galactic and extra-galactic sources of high energy gamma rays are portrayed, like the Crab Nebula and the Milky Way. Finally to demonstrate the potential of HAWC for new discoveries, the HAWC collaboration has reported new astrophysical sources such as the jets of the microquasar SS443 [142] and the extended halos of Geminga (PSR B0633+17) and Monogem (PSR B0656+14) [143] and even that haven't yet been observed by other instruments, for example, the 2HWC J2006+341 source [144].



Figure 4.3: Stellar map created with HAWC's gamma ray observational data with an effective time of 340 days (taken between November 2014 and November 2015). On the map, the galactic plane, the Crab nebula and other high energy galactic and extragalactic sources (Markarian 501 and Markarian 421, as examples of extragalactic objects) are visible. Several constellations are shown on the map as a guide (*Image source:* [138]).

## 4.2 The HAWC detector

HAWC consists of a close-packed array of 300 water Cherenkov detectors (WCD) distributed over a flat surface of 22,000 m<sup>2</sup> with a 62% of physical coverage. Each WCD is 4.5 m high, 7.3 m in diameter, and has four upward-facing photomultipliers (PMTs) distributed at the bottom of the WCD (see fig. 4.4), giving a total of 1,200 PMTs [145]. The detector also contains 60 ML of ultra-pure water each. The complete array of the observatory is presented at fig. 4.5.

HAWC is able to discern between air showers generated by gamma rays from those induced by cosmic rays (Gamma/Hadron separation) from the smoothness of the shower front and to resolve the core position of the air shower at ground level thanks to its large coverage. For the detection of shower particles (whether induced by gamma rays or cosmic rays), HAWC employs the WCDs. The relativistic particles that passes through the water tanks produce Cherenkov radiation, which is measured with the PMTs.

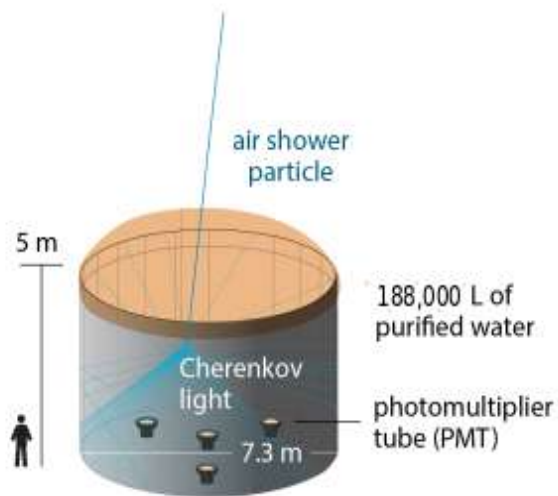


Figure 4.4: Left: sketch of a WCD of HAWC. Due to water's refraction index and its low cost, water is employed to fill in the WCDs [146]. Right: HAWC's site counts with a continuous purifying water system, which prevents the presence of impurities, contaminants or microorganisms inside each WCD of the experiment. In the figure the purifying water system can be seen (*Image source: HAWC Collaboration*).

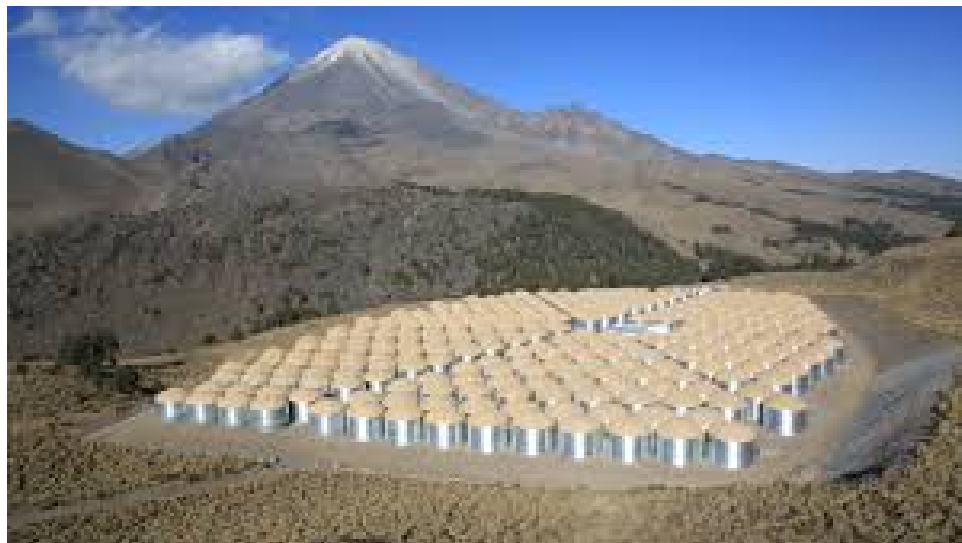


Figure 4.5: HAWC main array of 300 WCD. The observatory takes measurements day and night independent from weather conditions. At the center of the array there is a small building called counting house, which is home of the Data Acquisition Center. The *Pico de Orizaba (Citlaltépetl)* Volcano can be observed in the background. (*Image source: HAWC collaboration*).

### 4.3 Cherenkov Radiation

The HAWC observatory uses the water Cherenkov technique, which was pioneered by the Milagro Collaboration [147], for the detection of relativistic particles at water, recording the air shower passage at ground level. This kind of detection method measures the Cherenkov radiation generated by the secondary particles of an air shower as they propagate through the water in the WCD.

The Cherenkov radiation receives its name after the Russian physicist Pavel Alekseyevich Cherenkov, who was the first scientist in detecting this type of radiation.

When a charged particle travels through a transparent refractive and dielectric medium at speed  $u$ , such that  $u$  is greater than the speed of light in the aforesaid medium the Cherenkov light is produced [61, 148]. The Cherenkov effect was theoretically first predicted by Oliver Heaviside in 1888 [149, 150], discovered experimentally by P. Cherenkov [151] and later interpreted by Il'ja Frank and Igor Tamm [152] in 1937. Cherenkov, Frank and Tamm shared the Nobel Prize in physics on 1958 for their work on the Cherenkov radiation. The Cherenkov light is the electromagnetic equivalent of a sonic boom but in a transparent medium.

The Cherenkov radiation is emitted around a small cone through the direction of propagation of the particle, as depicted on a two-dimensional diagram in fig. 4.6. The aperture angle of the cone is given by:

$$\cos \theta = \frac{c}{un} = \frac{1}{\beta n}, \quad (4.1)$$

where  $\beta = u/c$  is the relative velocity of the charged particle in the medium,  $n$  is the refraction index of the medium and  $c$  is the speed of light in the vacuum [42].

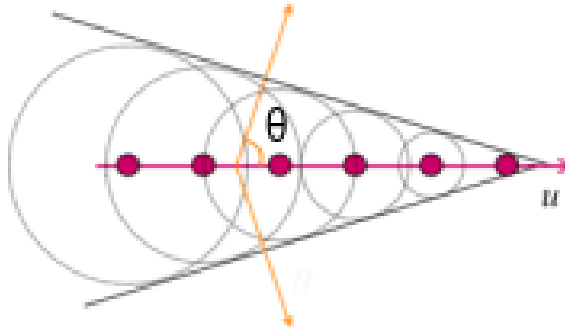


Figure 4.6: When a charged particle, let's say an electron, travels at a speed greater than the speed of light in a transparent medium, it produces conical wave fronts of Cherenkov radiation. The Cherenkov light is emitted at an angle  $\theta$  with respect to the particle trajectory. The refraction index of the water is 1.33 then, if we assume  $u \approx c$ , the angle at which the Cherenkov photons are emitted is  $\theta \sim 41^\circ$ . *Image credit: [153]*.

From eq. (4.1) it can be seen that there exist a threshold condition for the production of Cherenkov radiation. Such condition is

$$\beta_{th} n = 1, \quad (4.2)$$

which tells us that only charged particles with  $\beta > 1/n$  will produce Cherenkov radiation in a transparent medium [148].

The kinetic energy threshold for emission of Cherenkov radiation by an electron in a medium of refraction index  $n$  can be obtained from the following expression [148]:

$$E_{th} = 511 \text{ keV} \left[ \left( 1 - \frac{1}{n^2} \right)^{1/2} - 1 \right]. \quad (4.3)$$

The kinetic energy threshold for an electron in air is  $E_{th} = 21 \text{ MeV}$  and the maximum emission angle of the Cherenkov cone is  $\theta_{max} = 1.3^\circ$ . On the other hand, the threshold energy for the production of Cherenkov light by electrons in water ( $n_{water} = 1.33$ ) is 263 keV according to eq. (4.3), and following eq. (4.1)  $\theta_{max} \approx 41^\circ$ .

The energy loss of charged particles by Cherenkov radiation is almost negligible and represents only  $\approx 0.1\%$  of the energy loss by ionization. The number of photons,  $N_f$ , emitted by an electron per path length of travel, as a function of the refraction index, is [148]:

$$N_f = 2\pi \cdot z^2 \cdot \alpha \cdot l \cdot \left( \frac{1}{\lambda_2} - \frac{1}{\lambda_1} \right) \cdot \left( 1 - \frac{1}{\beta^2 n^2} \right), \quad (4.4)$$

where  $z$  is the particle charge,  $\alpha = 1/137$  is the fine structure constant,  $n$  is the media refractive index,  $l$  is the length of the medium, and  $\lambda_1$  and  $\lambda_2$  are extreme points of the emitted wavelength interval. Using eq. (4.1), the eq. (4.4) can also be expressed as follows [42]:

$$N_f = 2\pi \cdot z^2 \cdot \alpha \cdot l \cdot \left( \frac{1}{\lambda_1} - \frac{1}{\lambda_2} \right) \cdot \sin^2(\theta). \quad (4.5)$$

According to eq. (4.5), an electron in air ( $n_{air} = 1.00029$ ) at sea level will produce  $\approx 30$  photons/m with wavelengths between 350 and 500 nm.

## 4.4 Photomultiplier tubes, PMTs

Once the air shower secondary charged particles have spread inside the WCDs, the produced Cherenkov radiation is captured by the photomultiplier tubes placed upward-facing at the bottom of each WCD. A PMT is a vacuum sealed optical detector that works under the photoelectric principle [154]. There are two models of PMTs employed at the HAWC observatory. The first model is the high quantum-efficiency Hamamatsu R7081 of 10-inch, which gives HAWC an enhanced sensitivity to low-energy air showers [154]. The second model is the Hamamatsu R5912 of 8-inch [154]. The PMTs from the second model were inherited from the MILAGRO experiment [147]. Each WCD has one Hamamatsu R7081 PMT anchored to the bottom surrounded by 3 Hamamatsu R5912 PMTs arranged in an equilateral triangle. All the PMTs installed at HAWC have the upper part of the tube covered by a glass shell whose inner face is a semi-conductive film called photocathode. The left panel of fig. 4.7 shows a schematic diagram of a general PMT, and the right panel shows a photograph of a HAWC PMT.

The photons that reach the photocathode, according to the photoelectric principle, can produce electrons from the photocathode surface. These free electrons are accelerated towards a metallic plate (called dynode) thanks to a potential difference. Each PMT has a chain of 10

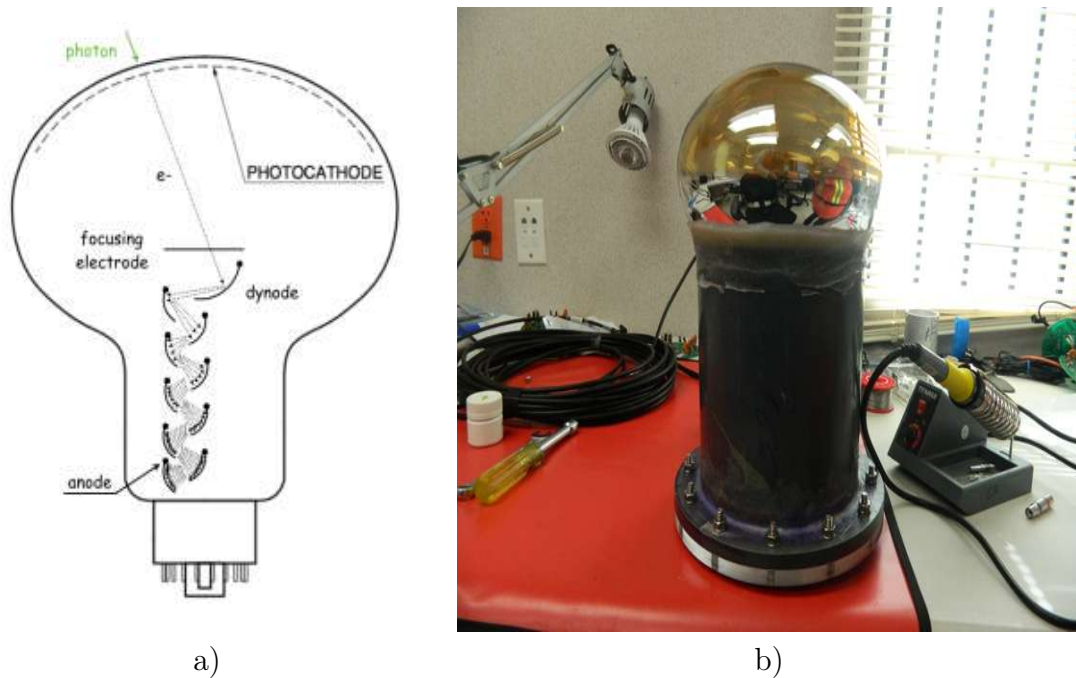


Figure 4.7: a) PMT diagram taken from [154]. b) Photography of one of the Hamamatsu R5912 8-inch PMTs used in HAWC (*Image source*: HAWC collaboration).

consecutive dynodes placed inside. When a primary electron collides with the first dynode produces a new group of electrons, which are then accelerated towards the second dynode generating a bigger group of electrons. This process continues copiously until the electrons reach the last dynode of the PMT. Once the electrons have reached the last dynode, all of the electrons are transferred to the anode where they are collected and sent to the PMT output channel.

#### 4.4.1 Data Acquisition System

Each PMT sends the signal through a coaxial wire RG-59 to the counting house (data acquisition center). Inside the counting house, the signal sent by the PMTs is received by the data acquisition system (DAQ) [140, 154]. A schematic diagram of this process is depicted in fig. 4.8. The DAQ is in charge of amplifying, giving shape, analyze and digitize the signal from the PMTs. The electronic analog and digital devices (front end board, FEB) are in charge of amplifying and giving shape to the signal [140, 154]. The analog FEBs compare the signal against two thresholds of different voltages, high (4 photoelectrons, PEs) and low ( $1/4$  PEs) ones, respectively. Each time that the signal goes through one of the thresholds it generates a pulse with a time length equal to the time that the signal spent above the specified threshold (see fig. 4.9). The digital FEBs digitize and give shape to the pulses with the Time over Threshold (ToT) technique. The result of this technique are two-edge and four-edge signals [140]. A two-edge signal is generated when the signal crosses the low voltage threshold, but not the high voltage threshold. When the signal crosses both thresholds a four-edge signal is generated (see fig. 4.9). Once the signal has

been characterized and digitize it is sent to the Time Digital Converter (TDC), where the signal is converted to binary system, and later is sent to an on-site cluster of servers where a selection process is performed to reduced the data rate from  $\sim 450$  MB/s to  $\sim 20$  MB/s, which generates approximately 1.7 TB of data per day. The selection is done by a trigger that requires that the signal from at least 28 PMTs is received in a time interval of 150 ns. The corresponding trigger rate is 25 kHz [145]. For the reconstruction, the hits (or PMTs with signal during an event) are saved up to 500 ns before the trigger and up to 1 minute after the trigger.

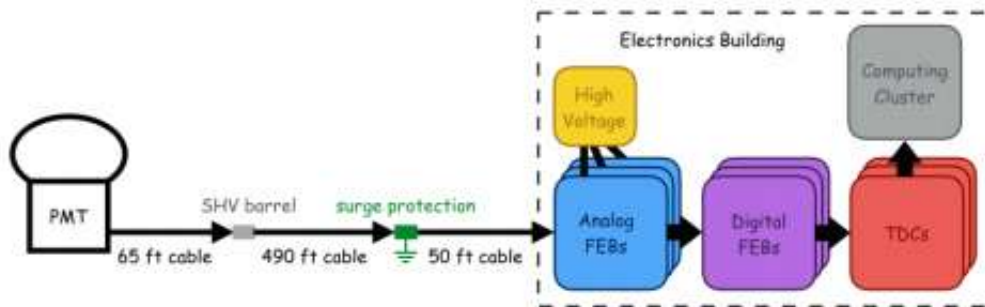


Figure 4.8: Scheme of the PMT signal processing in HAWC (*Image source:* [154]).

After this point, the data has been digitize and stored in hard drives to continue with the online/offline reconstruction of the detected air showers [155, 156].

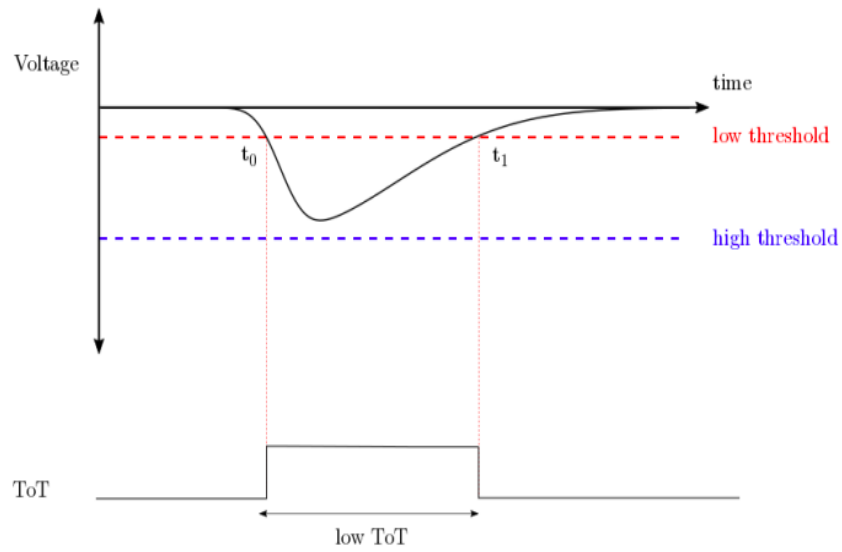
The DAQ is plugged to a cluster of servers that performs the online air shower event reconstruction in real time, which allows to monitor the data in a fast way. The offline air shower event reconstruction is carried out with more refined algorithms (AERIE [157]) due to the longer period of time that it takes. The data generated from the offline reconstruction is used for the detailed analysis of air shower events. The offline air shower reconstruction will be described with more detail on the next section.

## 4.5 Air shower reconstruction

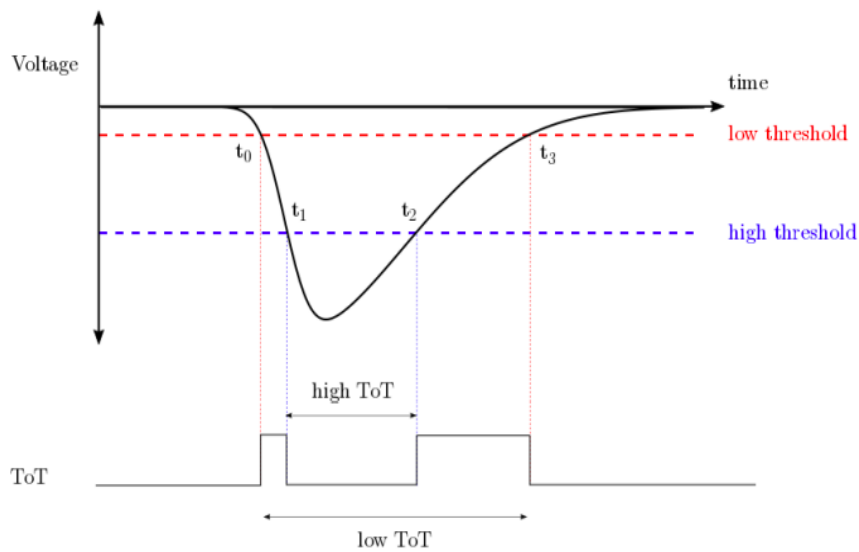
The offline air shower reconstruction takes place once the raw data from the PMTs has been successfully acquired. Below are described the reconstruction steps to get the main air shower parameters.

### 4.5.1 Core position

The first step on the reconstruction of an air shower is to identify the position where the shower axis lands on the detector or, in other words, to find the shower core position at ground level. The shower axis is defined as the path between the primary particle and the point at the detector where it would have landed if it hadn't interacted with the atmosphere. The shower core is the point of maximal energy deposition and highest particle density, and it's position is employed for the reconstruction of the primary cosmic ray arrival direction and



a)



b)

Figure 4.9: The ToT method applied to the PMTs signals from HAWC. The curves represent the pulses from a PMT of the experiment. On a) the curve doesn't cross the high voltage threshold, generating a two-edge event. While on b) the pulse crosses both thresholds, generating a four-edge event. *Image source:* [140].

for the Gamma/Hadron separation. An electromagnetic induced air shower has a smoothed distribution of deposited charge, in the core region has the maximal deposition of charge, and as the distance grows from the core the deposited charge on the detector falls. Meanwhile, the charge distribution of a cosmic ray induced shower has an irregular and clumpy distribution of

deposited charge (see fig. 4.10). It is of great importance to make the most precise estimation of the core position, due to its impact on the subsequent air shower reconstruction steps. A first rough estimation of the core position is made by estimating the *center of mass* of all the hits located within the array detector. This first estimation gives a first calculation of the shower core position. The *center of mass* is given by the following expression [155]:

$$\vec{r}_{cm} = \frac{\sum \vec{r}_i q_i}{\sum q_i}, \quad (4.6)$$

where  $r_i$  is the position of the  $i$ -th PMT in the detector coordinate system and  $q_i$  is the effective charge detected by the  $i$ -th PMT. For a detailed and quick estimation of the core position the Super Fast Core Fitter (SFCF) is implemented. The SFCF is a simplification of a modified NKG-like function that includes a Gaussian component. The latter is used to find the core by a  $\chi^2$  fit over the lateral distribution of the deposited charge of the event using the *center of mass* as a first approximation. The SFCF has the form [145]:

$$S_i = S(A, \vec{x}, \vec{x}_i) = A \left( \frac{1}{2\pi\sigma^2} e^{-|\vec{x}_i - \vec{x}|^2/2\sigma^2} + \frac{N}{(0.5 + |\vec{x}_i - \vec{x}|/r_0)^3} \right), \quad (4.7)$$

where  $S_i$  is the signal at the  $i$ -th PMT,  $\vec{x}$  is the core position,  $\vec{x}_i$  is the position where the measurement was made,  $r_0 = 124.21$  m is the Molière radius,  $\sigma = 10$  m,  $N = 5 \cdot 10^5$ , and  $A$  is the signal amplitude. The core position and overall amplitude,  $A$ , are left as free parameters.

In HAWC, the lateral distribution of an event is the effective charge distribution as a function of the radial distance to the shower core position at the shower front coordinate system (see fig. 4.10) [85, 86].

## 4.5.2 Arrival direction

The next step on the reconstruction of an air shower is to reconstruct the arrival direction of the primary particle. The information is obtained from a fit to the arrival times of the shower front.

As a first approximation, the shower front can be portrayed as a plane travelling at the speed of light. This is true near the shower axis, where the secondary particles remain approximately with the same direction of the primary particle, but the secondary particles farther from the shower axis have to travel larger trajectories and, therefore, their arrival times are bigger than at the center, which makes the shower front to curve given its finite velocity. Due to the fact that the shower front has a curvature, a correction must be applied to the data, which takes into account the differences in arrival time among the PMTs near the shower axis and those at the tail of the EAS [140, 145]. In general, the curvature correction of the shower front is of the order of 0.15 ns per meter from the shower core. Finally, a  $\chi^2$  fit over the shower plane is performed. The resulting zenith,  $\theta$ , and azimuth,  $\phi$ , angles of the vector normal to the fitted plane determine the arrival direction of the primary particle [140].

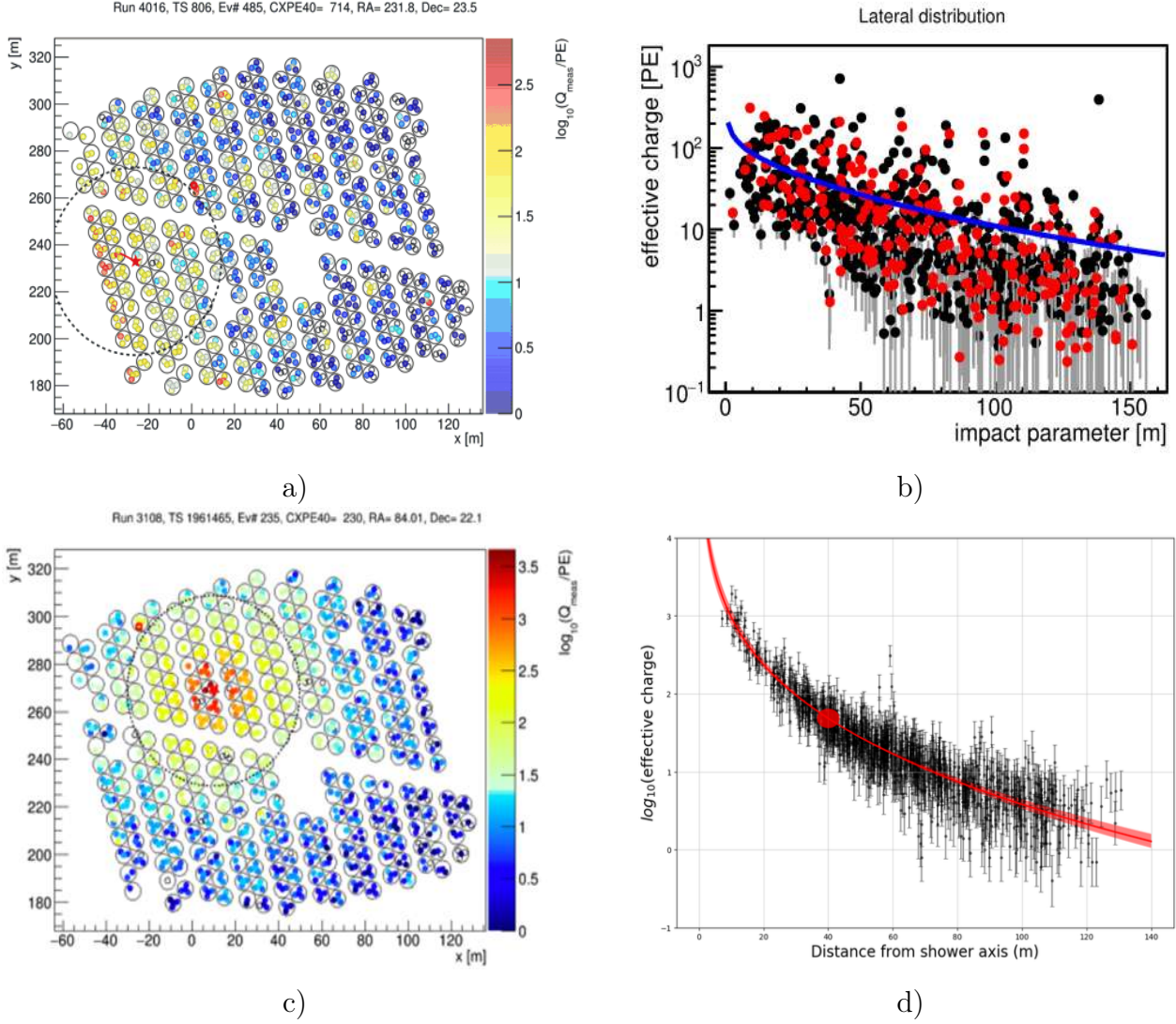


Figure 4.10: Charge distribution of a) a cosmic ray induced event with a primary energy  $E=10^{4.9}$  GeV, and c) a gamma-like event of energy  $E = 56$  TeV both measured with HAWC. For the panels a) and c) the small dots indicate the individual position of each PMT and the big circles stand for the positions of each WCD. The fitted core for each event is denoted by a star. Panel b) shows the lateral distribution of deposited charge around the shower axis for the event displayed at a). The blue line represents the fit applied with eq. (4.7). At d) the lateral distribution of the gamma-like event at c) is shown, where the red band is the best fit to a NKG function (4.8) and the red circle is the optimal radius ( $r = 41$  m), where the uncertainties on the effective charge due to the fit are smaller. It is clear to see from b) and d) that the lateral distribution for the gamma like event is smoother and less clumpy than that for the cosmic ray induced air shower (*Image source: [138, 158]*).

### 4.5.3 Age parameter, $s$

The reconstructed age parameter,  $s$ , measured at HAWC corresponds to the lateral shower age. The age parameter is estimated by performing a fit event by event to the lateral

distribution of effective charge (see fig. 4.10) measured by the HAWC's PMTs. The fit is performed using an NKG-like function [85]:

$$f(r) = A \cdot (r/r_0)^{s-3} \cdot (1 + r/r_0)^{s-4.5}, \quad (4.8)$$

where  $r$  is the radial distance to the shower core on the shower front coordinate system,  $s$  is the lateral shower age,  $r_0=124.21$  m is the Molière radius and  $A$  is a normalization parameter. The age parameter and  $A$  are left as free parameters.

#### 4.5.4 Energy reconstruction

For the reconstruction of primary particle energy the lateral distribution is also needed. By mean of the simulation of proton induced showers, four-dimensional probability tables are built with bins in zenith angle,  $\theta$ , primary energy,  $E$ , PMT distance to the shower core in the shower plane,  $r$ , and deposited effective charge at the PMTs,  $Q_{eff}$ . Given an air shower with reconstructed arrival direction and core position, each PMT contributes with a probability value extracted from the tables even if the PMT didn't recorded a signal: the tables also have the probability that a PMT is not activated. For each possible energy, a likelihood function is calculated as the product of the probability values of the PMTs. The energy bin with the maximum likelihood value is chosen as the best energy estimator of the air shower event [139, 140].

The bins of the proton probability tables are defined as follows:

- Zenith angle bins:
  - $\theta_0 \in [0^\circ, 16.8^\circ]$ ,
  - $\theta_1 \in [16.8^\circ, 35.2^\circ]$ ,
  - $\theta_2 \in [35.2^\circ, 60^\circ]$ .
- Energy bins:  $E \in [70 \text{ GeV}, 1 \text{ PeV}]$ , with a bin width of 0.1 in the logarithm of the energy, this is,  $\Delta \log_{10} E / \text{GeV} = 0.1$ . There are 44 energy bins in total.
- Lateral distance bins:  $R \in [0, 350]$  m, with a bin width of 5 m. 70 radial bins are used.
- Charge bins:  $Q_{eff} \in [1, 10^6]$  PE, where  $\Delta Q_{eff} = 0.15$ . 40 effective charge bins were employed.

#### 4.5.5 Simulation

The generation and propagation of secondary particles from the atmosphere to ground level is simulated via the CORSIKA v740 software package [159]. The hadronic interaction models employed for the simulations are *FLUKA* [80] and *QGSJet-II-03* [77], for the low- and high- energy regions, respectively. The interaction of the secondary shower particles with HAWC's detectors are simulated with HAWCSim which is based on a toolkit developed at CERN called *GEANT4* [160]. The simulated file that is created have the same output as the experimental data files. Both, simulations and experimental data are then reconstructed with the same algorithm.

Eight atomic nuclear species are generated at HAWC's simulations. These species were measured during the flights of the experiments CREAM, PAMELA and AMS. The eight atomic nuclear species that are simulated are  $^1\text{H}$ ,  $^4\text{He}$ ,  $^{12}\text{C}$ ,  $^{16}\text{O}$ ,  $^{20}\text{Ne}$ ,  $^{24}\text{Mg}$ ,  $^{28}\text{Si}$  and  $^{56}\text{Fe}$ , with a differential energy spectrum  $E^{-2}$  between 5 GeV and 3 PeV uniformly distributed with  $r$  over a flat circular surface of 1000 m in radius [92]. The simulations are generated in this way to compensate the statistics for those radial distances and energy bins where the number of events is low. On the other hand, the zenith angle has a total range between  $0^\circ$  and  $70^\circ$  with a  $\sin\theta\cos\theta$  arrival distribution, where  $\theta$  is the shower axis zenith angle.

The package Software for Weighting Events and Eventlike Things and Stuff (SWEETS) [161, 162] adds weights to the simulated data to model isotropic fluxes, point, extended or transitory sources, uniform distributions per unit area on the ground and to simulate specific energy spectra. The weight is added to describe more realistic distributions.

SWEETS adds weight to each type of atomic nucleus according to a double power-law function fitted with observational data from AMS [55], CREAM-II [94] and PAMELA [163] (see figs. 4.11 and 4.12) of the corresponding nucleus. The double power-laws have the form [164]:

$$f(E) = \begin{cases} A \times \left(\frac{E}{E_0}\right)^a, & \text{para } E < E_b, \\ A \times \left(\frac{E_b}{E_0}\right)^{a-b} \left(\frac{E}{E_0}\right)^b, & \text{para } E \geq E_b, \end{cases} \quad (4.9)$$

where  $A$  is a normalization constant at  $E_0$ ,  $a$  is the spectral index for  $E < E_b$ , and  $b$  is the one for  $E \geq E_b$ . Here  $E_b$  is the energy at which the spectral index change.  $E_0$  was fixed to a value of 100 GeV for all nuclear species fits [164, 165].

Tables 4.1 and 4.2 show the best fit parameters, as well as the maximum and minimum associated errors for the parameters  $A$ ,  $a$ ,  $b$ ,  $E_b$  and  $E_0$  [165]. This is the nominal composition model that is going to be used in the present work. Both data and simulations were processed with the same reconstruction algorithms.

### 4.5.6 Simulated data

For this work, the test\_nobroadpulse\_10pctlogchargesmearing\_0.63qe\_25kHzNoise\_run5481 with curvature 1 MC data set was selected. The curvature 1 parameter refers to the correction that was applied over the arrival times of particles of the air shower front to the PMTs due to the curvature of the EAS, which improves the angular resolution of simulated air shower events induced by cosmic rays and detected with HAWC [166].

### 4.5.7 Observables

Some of the reconstructed variables available at HAWC for simulated and experimental data sets are presented below:

**event.hit.channelsIsGood** Gives information about the PMT channel status. It can take values of 1 (channel is good) and 0 (channel is bad).

**stdCuts.isSelected** This observable tells if a hit passes the reconstruction standard cuts. If it takes a value of 0 it means that it did not fulfilled the cuts. If it is equal to 1 it means

	Best fit	Minimum value	Maximum value
Hydrogen			
A [1/(GeV m <sup>2</sup> s sr)]	0.04479	0.04445	0.0451
a	-2.807	-2.818	-2.796
b	-2.658	-2.667	-2.646
E <sub>0</sub> [GeV]	100	100	100
E <sub>b</sub> [GeV]	440.6	511.4	388.2
Helium			
A [1/(GeV m <sup>2</sup> s sr)]	0.03308	0.03289	0.03328
a	-2.734	-2.74	-2.728
b	-2.547	-2.562	-2.53
E <sub>0</sub> [GeV]	100	100	100
E <sub>b</sub> [GeV]	842.4	967.3	746.3
Carbon			
A [1/(GeV m <sup>2</sup> s sr)]	6.947×10 <sup>-6</sup>	6.779×10 <sup>-6</sup>	7.111×10 <sup>-6</sup>
a	-2.756	-2.732	-2.779
b	-2.554	-2.588	-2.519
E <sub>0</sub> [GeV]	1,200	1,200	1,200
E <sub>b</sub> [GeV]	2843	3631	2421
Oxygen			
A [1/(GeV m <sup>2</sup> s sr)]	4.995×10 <sup>-6</sup>	4.909×10 <sup>-6</sup>	5.099×10 <sup>-6</sup>
a	-2.756	-2.732	-2.779
b	-2.554	-2.588	-2.519
E <sub>0</sub> [GeV]	1,600	1,600	1,600
E <sub>b</sub> [GeV]	3791	4841	3227

Table 4.1: The table shows the fit parameters and respective errors of the double power-law functions (4.9) employed in the nominal composition model of HAWC for hydrogen, helium, carbon and oxygen data [165].

	Best fit	Minimum value	Maximum value
Neon			
A [1/(GeV m <sup>2</sup> s sr)]	$6.3 \times 10^{-7}$	$5.967 \times 10^{-7}$	$6.645 \times 10^{-7}$
a	-2.756	-2.732	-2.779
b	-2.554	-2.588	-2.519
E <sub>0</sub> [GeV]	2,000	2,000	2,000
E <sub>b</sub> [GeV]	4738	6051	4034
Magnesium			
A [1/(GeV m <sup>2</sup> s sr)]	$5.683 \times 10^{-7}$	$5.424 \times 10^{-7}$	$5.925 \times 10^{-7}$
a	-2.756	-2.732	-2.779
b	-2.554	-2.588	-2.519
E <sub>0</sub> [GeV]	2,400	2,400	2,400
E <sub>b</sub> [GeV]	5686	7261	4841
Silicon			
A [1/(GeV m <sup>2</sup> s sr)]	$5.71 \times 10^{-7}$	$5.571 \times 10^{-7}$	$5.841 \times 10^{-7}$
a	-2.756	-2.732	-2.779
b	-2.554	-2.588	-2.519
E <sub>0</sub> [GeV]	2800	2800	2800
E <sub>b</sub> [GeV]	6634	8472	5648
Iron			
A [1/(GeV m <sup>2</sup> s sr)]	$2.001 \times 10^{-7}$	$1.965 \times 10^{-7}$	$2.042 \times 10^{-7}$
a	-2.756	-2.732	-2.779
b	-2.554	-2.588	-2.519
E <sub>0</sub> [GeV]	5600	5600	5600
E <sub>b</sub> [GeV]	$1.327 \times 10^4$	$1.694 \times 10^4$	$1.13 \times 10^4$

Table 4.2: Table of the fit parameters and respective errors of the double power-law functions (4.9) employed in the nominal composition model of HAWC for neon, magnesium, silicon and iron data [165].

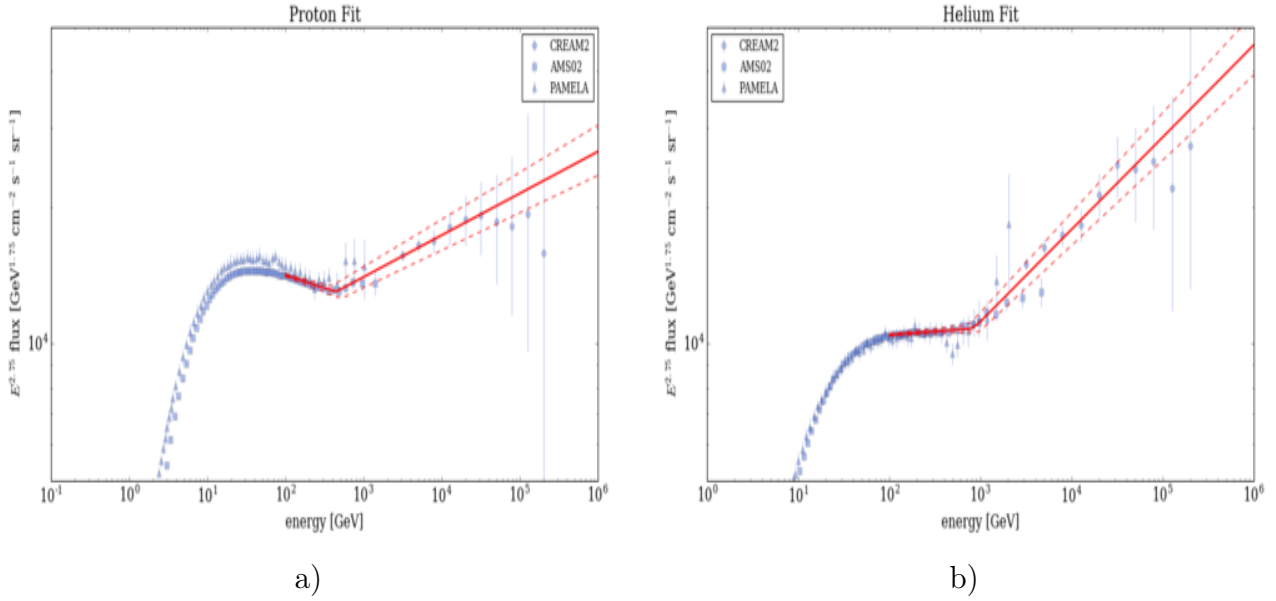


Figure 4.11: The double power-law fit (lines) with eq. (4.9) over the experimental data (points) for different direct measurements for (a) protons, and (b) helium nuclei [165]. These elements are part of the nominal composition model of HAWC.

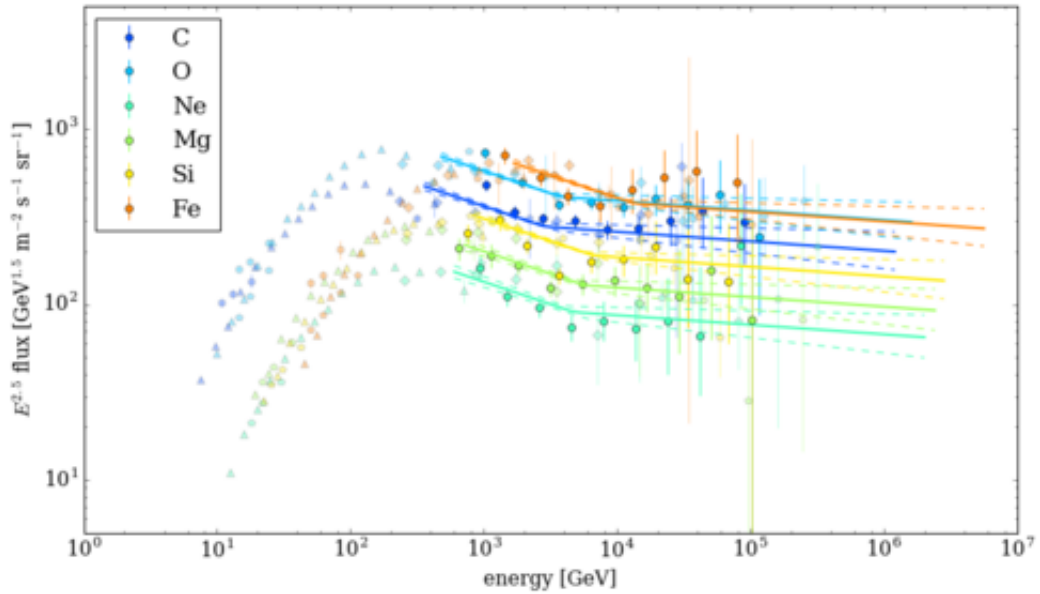


Figure 4.12: The double power-law fit (lines) with eq. (4.9) over the experimental data (points) from different direct measurements for carbon, oxygen, neon, magnesium, silicon and iron nuclei, respectively [165]. These elements are part of the nominal composition model of HAWC.

that the hit PMT passed the standard reconstruction cuts with  $0 < PE < 10000$ ,  $-150 \text{ ns} < T_{window} < 300 \text{ ns}$  relative to the trigger time,  $loTOT < 500$  and was marked as good [167].

**rec.nHit** Number of hits registered at the PMTs after a standard selection.

**rec.coreFiduScale** This is a scale factor related to HAWC's perimeter that indicates where did the shower core landed on the detector array. When  $\text{rec.coreFiduScale} \leq 100$  the reconstructed shower core falls inside the HAWC array.

**rec.coreFitUnc** Shower core error from the reconstruction in units of m.

**rec.coreFitStatus** indicates if the core position reconstruction was successful. If it is equal to zero it means that the fit passed the shower core reconstruction method.

**rec.zenithAngle** Zenith angle of air shower's arrival direction in units of rad.

**rec.angleFitStatus** indicates if the angular reconstruction was successful or not. It can take the following values:  $\text{rec.angleFitStatus} = 0$  if the reconstruction was successful,  $\text{rec.angleFitStatus} = 1$  the reconstruction failed,  $\text{rec.angleFitStatus} = 2$  means that there's no available data,  $\text{rec.angleFitStatus} = 3$  the fit didn't converge.

**rec.protonLheEnergy** Logarithm of the primary energy estimation, assuming that the primary particles are protons using the log-likelihood method described at the sub-section 4.5.4. The energy is expressed in units of eV.

**rec.LDFAge** Lateral shower age,  $s$ . This parameter is calculated by performing a fit over the lateral distribution of an event using the eq. (4.8).

**rec.LDFamp** Resulting amplitude,  $A$ , from the fit over the lateral distribution of an event using the eq. (4.8).

**rec.CxPE40XnCh** Number of channels activated within a small region of radius equal to 40 m.

**rec.nChAvail** Number of channels available at HAWC during the event detection.

**CxPE40** Maximum energy deposited at the PMT with the highest signal outside a region with radius of 40 m.

**rec.coreX** Estimated X position on the shower core at ground level in HAWC's coordinate system in units of m.

**rec.coreY** Estimated Y position on the shower core at ground level in HAWC's coordinate system in units of m.

In the following lines, some additional simulated observables (mc) are listed, which are only found on HAWC's Monte Carlo data sets:

**mc.corsikaParticleId** Primary particle identification used in CORSIKA and HAWC. Some useful particle IDs are:

1: gamma,  $\gamma$ .

14: proton,  $p$ .

402: helium.

1206: carbon.

1608: oxygen.

2010: neon.

2412: magnesium.

2814: silicon.

5626: iron.

**mc.eventWeight** Factor by which an event can be weighted to make its distribution in the area uniform and its energy distribution flat.

**mc.coreX** Shower core's true X position at ground level in HAWC's coordinate system in units of m.

**mc.coreY** Shower core's true Y position at ground level in HAWC's coordinate system in units of m.

**mc.zenithAngle** True zenith angle of the arrival direction of the primary particle determined in units of rad.

**mc.delCore** Difference between the reconstructed core position and the true core position in meters.

**mc.logEnergy** Base ten logarithm of the true primary energy. Here the energy is given in units of GeV.

**sweets.IWgt** In HAWC simulations with CORSIKA, primaries are not generated with a realistic probability distribution of  $E$  and  $r$ , MC events must be re-weighted for this purpose. The SWEETS program compute the weights. The primaries of the simulated events using CORSIKA are drawn from unnatural and unphysical distributions for  $E$  and  $r$ , thus they must be re-weighted in order to model physical fluxes of particles. The sweets.IWgt is a weight to reproduce in simulations an isotropic flux and the nominal mass composition model of HAWC.

## 4.5.8 Gamma/Hadron separation

Almost 99.9% of the events detected by HAWC are cosmic rays, and they represent the major background in the observation of gamma-ray events. Therefore, it is vital to count on with an effective Gamma/Hadron separation method. As mentioned before (see sub-section 4.5.1), gamma ray induced air showers are different from hadronic induced air showers, physically such difference can be seen on the lateral distribution. The lateral distribution of a  $\gamma$ -ray induced air shower is smoother and more compact, while the lateral distribution of a cosmic ray air shower is more bulky and more clumpy.

The HAWC collaboration employs two variables to perform the Gamma/Hadron separation: Compactness ( $\mathcal{C}$ ) and the Parameter for Identifying Nuclear Cosmic-Rays (PINCness,  $\mathcal{P}$ ).

The Compactness is defined as [145]:

$$\mathcal{C} = \frac{N_{hit}}{CxPe40}, \quad (4.10)$$

where  $N_{hit}$  is the number of PMTs activated during the event and  $CxPe40$  is the highest charge measured outside a circle of 40 m from the shower core. As cosmic ray induced air showers are more clumpy far from the shower core region than gamma ray induced air showers (and therefore are more likely to get an isolated large hit), these showers have smaller values of  $\mathcal{C}$ .

On the other hand, the PINCness variable measures how smooth the lateral distribution of an event is and has a  $\chi^2$ -like form [145]:

$$\mathcal{P} = \frac{1}{N} \sum_{i=0}^N \frac{(\log_{10} q_i - \langle \log_{10} q_i \rangle)^2}{\sigma_{\log_{10} q_i}}, \quad (4.11)$$

where  $N$  is the number of total hits per event,  $q_i$  is the measured effective charge at the  $i$ -th PMT, and  $\sigma_{\log_{10} q_i}$  is the corresponding  $q_i$  uncertainty. So, the smoother the lateral distribution of an air shower is, the more likely it is to be a gamma ray induced event, and a smaller value of PINCness.

### 4.5.9 Quality cuts

Some quality cuts were applied to HAWC's experimental and simulated data to diminish the effect of the systematic errors in the shower parameters, such as: energy, arrival direction and core position. The quality cuts applied on this work are listed below:

**rec.zenithAngle** Only vertical events are selected, in particular, the events that have an arrival direction between  $0^\circ$  and  $16.71^\circ$  are taken into account.

**rec.coreFiduScale<100** This cut is mainly applied to diminish the systematical errors in the reconstruction of the energy, core position and arrival direction. This scale was chosen to select events with shower cores inside HAWC's area.

**rec.nChAvail>0** During the reconstruction procedure there are some cases in which the number of available channels is zero. This cut discriminates such events.

**rec.nHit $\geq$ 0.3\*rec.nChAvail** Eliminates low energy events that are below the region of maximum efficiency.

**rec.nHit $\geq$ 75** This cut optimizes the energy reconstruction algorithm (see section 4.5.4).

**rec.angleFitStatus=0** Only the events that have a successful angular fit are selected.

**rec.coreFitStatus=0** Only the events that have a successful core fit are selected.

**rec.CxPE40XnCh $\geq$ 60** First, a circumference of a radius of 40 m is plotted from the center of the detector. This quality cut selects only those events that activated at least 60 channels within the circumference.

**stdCuts.isSelected=1** It removes hits that were tagged as bad and did not satisfy some standard quality criteria for the behaviour of the signal of the PMTs and for the relative time threshold of the trigger.

**event.hit.channelsIsGood=1** It ensures that the PMT used in the reconstruction is good.

In other words, the selected events are verticals,  $\theta < 16.71^\circ$ , activated at least 60 channels in a radius of 40 m from the shower core, fell inside HAWC's area, recorded a signal in at least 75 channels of a total of 1200, and activated at least 30% of the available channels.

## 4.6 Systematic errors

The selected events for this work went through a quality test. The test was carried out through an analysis of the systematic errors of the:

- arrival direction,

- energy,
- and the air showers' core position.

All the MC samples were weighted according to the nominal model, as described at section 4.5.5. Also, the aforementioned quality cuts were applied to the MC samples.

In general, the systematic error, or bias, is defined as the difference between the true and the reconstructed observables, and the resolution is defined as the region that covers the 68% of the bias.

In the following, for the plots in this section, the graph on the left represents the bias, and the graph on the right side represents the resolution. The blue points stand for protons, the red triangles represent the iron nuclei, and the black stars represent the data for all nuclei using the nominal composition model, while the R and T superscripts stand for the reconstructed and true variables, respectively.

### 4.6.1 Angular bias and resolution

The angular bias is defined as the angle between the true and reconstructed shower arrival directions, i. e.:

$$\Delta\alpha = |\vec{\alpha}^T - \vec{\alpha}^R| = \cos^{-1}(\sin\theta_R\sin\theta_T\cos(\phi_T - \phi_R) + \cos\theta_T\cos\theta_R). \quad (4.12)$$

fig. 4.13 shows that the the arrival direction bias generally tends to decrease as the energy tends to grow up. At high energies, the angular resolution is better. However, it is clear that the iron nuclei resolution is slightly worse than the resolution for the hydrogen nuclei, specially at low energies,  $\log_{10}(E/GeV) = [3.5, 4.5]$ , and it maybe due to the fact that the iron signals are less intense in the detectors and have more fluctuations.

At an energy  $E=10^{4.5}$  GeV, the angular bias and resolution for protons are:  $\lesssim 0.3^\circ$  and  $\lesssim 0.4^\circ$ , respectively; and for iron nuclei we have:  $\lesssim 0.3^\circ$  and  $\lesssim 0.4^\circ$ , correspondingly.

### 4.6.2 Energy bias and resolution

The energy systematic error is given by:

$$\Delta E/E = (E^T - E^R)/E^T. \quad (4.13)$$

For both energy bias and resolution, the behaviour for the hydrogen and iron nuclei is better at high energies, as appreciated in fig. 4.14. At low energies, the bias for protons and iron nuclei is bigger than at high energies, most likely due to fluctuations which are larger at low energies. It is also observed that the bias is bigger for iron nuclei than for protons since we are using proton calibrated expressions to get the primary energy.

At an energy of  $E=10^{4.5}$  GeV, the bias and the resolution for the hydrogen nuclei are:  $\lesssim 20\%$  and  $\lesssim 30\%$ , respectively; meanwhile, for the iron nuclei they are  $\lesssim 80\%$ ,  $\lesssim 97\%$ , correspondingly.

### 4.6.3 Core position bias and resolution

The formula used to calculate the systematic error of the shower core position is as follows:

$$\Delta R = \sqrt{(X^T - X^R)^2 + (Y^T - Y^R)^2}, \quad (4.14)$$

where  $X$  and  $Y$  represent the coordinates of the shower core position at ground.

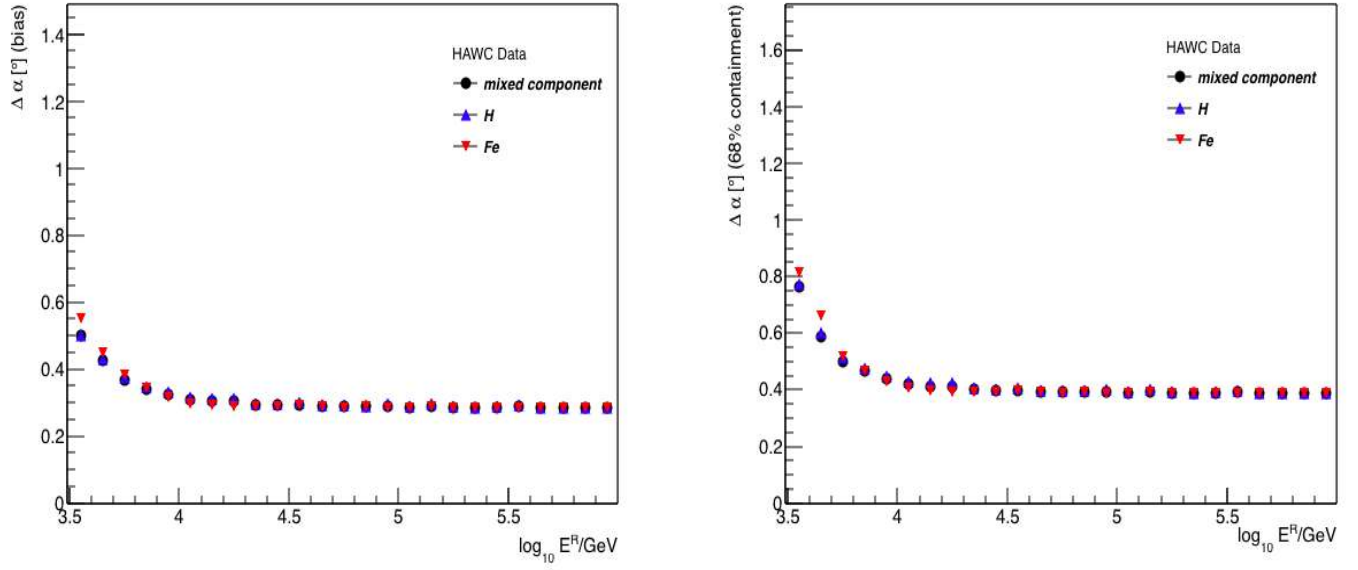


Figure 4.13: Left: The arrival direction bias vs  $\log_{10}E^R$  in *HAWC* for the selected MC data. Right: Angular resolution vs  $\log_{10}E^R$  in *HAWC* for the selected MC data.

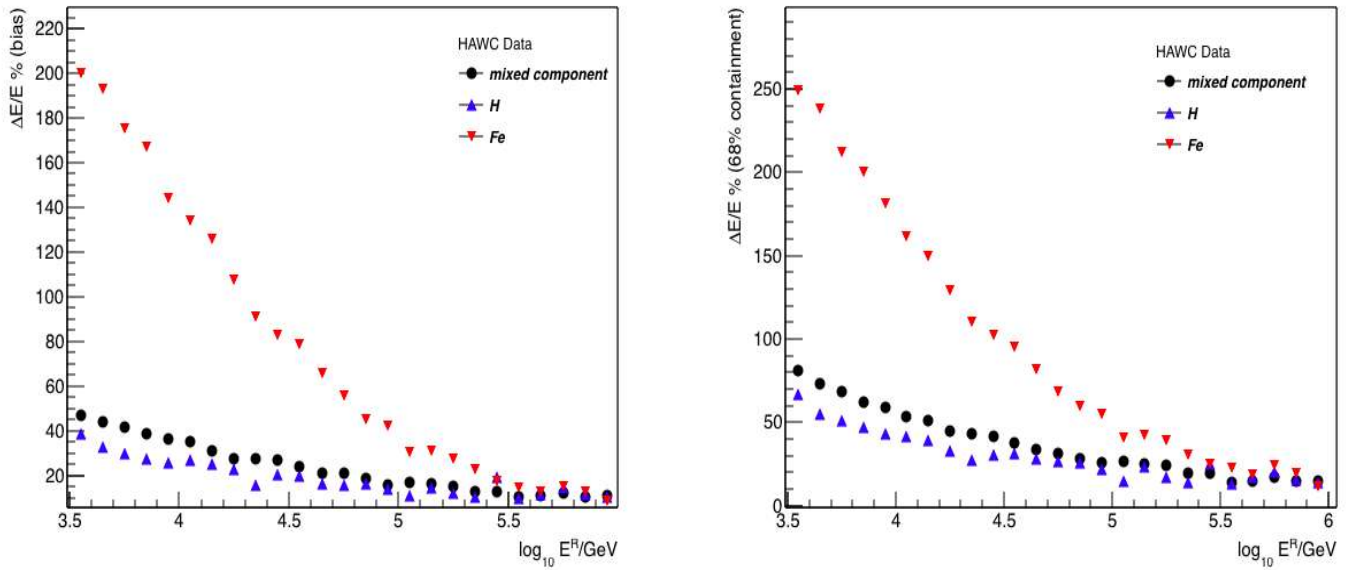


Figure 4.14: Left: Primary energy bias vs  $\log_{10}E^R$  in *HAWC* for the selected MC data. Right: Energy resolution vs  $\log_{10}E^R$  in *HAWC* for the selected MC data.

From fig. 4.15 it can be seen that the bias and the resolution for the shower core position of protons tends to decrease as the energy grows up. In the case of the iron induced air showers, the bias at low energies is bigger than for protons, but both of them decrease at high energies and are almost similar.

At an energy of  $E=10^{4.5}$  GeV, the systematic error and the resolution for the shower core position are:  $\lesssim 7.5$  m and  $\lesssim 10.5$  m, respectively; and for the iron component they are  $\lesssim 8$  m,  $\lesssim 11$  m, correspondingly.

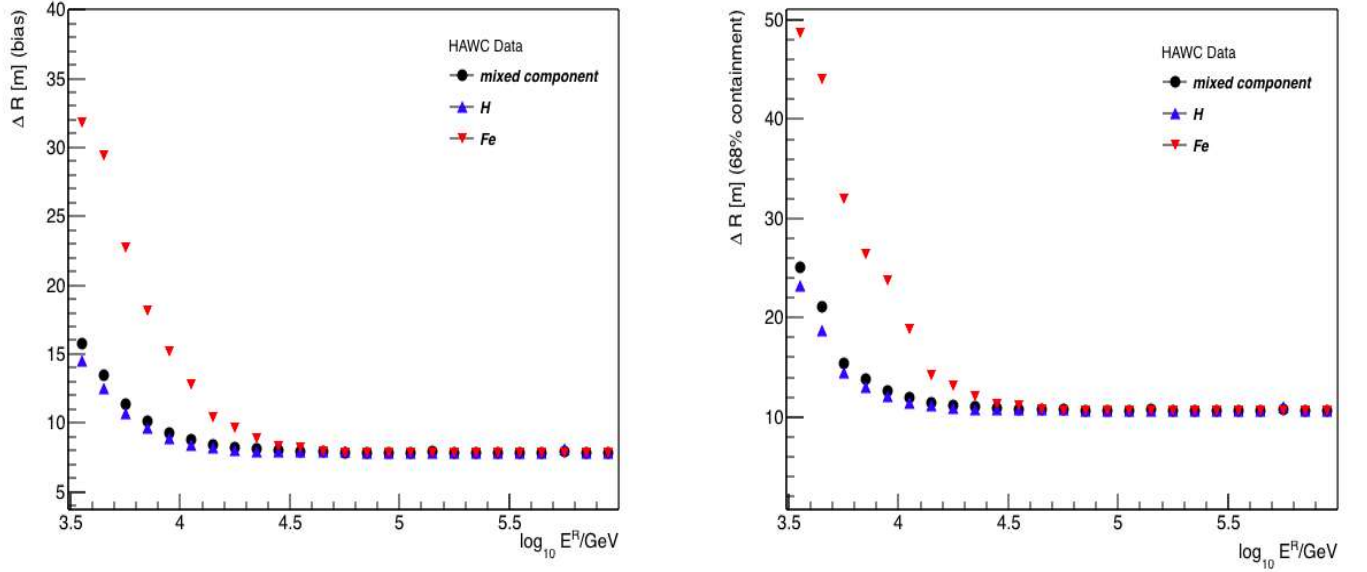


Figure 4.15: Left: Shower core position bias vs  $\log_{10}E^R$  in *HAWC* for the selected MC data. Right: Core resolution vs  $\log_{10}E^R$  in *HAWC* for the selected MC data.

## 4.7 Experimental data

For this work, the employed experimental runs have a total duration of 119,875.148 s (1.38 days) and were recorded by *HAWC* in 2016. Table 4.3 has a basic description of the experimental runs selected for this work <sup>1</sup>.

To diminish the effect of systematic errors in the analysis, the events must fulfill the quality criteria described in chapter 4.5.6. For the present analysis data with primary energy in the interval  $E = 10^{3.5}$  GeV -  $10^{6.2}$  GeV was considered. Before applying the criteria selection of section 4.5.9, the experimental data set had a total of 3,367,914,278 events, and after the cuts the experimental data set has 33,571,855 events, which corresponds to the 1% of the initial events.

<sup>1</sup>For a more detailed description about the experimental runs, please visit: *HAWC* Tranches [168].

Run	Date	Duration	#events before cuts	#events after cuts
run005481	2016/06/02	t=32,168.625 s	795370112	7942997
run005489	2016/06/05	t=21,158.948 s	539856641	5362015
run005490	2016/06/05	t=35,311.425 s	900178843	8929378
run005493	2016/06/07	t=26,147.625 s	655220894	6559812
run005515	2016/06/12	t=19,499.774 s	477287788	4777653

Table 4.3: Experimental runs selected for the study of the lateral distribution of EAS measured at HAWC.

# Chapter 5

## Analysis method of the lateral distribution of cosmic-ray induced showers

The HAWC observatory is well-suited to perform detailed event-by-event studies of the lateral distribution of EAS at TeV energies given its instrumented area, large volume and coverage, closed-packed detector design, high altitude and large number of photomultipliers (PMT).

The interest in the study of the lateral distribution lies in the fact that it contains information about the energy and the mass composition of the primary cosmic rays.

As mentioned in chapter 2, the lateral age parameter,  $s$ , is related to the shape of the lateral distribution of secondaries and the depth of the shower maximum position. In addition, the lateral shower age has a dependence with the mass composition of cosmic rays. At HAWC, the age parameter has been already used in primary cosmic ray mass composition studies [139, 164, 169]. The dependence of the mean lateral age parameter as a function of the energy and the primary mass is shown in fig. 5.1 MC predictions. The measured energy dependence of the age is also shown.

As observed in the above figure, there is a deviation in the behaviour of the measured lateral shower age from the MC predictions at energies higher than  $E = 10^{5.5}$  GeV. The deviation observed on the graph may be due to the fact that the lateral distribution function (LDF) used for the estimation of the lateral age parameter may not be fitting properly the data. This deviation has motivated the purpose of this work, which focuses in the study of the lateral distribution of cosmic ray induced air showers with the aim of:

- Determinate the origin of the deviation of the experimental shower age distribution from the MC predictions (see fig. 5.1) at  $E \geq 10^{5.5}$  GeV.
- Verify if the observed deviation is due to the LDF used in the estimation of the lateral shower age at HAWC.

For the purpose we will find the function that best describes the lateral distribution of EAS created by cosmic rays and detected with HAWC and we will study the impact of the LDF in the observed deviation. In addition we will study the sensitivity of the lateral shower age to the mass composition of cosmic rays by calculation of the figure of merit.

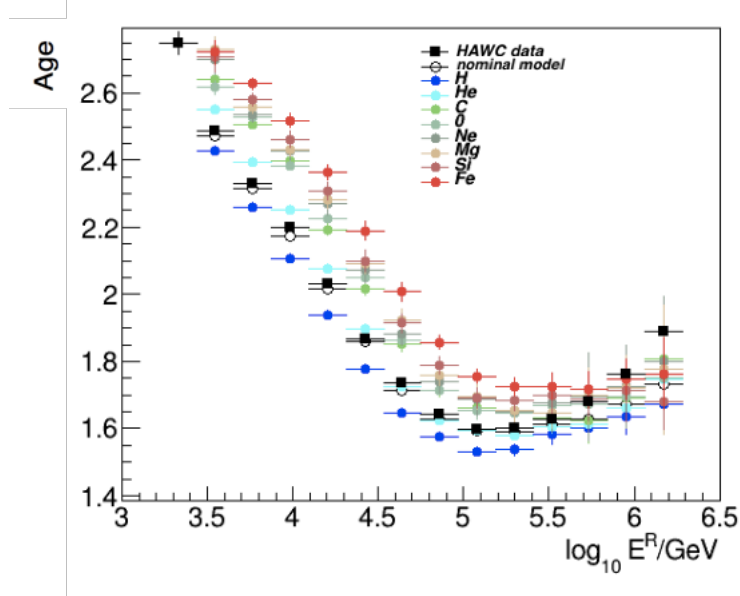


Figure 5.1: Mean lateral age parameter as a function of the energy for eight nominal species (circles) according to MC predictions in comparison with experimental data (squares) for vertical air showers,  $\theta < 16.71^\circ$ .

## 5.1 Reconstruction of the lateral distribution of EAS in HAWC

At HAWC, the lateral distribution of the event is just the lateral effective charge distribution deposited at each PMT as a function of the distance to the shower core position,  $Q_{eff}(r)$ , at the shower front coordinate system. That means that we need to project the coordinates of the PMTs onto the shower front plane to obtain the above mentioned distributions. As a first step the coordinate system of the detector is translated to the core position. This way if the position of the  $i$ th-PMT in the HAWC system is defined as

$$\vec{r}_i = x_i \hat{i} + y_i \hat{j} + z_i \hat{k}, \quad (5.1)$$

and the position of the shower core is

$$\vec{R}_c = x_c \hat{i} + y_c \hat{j} + z_c \hat{k}, \quad (5.2)$$

in the same system, then the position of the  $i$ th-PMT in the new system centered at the EAS core is given by

$$r_{i,H} \vec{r}_i = \vec{r}_i - \vec{R}_c, \quad (5.3)$$

Then, we need to make a projection of the position of the WCDs to the shower front, for this we define a normal vector perpendicular to shower front pointing to the direction from which arrived the cosmic ray (see fig. 5.2). Such vector is defined as:

$$\hat{n} = \sin\theta \cos\phi \hat{i} + \sin\theta \sin\phi \hat{j} + \cos\theta \hat{k}, \quad (5.4)$$

where  $\theta$  and  $\phi$  are the zenith and azimuth angles of the shower axis. Here,  $\phi$  is measured from  $\hat{x}$ , which points to the East.

The perpendicular vector from a PMT to the shower core front is  $\vec{d}_i$  and it is given by

$$\vec{d}_i = -d_i(\hat{n}), \quad (5.5)$$

where

$$d_i = \hat{n} \cdot r_{i,H}, \quad (5.6)$$

Then, by vectorial sum, the lateral position vector from the shower core to a PMT in shower disk coordinates (SDC) is:

$$\vec{r}_{i,SDC} = r_{i,H} + \vec{d}_i, \quad (5.7)$$

and finally, the lateral distance of the PMT to the core on the shower front plane is:

$$r_{i,SDC} = |\vec{r}_{i,SDC}| = \sqrt{x_{i,SDC}^2 + y_{i,SDC}^2 + z_{i,SDC}^2} \quad (5.8)$$

where

$$x_{i,SDC} = x_{i,H} - d_i(\sin\theta\cos\phi), \quad (5.9)$$

$$y_{i,SDC} = y_{i,H} - d_i(\sin\theta\sin\phi), \quad (5.10)$$

$$z_{i,SDC} = z_{i,H} - d_i(\cos\theta), \quad (5.11)$$

which were derived from eqs. (5.5) - (5.7). Fig. 5.2 shows a 2-dimensional sketch of these quantities. Finally, we can perform two rotations to orient the late/early components of the EAS with the  $-x/+x$  regions and the shower axis, along the  $\hat{z}$  direction. For the first case, we make a  $\phi$  rotation around the  $\hat{z}_{SDC}$ -axis of our system, so that the  $xy$  projection of the arrival direction and the new  $\hat{x}_\phi$ -axis match. So we have:

$$\begin{bmatrix} x_\phi \\ y_\phi \\ z_\phi \end{bmatrix} = \begin{bmatrix} \cos\phi & \sin\phi & 0 \\ -\sin\phi & \cos\phi & 0 \\ 0 & 0 & 1 \end{bmatrix} \begin{bmatrix} x_{SDC} \\ y_{SDC} \\ z_{SDC} \end{bmatrix}.$$

from which it is found that:

$$\begin{bmatrix} x_\phi \\ y_\phi \\ z_\phi \end{bmatrix} = \begin{bmatrix} x_{SDC}\cos\phi + y_{SDC}\sin\phi \\ -x_{SDC}\sin\phi + y_{SDC}\cos\phi \\ z_{SDC} \end{bmatrix}. \quad (5.12)$$

Finally, a last rotation of  $\theta$  is performed around the  $\hat{y}_\phi$ -axis, so that the shower axis match with the new  $\hat{z}_\theta$ -axis. Hence,

$$\begin{bmatrix} x_\theta \\ y_\theta \\ z_\theta \end{bmatrix} = \begin{bmatrix} \cos\theta & 0 & \sin\theta \\ 0 & 1 & 0 \\ -\sin\theta & 0 & \cos\theta \end{bmatrix} \begin{bmatrix} x_\phi \\ y_\phi \\ z_\phi \end{bmatrix},$$

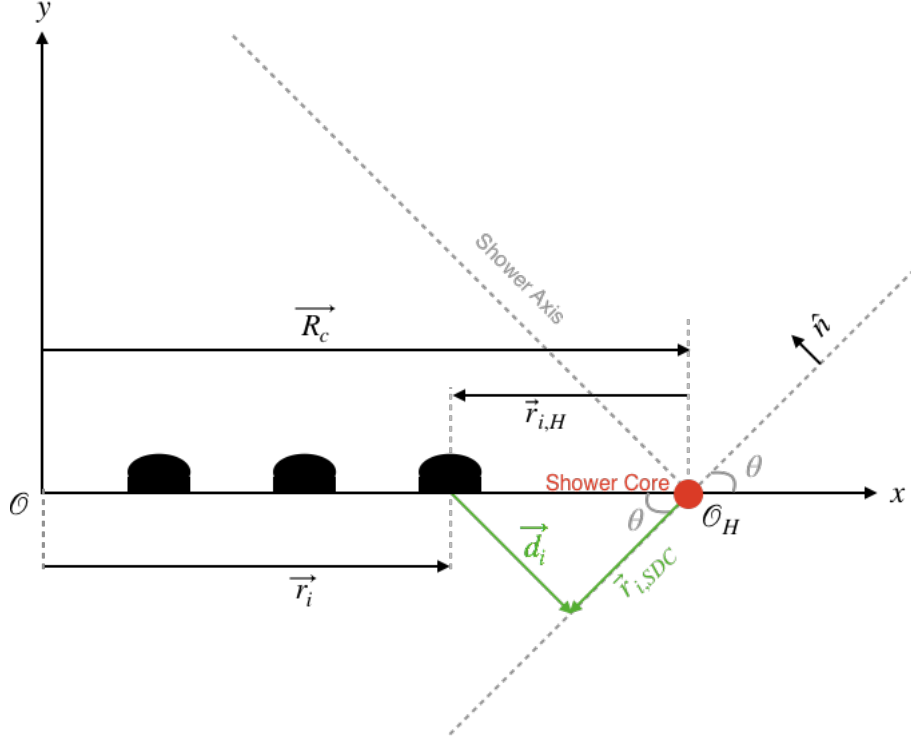


Figure 5.2: Sketch of the relevant quantities for the calculus of the distance to the shower axis at shower disk coordinates.

and solving the above equation, we obtain

$$\begin{bmatrix} x_\theta \\ y_\theta \\ z_\theta \end{bmatrix} = \begin{bmatrix} x_\phi \cos\theta + z_\phi \sin\theta \\ y_\phi \\ -x_\phi \sin\theta + z_\phi \cos\theta \end{bmatrix}. \quad (5.13)$$

Fig. 5.3 shows a lateral distribution of a simulated air shower event in this new coordinate system. The final result is the lateral distribution of effective charge deposited at each PMT,  $Q_{eff}$ , as a function of the distance to the core position (see fig. 5.4 for a MC event sample). The errors of the effective charge are parametrized by using the following empirical function [170]:

$$\log_{10}(Q_{eff}^{error}) = \begin{cases} 0.3 - 0.06667 \log_{10}(Q_{eff}) & \text{if } \log_{10}(Q_{eff}) \leq 3, \\ 0.1 & \text{if } \log_{10}(Q_{eff}) > 3. \end{cases} \quad (5.14)$$

## 5.2 Parameterizing the LDF of cosmic-ray induced extensive air showers

Many collaborations of different experiments have dedicated different analysis to the proper parameterization of the lateral distribution through of cosmic ray induced air showers by comparing the fits of the data with distinct lateral distribution functions.

At HAWC, the lateral distribution of gamma induced EAS is described by the following NKG-type function [158]:

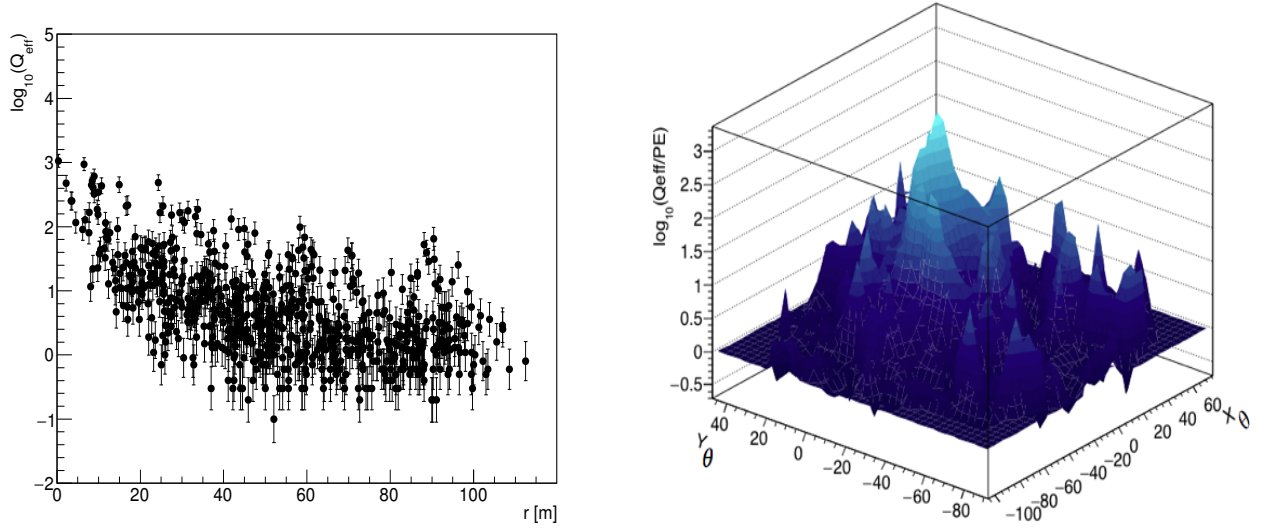


Figure 5.3: Lateral distribution of a proton induced air shower from MC data in 1D (left, where  $r$  is the lateral distance at shower disk coordinates) and 2D (right, in the coordinate system defined in section 5.1). The simulated event has an energy of  $10^{4.5}$  GeV and a zenith angle  $\theta = 8.06^\circ$ .

$$f(r) = A \left( \frac{r}{r_M} \right)^{s-3} \left( 1 + \frac{r}{r_M} \right)^{s-4.5}, \quad (5.15)$$

where  $\rho(r)$  is the charge distribution at a distance  $r$  [m] at shower disk coordinates,  $r_M = 124.21$  m is the Moliere radius,  $A$  is a normalizing factor, and  $s$  is the lateral age parameter. It has been checked that this NKG-like LDF gives a good description of gamma-ray induced air showers [145], but this hasn't been proven yet for cosmic ray induced air showers. Part of this work focuses on determining a LDF that gives an optimal parameterization of the HAWC's data. This and other LDFs chosen from the literature were selected in this study to find a LDF that best describes the lateral distribution of air showers detected at HAWC.

Among the different LDF functions that were tried, it is found the lateral distribution function (5.16) used by the KASCADE collaboration:

$$f(r) = N \cdot \bar{c}(s) \cdot \left( \frac{r}{r_0} \right)^{s-\alpha} \left( 1 + \frac{r}{r_0} \right)^{s-\beta}, \quad (5.16)$$

where  $N$  is the number of particles,  $r_0$  is a scale parameter,  $s$  is the lateral shower age, and

$$\bar{c}(s) = \frac{\Gamma(\beta - s)}{2\pi r_0^2 \Gamma(s - \alpha + 2) \Gamma(\alpha + \beta - 2s - 2)}, \quad (5.17)$$

is a normalization parameter.

For this work, the lateral shower age was left as a free parameter, while  $\alpha = 2.33$  and  $\beta = 1.17$  are constants derived from MC simulations, and in this study  $r_0$  was set to a value of the Moliere radius at HAWC equal to 124.21 m.

The lateral distribution function used by the ARGO collaboration was also selected for this work:

$$f(r) = A \left( \frac{r}{r_0} \right)^{s-2} \left( 1 + \frac{r}{r_0} \right)^{s-4.5}, \quad (5.18)$$

where  $A$  is a normalization factor,  $s$  is the lateral shower age, and  $r_0$  is a constant scale radius. In this study,  $r_0 = 124.21$  m. The  $s$  parameter was left as a free parameter.

Finally, the lateral distribution function called *scaling formalism* used by the AGASA and ARGO collaborations was also selected for this analysis [113, 171]. The LDF *scaling formalism* is

$$f(r) = C \left( \frac{r}{r_0} \right)^{-\alpha} \left( 1 + \frac{r}{r_0} \right)^{-(\beta-\alpha)} \left[ 1 + \frac{r}{10r_0} \right]^\delta, \quad (5.19)$$

where  $C$  is parametrization constant,  $\alpha$ ,  $\beta$  and  $\delta$  are fixed parameters, while  $r_0$  is a scale radius again. Since the *scaling formalism* didn't describe properly the selected data for this work, a modified version of eq. (5.19) was employed instead

$$f(r) = C \left( \frac{r}{r_M} \right)^{-s} \left( 1 + \frac{r}{r_M} \right)^{(s-\beta)} \left[ 1 + \left( \frac{r}{r_M} \right)^\phi \right]^\delta, \quad (5.20)$$

where  $\beta = 3.59$ ,  $\phi = 0.19$  and  $\delta = 3.61$  were derived from MC simulations and  $r_M = 124.21$  m is the Moliere radius. In the following, eq. (5.20) will be given the name of *modified scaling formalism*.

On the other hand, there were other lateral distribution functions that were tested but it was found that they didn't describe the lateral distribution of cosmic-ray induced air showers measured with HAWC. The following LDFs were ruled out from the analysis:

◇ The Haverá Park lateral distribution function [172]

$$f(r) = K r^{-(\eta + \frac{r}{4000})}, \quad (5.21)$$

where  $K$  is a normalization constant,  $r$  is the lateral distance to the shower core and  $\eta$  was left as a free parameter.

◇ The Egorov lateral distribution function

$$f(r) = \frac{N}{r_M^2} \left( \frac{\eta - 2}{2\pi} \right) \left( \frac{r}{r_M} \right)^{-1} \left( 1 + \frac{r}{r_M} \right)^{-\eta}, \quad (5.22)$$

where  $r_M$  is the Moliere radius,  $N$  is a normalization constant, and  $\eta$  was left as a free parameter.

◇ The Kaneko lateral distribution function

$$f(r) = \frac{CN}{2\pi r_M^2} \left( \frac{r}{r_M} \right)^{s-2} \left( 1 + \frac{r}{r_M} \right)^{s-4.5} \left[ 1 + C \left( \frac{r}{r_M} \right)^2 \right], \quad (5.23)$$

where  $r$  is the lateral distance to the shower core,  $r_M$  is the Moliere radius,  $C$  is a normalization constant, and  $s$  is the lateral shower age which was left as a free parameter.

## 5.3 Description of the Analysis

### 5.3.1 Fit of the lateral distribution of air showers

To fit the experimental data the LDFs (5.15), (5.16), (5.18) and (5.20) were employed using the  $\chi^2$  method to verify the quality of the fits.

As a first step an average over the values of the effective charged deposited at each PMT,  $\bar{Q}_{eff}$ , is obtained for several radial bins,  $r$  (see fig. 5.4 - left), and then different fits are applied over the

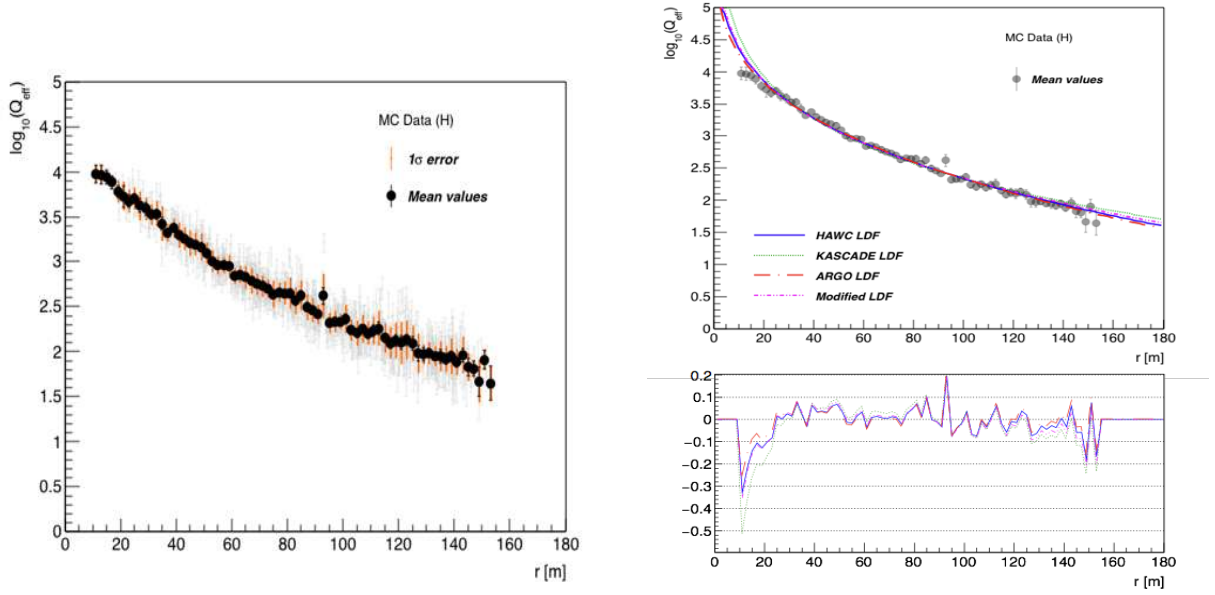


Figure 5.4: Left panel: lateral distribution of a proton induced air shower from the MC data set with an energy of  $E = 10^6$  GeV and a zenith angle of  $15.57^\circ$ . The gray markers correspond to the effective charge points per PMT. Their corresponding errors were calculated using Eq (5.14), the solid black circles correspond to the mean  $Q_{eff}$  per radial bin and the black and grey error bars represent the sum in quadrature of error on the mean plus the experimental error and the one sigma error. Upper right panel: result of the fits to the mean  $Q_{eff}$  of the MC event on the left. Lower right figure: The difference between the observed values and the values from the fit. The  $\chi^2/NDOF$  values for the fitted results are: HAWC LDF = 1.08, KASCADE = 2.2, ARGO LDF = 0.8, Modified LDF = 1.3.

$\bar{Q}_{eff}$  distribution using the  $\chi^2$  method (see fig. 5.4 - right). To fit  $Q_{eff}(r)$  with the above LDFs the minimum  $\chi^2$  method was used. For that, the observed distribution is compared against an expected distribution of the same data as follows:

$$\chi^2 = \sum_{i=1}^n \left( \frac{\bar{Q}_{eff,i} - f(r_i)}{\sigma_i} \right)^2, \quad (5.24)$$

where  $n$  is the number of radial bins,  $\bar{Q}_{eff,i}$  is the mean measured value of the deposited charge per radial bin,  $r_i$ ,  $f(r_i)$  is the predicted mean value of effective charge and  $\sigma_i$  is the uncertainty of the data value, which is the sum in quadrature of the error on the mean and the experimental error.

To obtain the LDF that best fits the data, a systematic study was carried out through a comparison of the  $\chi^2$  per number of degrees of freedom (NDOF) of the results of the fits. The results for the MC predictions in the energy range between  $10^{3.5}$  GeV to  $10^{6.2}$  GeV for hydrogen and iron nuclei are shown in fig. 5.5, from which it can be seen that at energies lower than  $E \sim 10^{4.4}$  GeV the eqs. (5.15) and (5.16) give a better description of the MC data, but for energies higher than  $E \sim 10^{4.4}$  GeV, eqs. (5.15) and (5.20) fit better the data.

The average  $s$  obtained with the selected LDFs for the MC simulations is shown at fig. 5.6 for protons and iron nuclei. The sensitivity of the lateral age parameter to the mass composition of cosmic rays was studied with the results from the fits of the selected LDFs and are presented in the

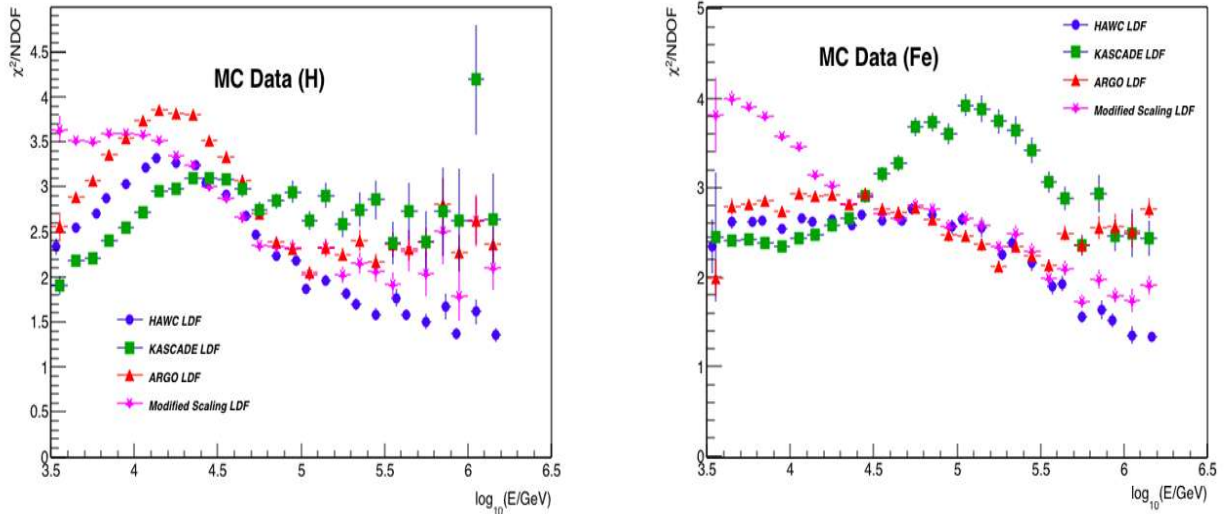


Figure 5.5: Comparisons of the mean  $\chi^2/NDOF$  as a function of the reconstructed energy of the resulting fits with each of the selected LDFs for the hydrogen (left panel) and iron (right panel) MC events.

following section.

### 5.3.2 Predicted lateral age parameter

The average  $s$  obtained with the LDFs (5.15), (5.16), (5.19) and (5.20) for protons and iron nuclei from the MC simulations is shown at fig. 5.7 as a function of the energy. The error bars represent the one sigma error. It can be seen that the age parameter has a dependence with the mass composition and the energy. From figs. 5.7, upper and right lower panels, as the energy tends to grow up, the values of the age parameter tend to decrease, i.e., at higher energies the measured air showers become younger, and the values of the age parameter depend on the mass composition, the heavier nuclei produced older showers than the lighter nuclei. At energies higher than  $10^5$  GeV the lateral shower age doesn't decrease because the air shower is not completely contained by the detector. On the other hand, from fig. 5.7, left lower panel, the  $s$  parameter for the LDF (5.20) behaves different (it increases with energy and with lighter mass groups) as it no longer acts as the traditional lateral shower age by its new definition, but it is observed that this  $s$  parameter is also sensitive to the mass composition of cosmic rays. The sensitivity of the age parameter to the mass composition of the primaries is evaluated with the figure of merit (FOM). The FOM quantifies the separation between the mean values of the classes to analyze [173, 174], in this case, the separation of proton and iron showers by the shower age value. The FOM is defined as:

$$FOM = \frac{|s_{Fe} - s_p|}{\sqrt{\sigma_p^2 + \sigma_{Fe}^2}}, \quad (5.25)$$

where  $s_p$  and  $s_{Fe}$  are the mean values of the proton and iron populations, respectively, and  $\sigma_p$  and  $\sigma_{Fe}$  are the one standard deviation of the proton and iron classes. The FOM defines a relation between the mean value and the standard deviation of the observable for the two populations thus, for example, if the  $FOM = 1$  it indicates that the means of the two populations are separated by

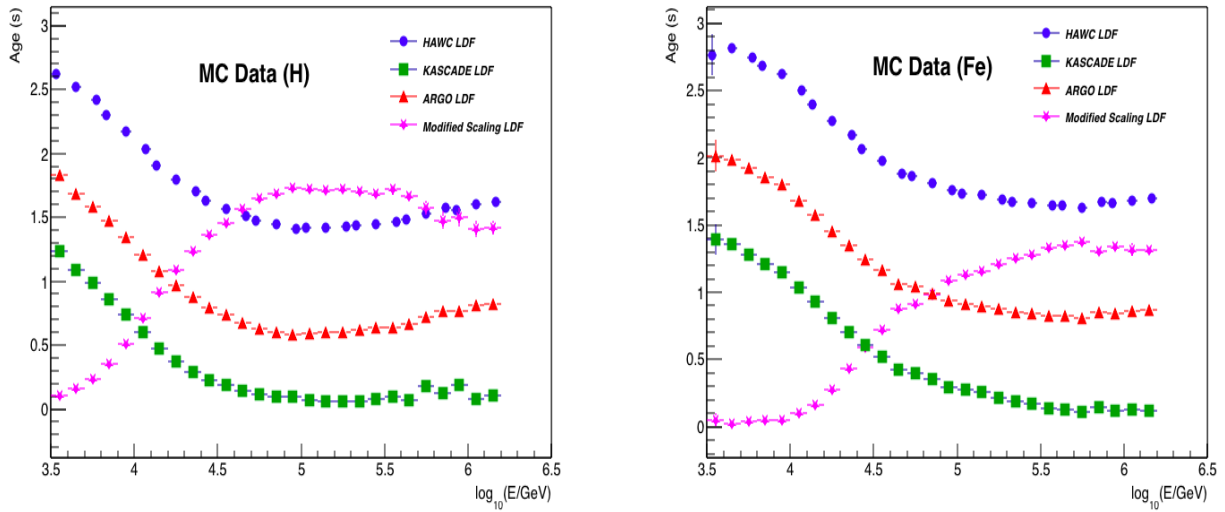


Figure 5.6: Average lateral shower age as a function of the reconstructed energy obtained from the results of the fits with HAWC LDF (blue circles), KASCADE LDF (green squares), ARGO LDF (red triangles) and Modified Scaling Formalism LDF (pink stars) for the hydrogen (left panel) and iron (right panel) MC events.

one standard deviation. The FOM for the age MC distributions shown in fig. 5.7 are shown on the plot of fig. 5.8.

The results of the analysis of the lateral distribution of EAS from cosmic ray primaries measured with HAWC and the discussion of the results for the FOM are described in the following chapter.

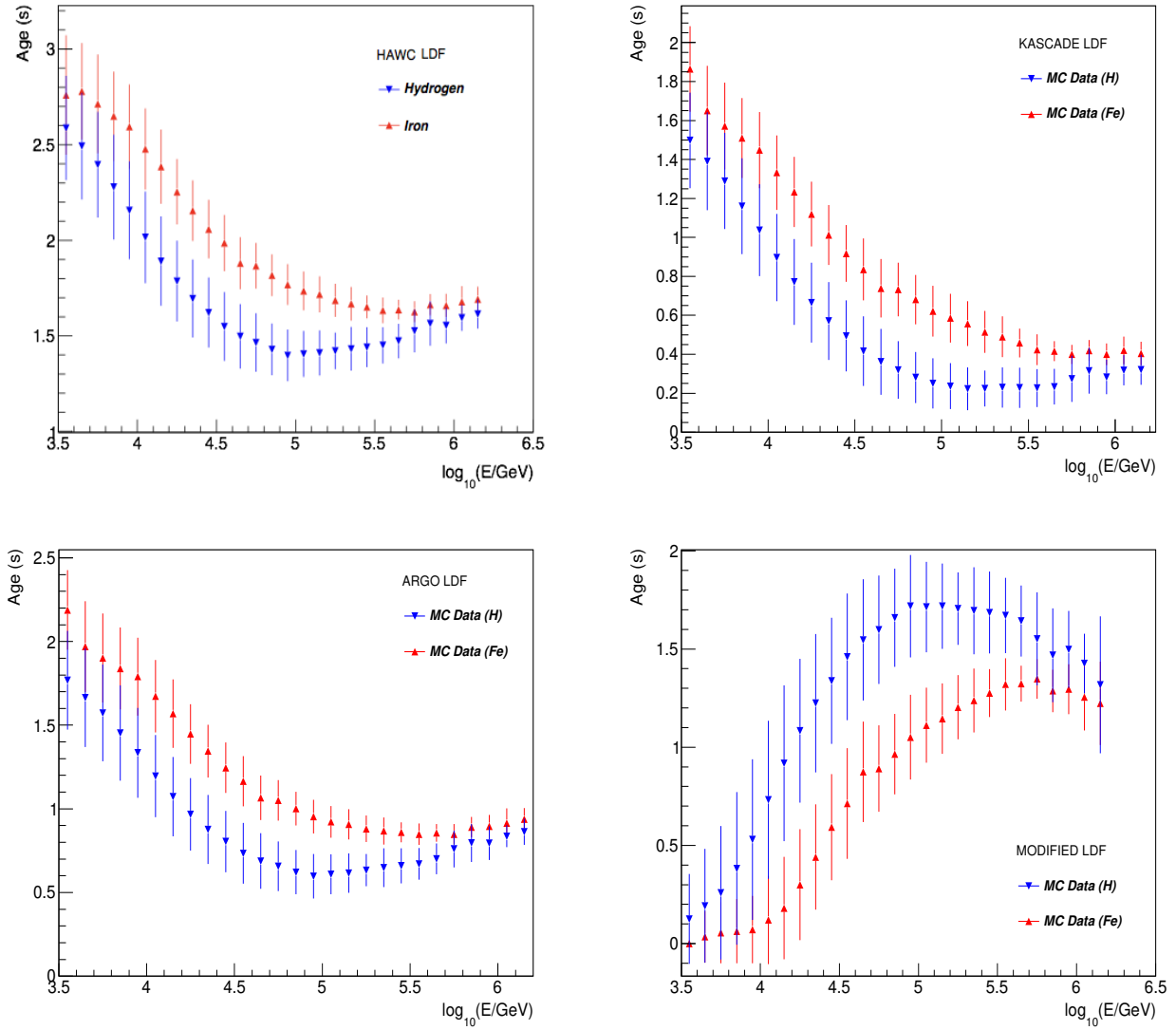


Figure 5.7: Mean lateral shower age estimated by the fits with the formulas HAWC LDF (top left), KASCADE LDF (top right), ARGO LDF (bottom left) and MODIFIED LDF (bottom right) to the lateral distribution of hydrogen (blue face-down triangles) and iron (red triangles) primaries as a function of the reconstructed energy for MC simulations. The error bars correspond to a  $1\sigma$  statistical error.

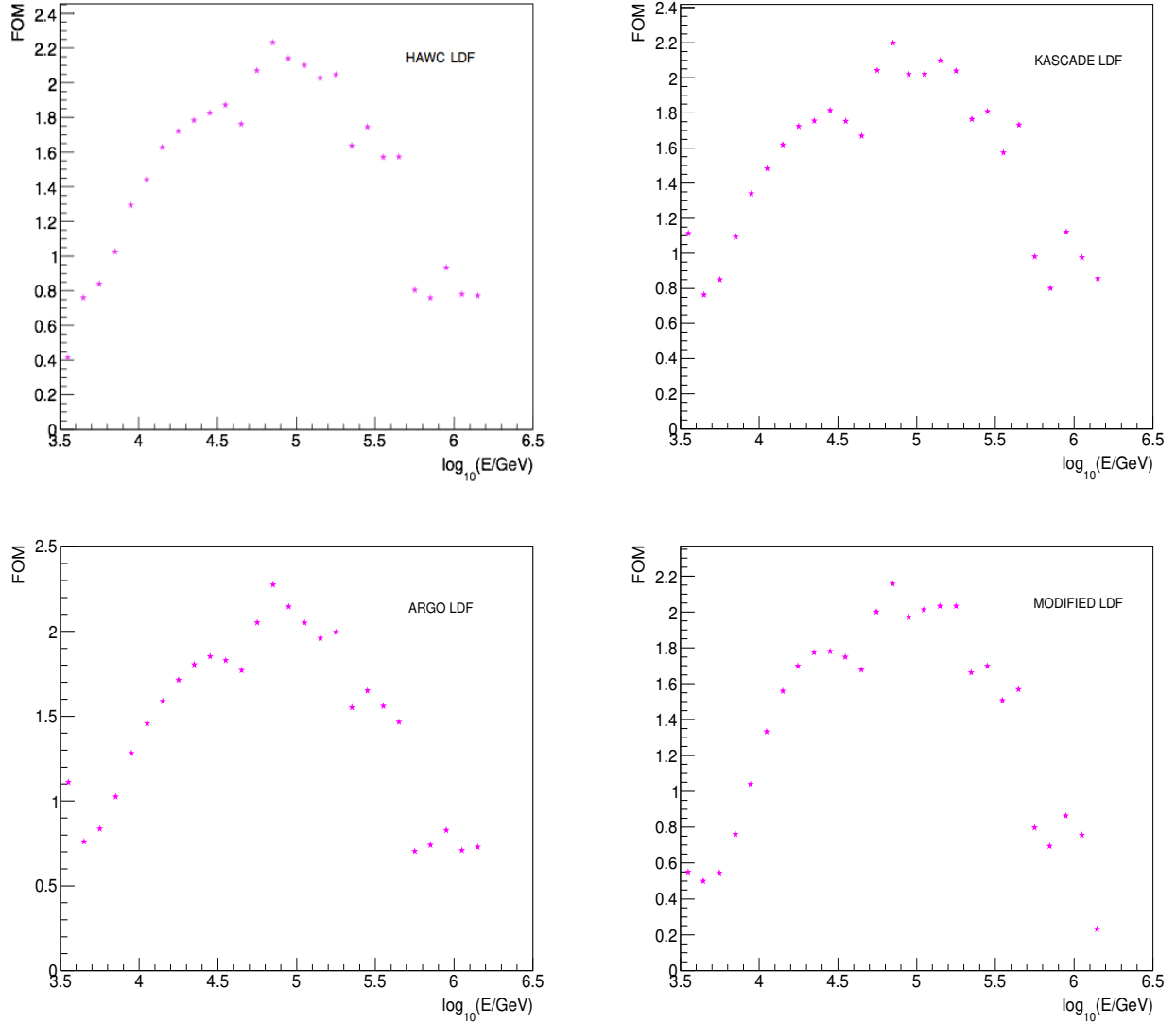


Figure 5.8: Figure of merit as a function of the reconstructed energy for the lateral shower age of proton and iron nuclei according to the MC simulations estimated from the different fits with the LDF's selected for this study, i. e., eqs. (5.15) (top left), (5.16) (top right), (5.19) (bottom left) and (5.20) (bottom right).

# Chapter 6

## Experimental analyses, results and discussion

In this chapter the analysis described in chapter 5 will be applied to HAWC's experimental data to determine the optimal parametrization of the lateral distribution of EAS from cosmic ray primaries measured at HAWC. From here, the lateral shower age parameter will be obtained. Also, the sensitivity of the shower age to the cosmic ray mass composition will be analyzed using MC simulations.

### 6.1 Study of the shape of the lateral distribution of EAS measured at HAWC

For this first analysis of the data, the average lateral distribution of effective charge deposited at each PMT per radial bin,  $\bar{Q}_{eff}(r)$ , for each measured event was calculated. Then the  $\chi^2$  method is applied to fit the  $\bar{Q}_{eff}(r)$  of the event using eqs. (5.15), (5.16), (5.18) and (5.20) to determine which of the LDFs gives a better parameterization of the data. As examples, the  $Q_{eff}(r)$  and  $\bar{Q}_{eff}(r)$  distributions for different experimental events with energies  $E(\text{GeV}) = 10^{3.85}, 10^{4.5}, 10^{5.05}, 10^{5.55}$  and  $10^{6.05}$  are shown in figures 6.1 - 6.3 left (top and bottom). The  $\bar{Q}_{eff}(r)$  distributions are shown along with their  $1\sigma$  errors (thin black error bars) and the sum in quadrature of the errors on the mean and the average experimental error (bold black errors).

The comparison of the mean  $\chi^2/NDOF$  obtained from the fits are shown in fig. 6.4 for measured data. On the other hand, the fits of the example HAWC events are presented in figs. 6.1 - 6.3, right (top and bottom).

Finally, to appreciate the quality of the fit at different radial distances we present the corresponding deviation between the measured and fitted  $\bar{Q}_{eff}(r)$  values against the lateral distance to the core in figs. 6.1 - 6.3 too.

### 6.2 Analysis of the age of air showers and primary composition

The mean lateral age parameter estimated from the fits of the measured data using each of the selected LDFs as a function of the reconstructed energy is shown in Figure 6.5 (left). This calculation was performed to study the energy evolution of the above parameter and compare it with the predictions of the model. In this regard, the average  $s$  obtained with the HAWC LDF for the

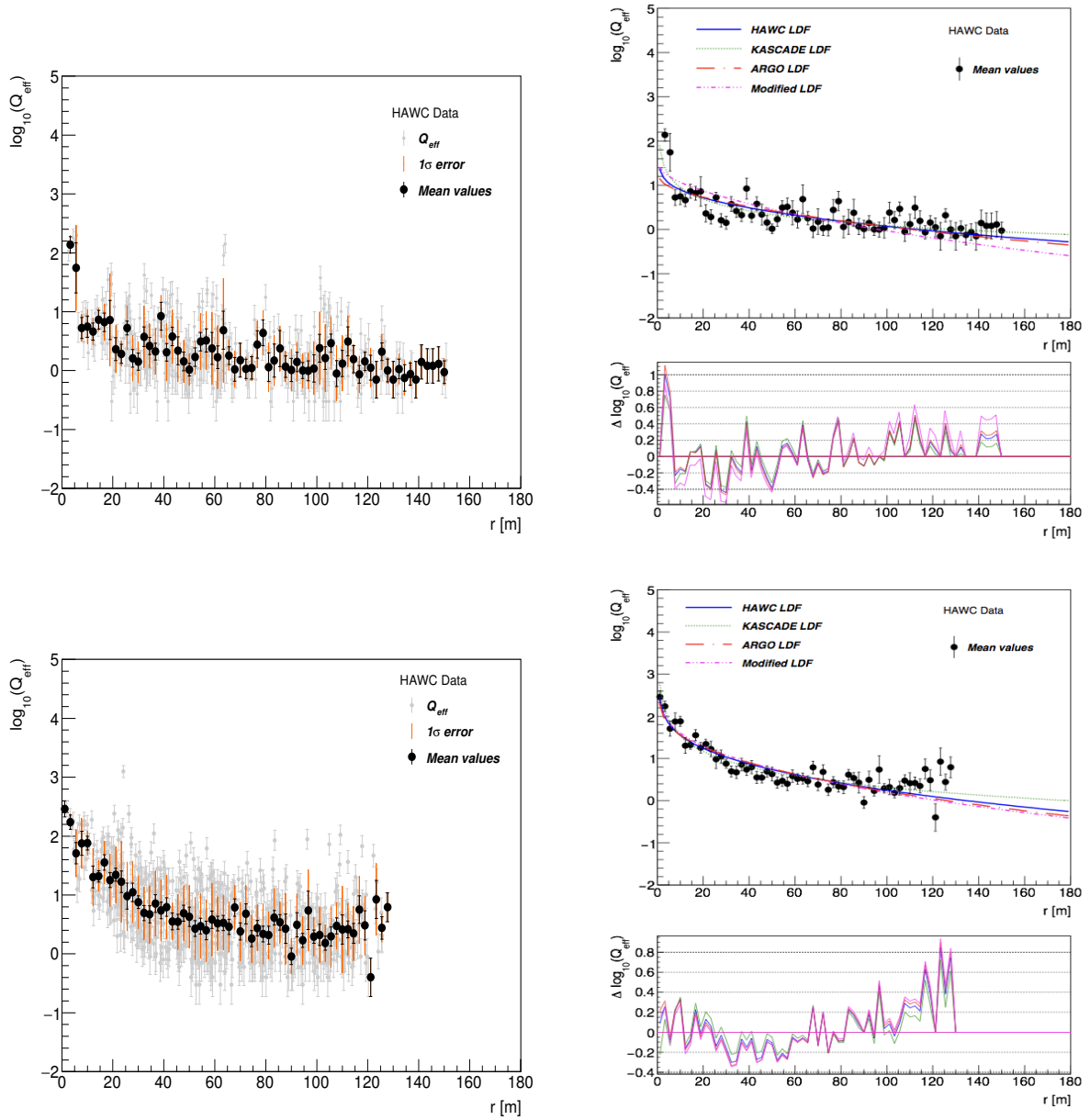


Figure 6.1: Left panels: lateral distributions of two measured air showers. The left top panel corresponds to an event with an energy of  $E = 10^{3.85}$  GeV and a zenith angle of  $7^\circ$ , while the left bottom panel shows an event with an energy of  $E = 10^{4.15}$  GeV and a zenith angle of  $9.7^\circ$ . The gray markers correspond to the effective charge per PMT and their error bars (in gray) are the systematic uncertainties calculated using eq. (5.14). The solid black circles represent the mean  $\bar{Q}_{eff}(r)$  per radial bin. The black error bars correspond to the sum in quadrature of the error on the mean and the experimental error, and the orange error bars represent the  $1\sigma$  error. Right panels: results of the fits to the mean  $\bar{Q}_{eff}$  and the difference  $\Delta \log_{10}(\bar{Q}_{eff}) = \log_{10}(\bar{Q}_{eff}^{exp}) - \log_{10}(\bar{Q}_{eff}^{fit})$  between the observed values and the values from the fit. The  $\chi^2/NDOF$  values of the results from the fits for the top right panel are: HAWC LDF = 2.34, KASCADE = 1.74, ARGO LDF = 2.68, Modified LDF = 3.42; while the corresponding  $\chi^2/NDOF$  values for the event in the bottom panel are: HAWC LDF = 2.13, KASCADE = 1.67, ARGO LDF = 2.5, Modified LDF = 2.56. In these cases, eq. (5.16) gives a better description of the lateral distribution of measured EAS according to the  $\chi^2/NDOF$  analysis.

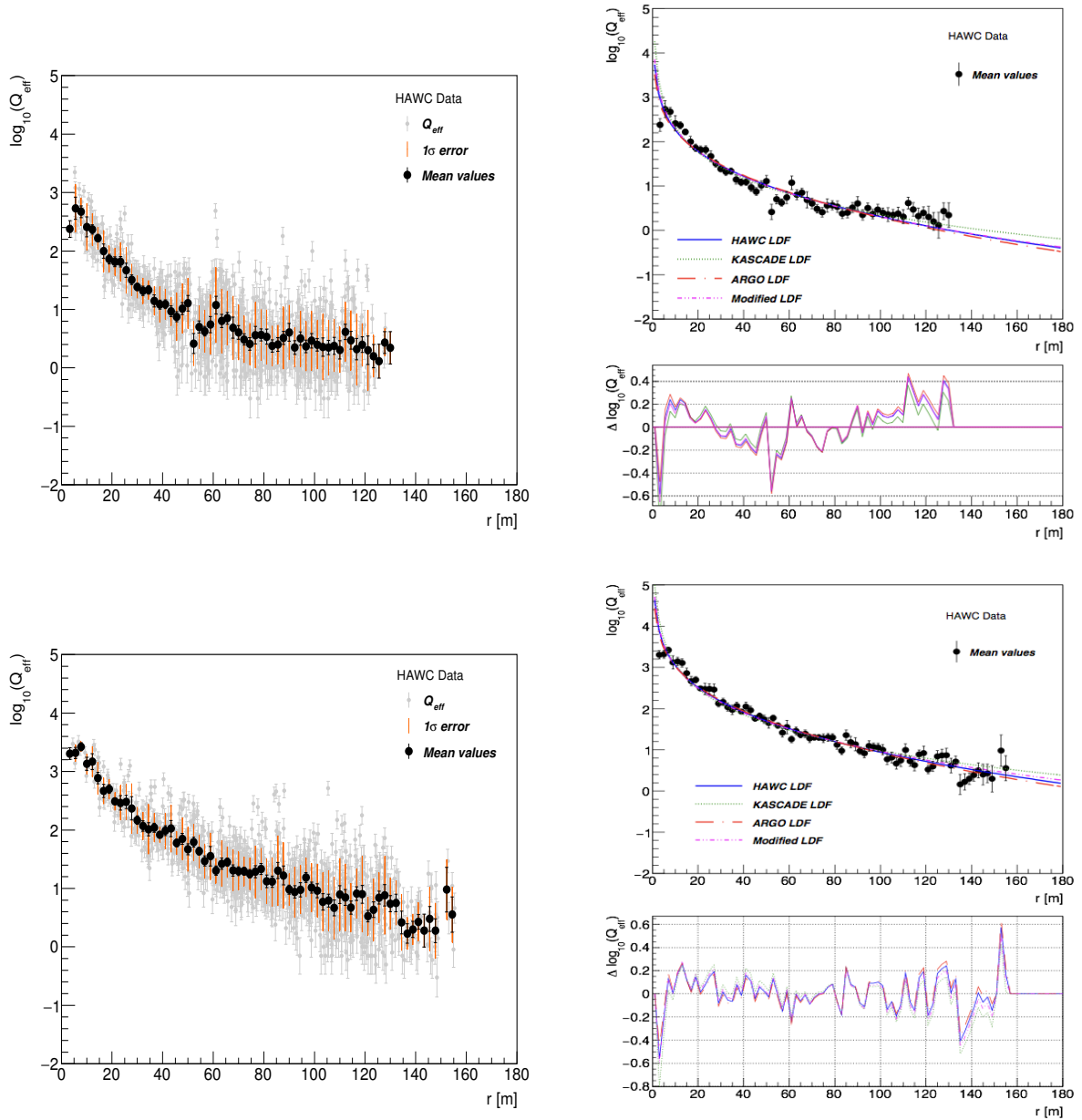


Figure 6.2: Left panels: lateral distributions of two measured air showers. The left top panel corresponds to an event with an energy of  $E = 10^{4.5}$  GeV and a zenith angle of  $9.7^\circ$ , while the left bottom panel shows an event with an energy of  $E = 10^{5.05}$  GeV and a zenith angle of  $10.3^\circ$ . The gray markers correspond to the effective charge per PMT and their error bars (in gray) are the systematic uncertainties calculated using eq. (5.14). The solid black circles represent the mean  $\bar{Q}_{eff}(r)$  per radial bin. The black error bars correspond to the sum in quadrature of the error on the mean and the experimental error, and the orange error bars represent the  $1\sigma$  error. Right panels: results of the fits to the mean  $\bar{Q}_{eff}$  and the difference  $\Delta \log_{10}(\bar{Q}_{eff}) = \log_{10}(\bar{Q}_{eff}^{exp}) - \log_{10}(\bar{Q}_{eff}^{fit})$  between the observed values and the values from the fit. The  $\chi^2/NDOF$  values of the results from the fits for the top right panel are: HAWC LDF = 2.64, KASCADE = 2.3, ARGO LDF = 2.9, Modified LDF = 2.5; while the corresponding  $\chi^2/NDOF$  values for the event in the bottom panel are: HAWC LDF = 1.6, KASCADE = 2.3, ARGO LDF = 1.5, Modified LDF = 1.76.

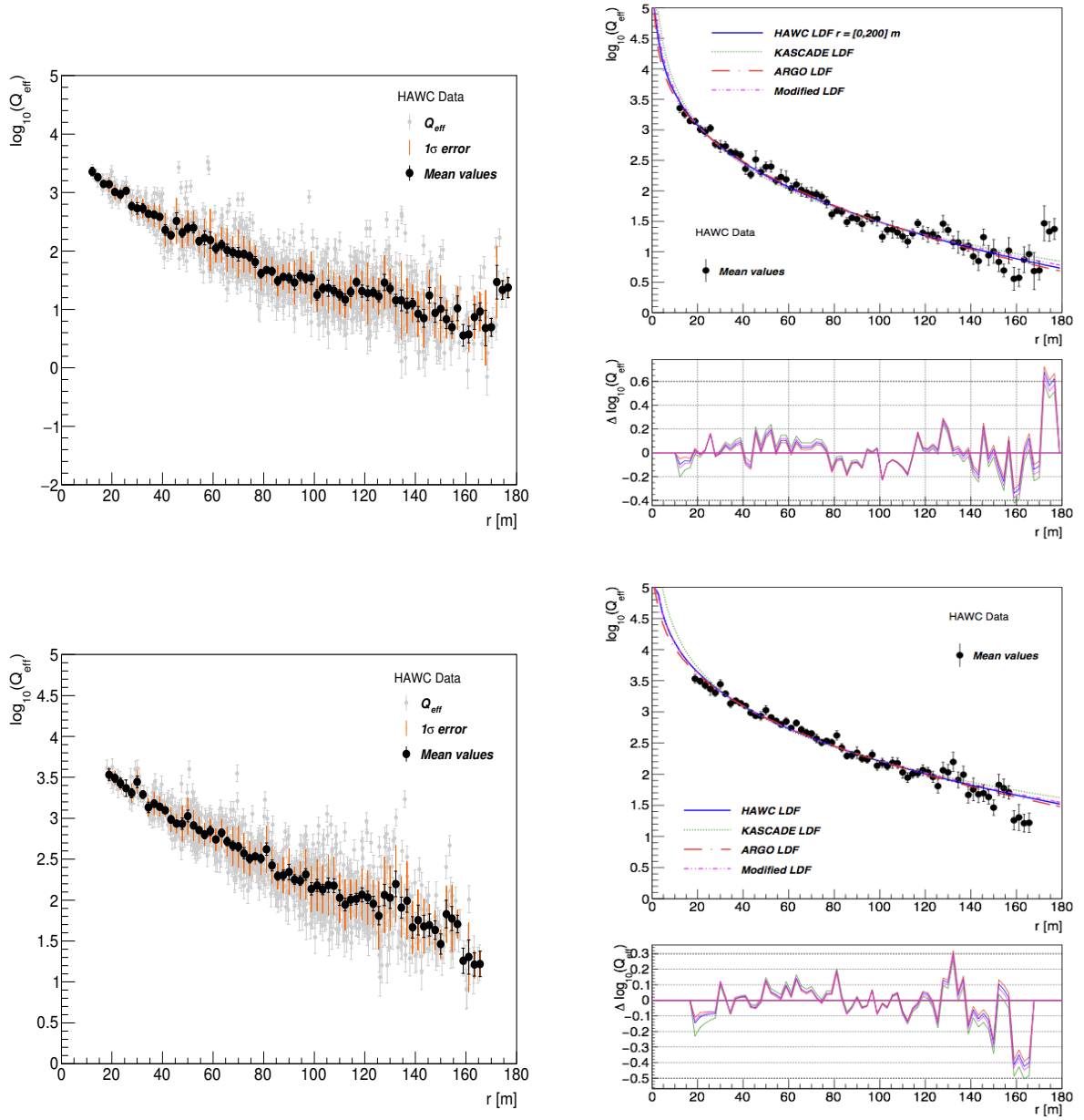


Figure 6.3: Left panels: lateral distributions of two measured air showers. The left top panel corresponds to an event with an energy of  $E = 10^{5.55}$  GeV and a zenith angle of  $12.3^\circ$ , while the left bottom panel shows an event with an energy of  $E = 10^{6.05}$  GeV and a zenith angle of  $14.7^\circ$ . The gray markers correspond to the effective charge per PMT and their error bars (in gray) are the systematic uncertainties calculated using eq. (5.14). The solid black circles represent the mean  $\bar{Q}_{eff}(r)$  per radial bin. The black error bars correspond to the sum in quadrature of the error on the mean and the experimental error, and the orange error bars represent the  $1\sigma$  error. Right panels: results of the fits to the mean  $\bar{Q}_{eff}$  and the difference  $\Delta \log_{10}(\bar{Q}_{eff}) = \log_{10}(\bar{Q}_{eff}^{exp}) - \log_{10}(\bar{Q}_{eff}^{fit})$  between the observed values and the values from the fit. The  $\chi^2/NDOF$  values of the results from the fits for the top right panel are: HAWC LDF = 1.89, KASCADE = 2.23, ARGO LDF = 1.89, Modified LDF = 1.96; while the corresponding  $\chi^2/NDOF$  values for the event in the bottom panel are: HAWC LDF = 1.69, KASCADE = 2.5, ARGO LDF = 1.45, Modified LDF = 1.76.

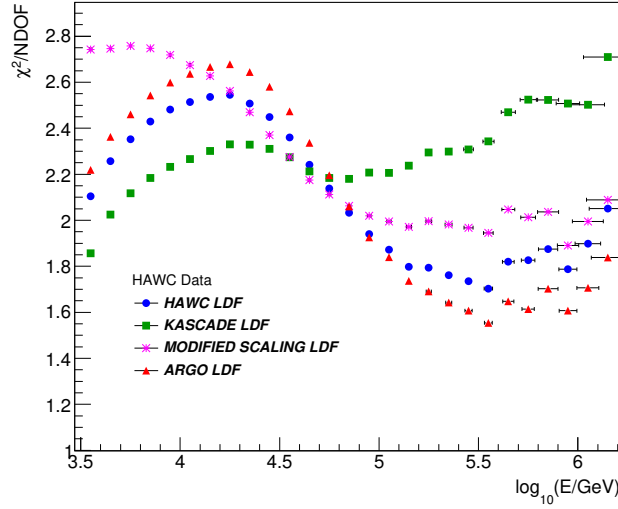


Figure 6.4: Comparison of the mean  $\chi^2/NDOF$  against the reconstructed energy resulting from fits of the HAWC data using the selected LDFs (5.15) (circles), (5.16) (squares), (5.18) (triangles) and (5.20) (stars) in the energy range from  $E = 10^{3.5}$  GeV to  $10^{6.2}$  GeV.

experimental data were compared with the predictions of the MC models for protons and iron nuclei in fig. 6.6.

### 6.3 PINCness

In the search for different parameters of the EAS sensible to the mass composition of cosmic rays, the mean Parameter for Identifying Nuclear Cosmic-Rays, or PINCness (see section 4.5.8), was estimated for each measured and simulated event as a function of the reconstructed energy and also as a function of the lateral distance to the shower core. The corresponding graphics are shown in the right panel of fig. 6.7 and in figs. 6.8 (for different energy intervals).

### 6.4 Comparison of LDF data with model predictions

In addition to the mass composition studies, tests of the predictions of the QGSJET-II-03 high-energy hadronic interaction model were performed using the  $\bar{Q}_{eff}(r)$  data. The test consisted in a comparison among the measured  $\bar{Q}_{eff}(r)$  distributions with the expectations from the above hadronic interaction model for proton and iron nuclei as the more representative elements for the light and heavy mass groups of cosmic rays. The comparisons were performed for the following primary energy intervals:  $\log_{10}(E/GeV) = [3.5,4.0], [4.0,4.5], [4.5,5.0], [5.0,5.5], [5.5,6.0], [6.0,6.5]$ . The results are shown in figs. 6.9.

From figs. 6.9 a deviation in the behaviour of the experimental data from the MC predictions close to the shower core and above  $\bar{Q}_{eff}(r) = 3$  PE for high energies is observed. This change in the behaviour of the lateral distribution of measured EAS seems to be a systematic and may have an influence in the corresponding calculation of the lateral shower age.

To study the effect of the observed deviation near the shower core region on the estimation of the age parameter, the analysis of the lateral distribution was repeated, this time by ruling out the

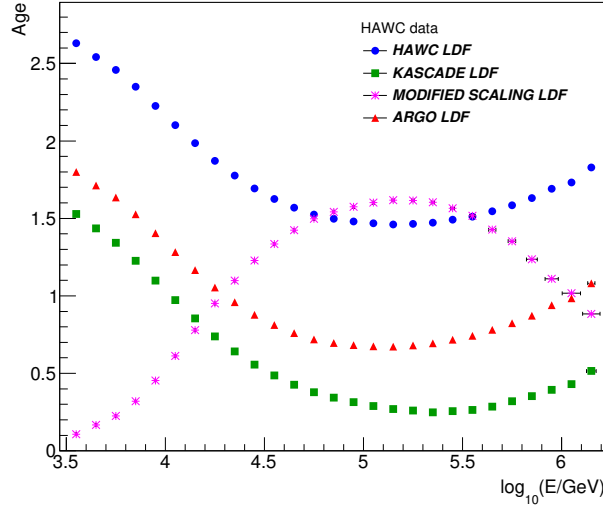


Figure 6.5: Mean lateral shower age estimated from the fits of the selected LDFs over HAWC’s experimental data in the energy range between  $E = 10^{3.5}$  and  $10^{6.2}$  GeV.

$\bar{Q}_{eff}(r)$  values close to the shower core. Depending on the energy interval a corresponding radial cut was applied. For this part of the analysis, the energy intervals described above were used. The radial cuts were chosen according to the results shown in fig. 6.9 for the shower core regions in which the deviation was more dominant. The selected radial cuts are shown in table 6.1).

Energy interval	Radial cut [m]
$\log_{10}(E/GeV) = [3.5,4.0]$	$r > 0$
$\log_{10}(E/GeV) = [4.0,4.5]$	$r > 0$
$\log_{10}(E/GeV) = [4.5,5.0]$	$r > 5$
$\log_{10}(E/GeV) = [5.0,5.5]$	$r > 12.5$
$\log_{10}(E/GeV) = [5.5,6.0]$	$r > 22.5$
$\log_{10}(E/GeV) = [6.0,6.5]$	$r > 27.5$

Table 6.1: Radial cuts corresponding to the corresponding energy intervals selected to study the sensitivity of the age parameter to the data of the lateral distribution near the shower core.

The fit of the data using the LDF (5.15) was repeated but with the radial cuts mentioned before. The results of the fit in different radial regions for some measured EAS are illustrated in fig. 6.10 and are compared with the results of the fit without the radial cuts.

The observed deviation near the shower core may also be originated from a saturation effect of the effective charge deposited at each PMT for values above  $\log_{10}(Q_{eff}) = 3$  Photo Electrons (PE). To study the influence of this possible saturation effect in the estimation of the lateral shower age, a cut was applied over the values of the deposited charge and then the analysis of the shower age was repeated. Only data with  $\log_{10}(Q_{eff}) < 3$  PE were taken into account for the fit and the

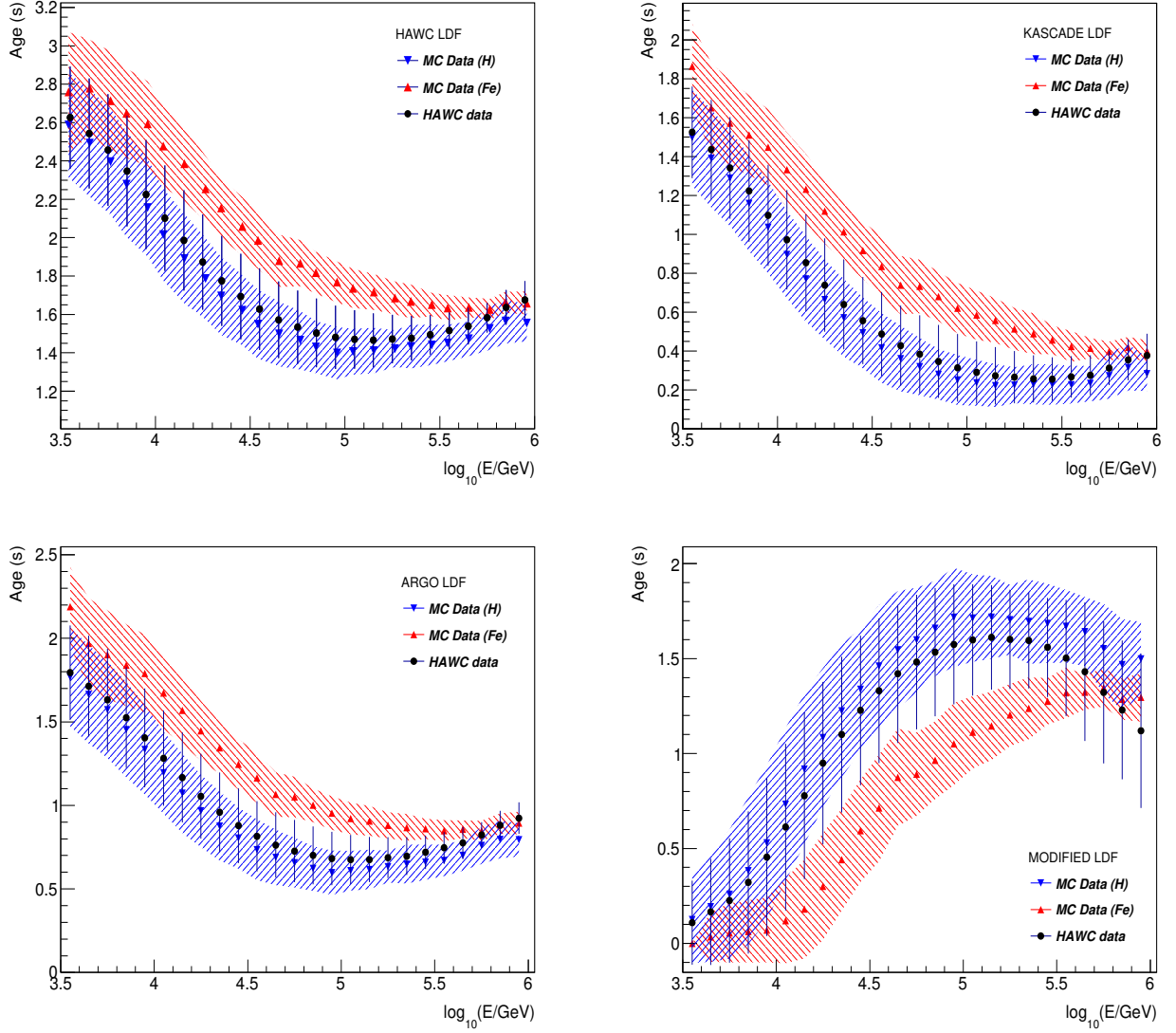


Figure 6.6: Mean lateral age parameter as a function of the energy estimated from the fit performed with HAWC LDF (5.15) (top left), KASCADE LDF (5.16) (top right), ARGO LDF (5.18) (bottom left) and Modified Scaling LDF (5.20) (bottom right) to MC (triangles) and experimental data (circles). The error bands of each component correspond to a  $1\sigma$  containment error in the MC simulations and the error bars to the  $1\sigma$  statistical uncertainty of the measured data.

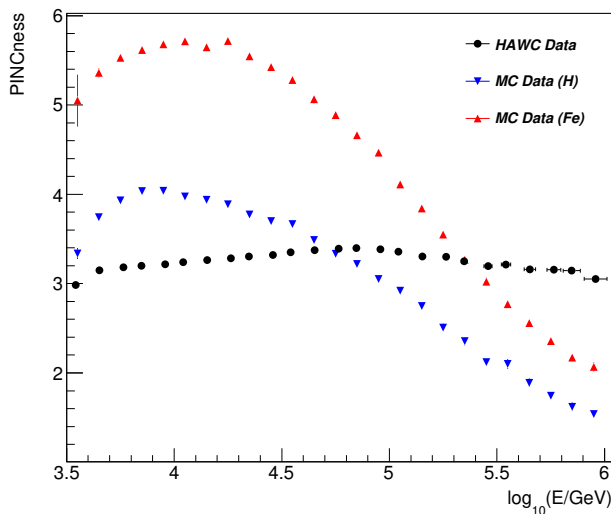


Figure 6.7: Mean PINCness vs the reconstructed energy as calculated for MC protons and iron nuclei (triangles) compared with the measured data (circles).

estimation of the age parameter. The resulting mean lateral age parameter for MC simulations and measured data is shown in fig. 6.12 as function of the energy.

## 6.5 Discussion

### 6.5.1 Parameterization of the lateral distribution of EAS induced by cosmic rays

First, the quality of the fits made with the eqs. (5.15), (5.16), (5.18) and (5.20) will be analyzed based on the results shown in the figures 5.5 and 6.4. From these analysis, it will be discussed the implications for the determination of the LDF that best describes the lateral distribution of air showers induced by cosmic rays in measured data and simulations.

From the results presented at figs. 5.5 and 6.4 for MC and experimental data, it can be seen that the quality of the description of the LDFs varies depending on the energy region. In the low energy region ( $E \lesssim 10^{4.5}$  GeV), for experimental data and MC simulations, the eqs. HAWC LDF (5.15) and KASCADE LDF (5.16) give a better description of the data, while in the energy regime between  $10^{4.5}$  GeV and  $10^{5.5}$  GeV, eqs. HAWC LDF (5.15) and ARGO LDF (5.18) fit better the measured data, but for the MC simulations the eqs. ARGO LDF (5.18) and Modified Scaling Formalism LDF (5.20) work better in that energy regime. On the other hand, at energies  $E > 10^{5.5}$  GeV the quality in the description of the data decreases, but not for the MC simulations. In any case, the fits with eqs. (5.15) and (5.18) at higher energies are better than at low energies. This difference between the experimental and MC results at energies  $E > 10^{5.5}$  GeV may be because the shape of the lateral distribution for measured and simulated air showers is different in this energy region. In addition, it was also found that non of the selected LDF's describes the experimental and MC data in all the energy range according to the above figures. In any case, we see that the HAWC LDF (5.15) seems to give an accurate description of the experimental and MC data at all energies in comparison to the other LDF's.

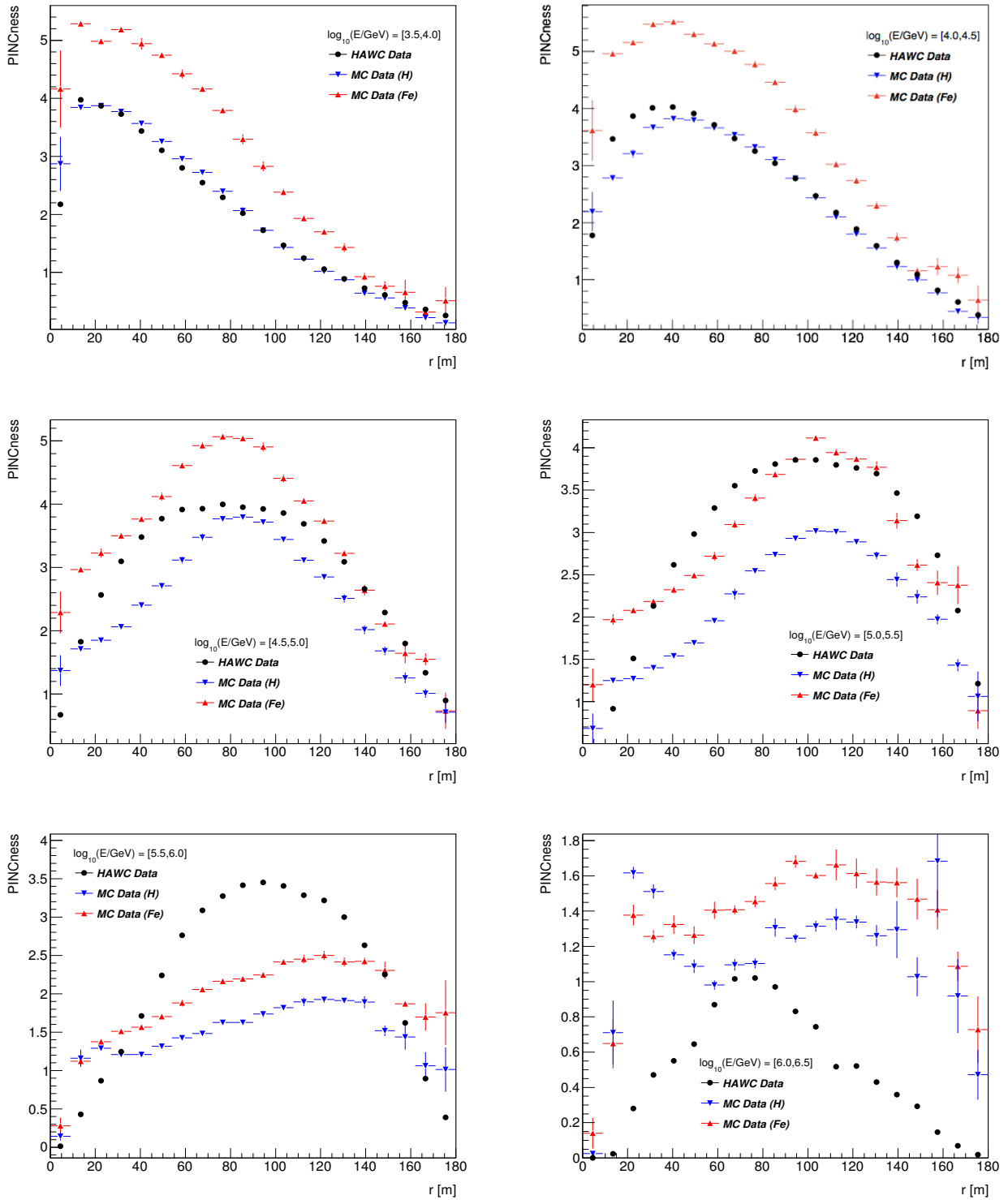


Figure 6.8: Mean PINCness as a function of the lateral distance to the shower core for different energy intervals obtained for MC simulations and experimental data. The black dots correspond to HAWC data and the triangles represent the simulated proton (blue) and iron (red) nuclei.

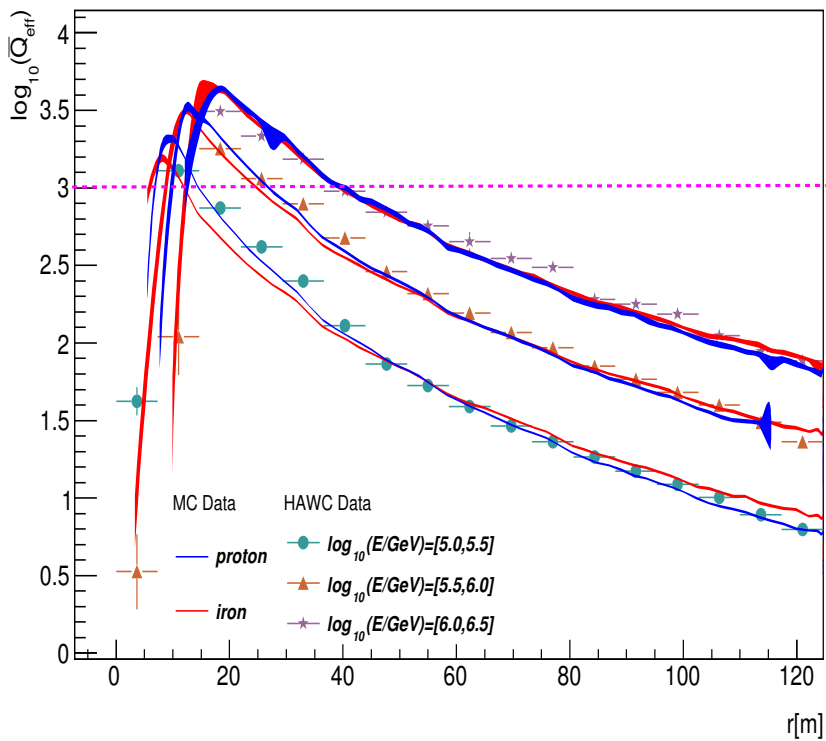
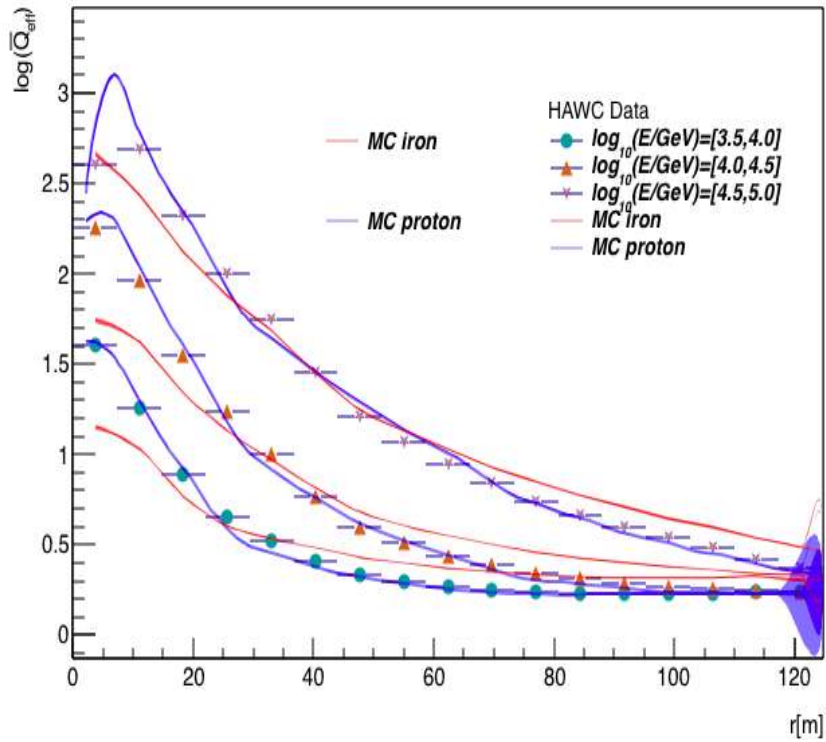


Figure 6.9: Lateral distribution of a mean EAS for low (left panel) and high (right panel) energies corresponding to the MC (blue bands: proton; red bands: iron) and experimental (solid markers) data. The error on the mean is smaller than the marker size for experimental data. The error band shows the error on the mean for the simulated data. Right: the dashed line points a deviation in the behaviour of the experimental data near the shower core region and above  $\bar{Q}_{eff}(r) = 3$  PE.

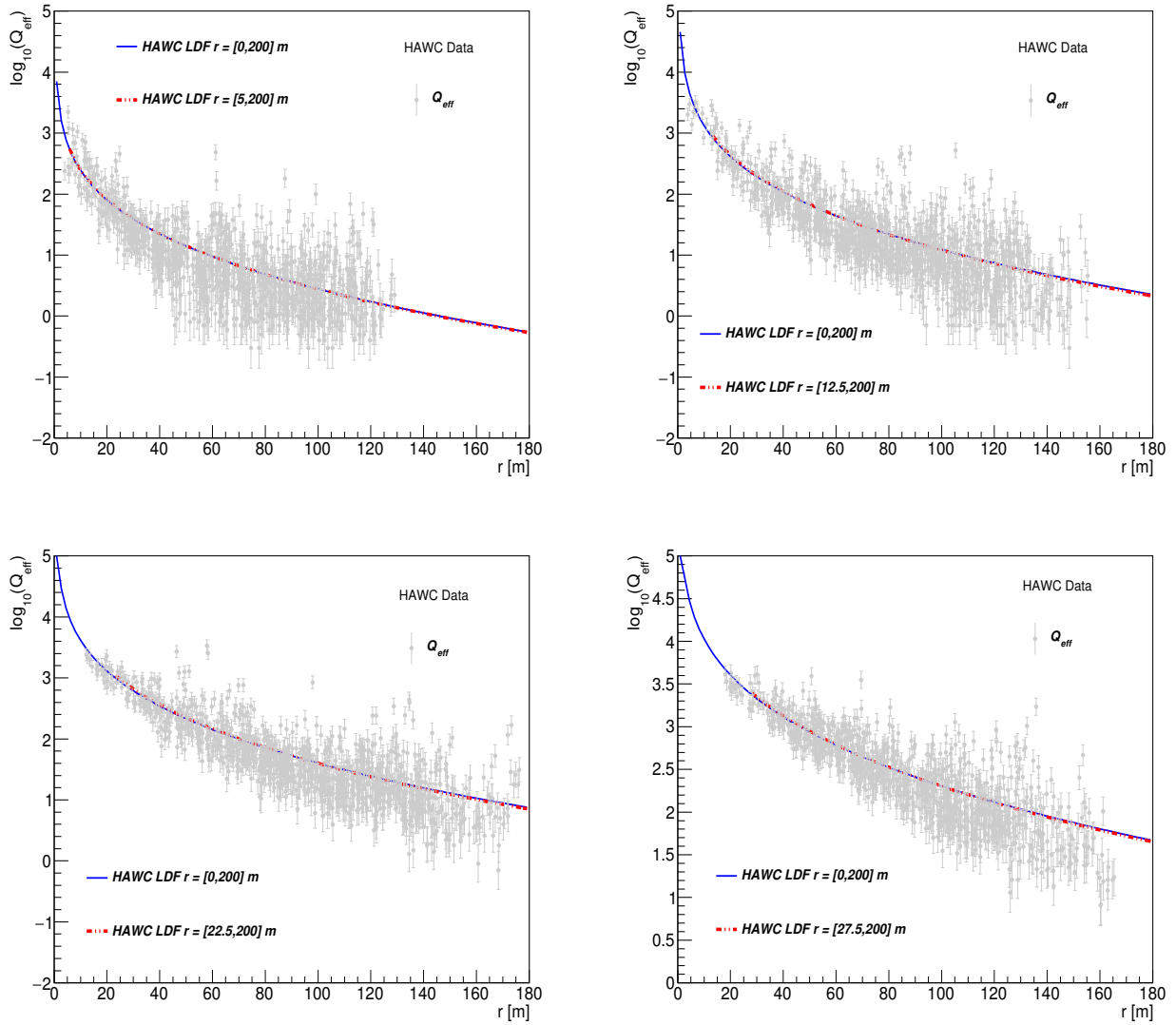


Figure 6.10: Fits over the lateral distribution of some EAS event examples measured with HAWC for different radial intervals using HAWC's LDF (5.15). These events have energies of  $10^{64.5}$  GeV (top left),  $10^{5.05}$  GeV (top right),  $10^{5.55}$  GeV (bottom left) and  $10^{6.05}$  GeV (bottom right).

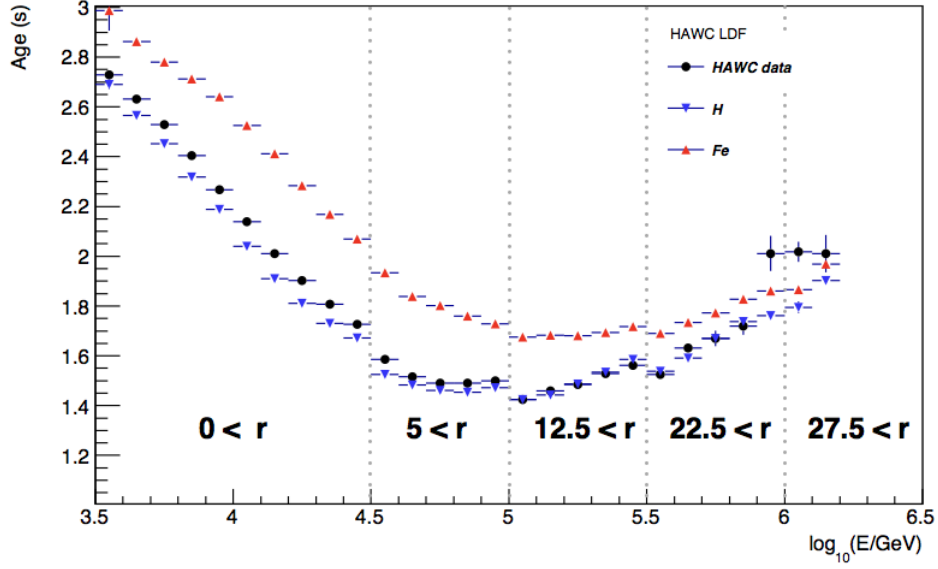


Figure 6.11: Mean shower age for MC simulations (triangles) and measured data (circles) as a function of the energy estimated using eq. (5.15) for the radial cuts shown in table 6.1. In the figure,  $r$  has units of m.

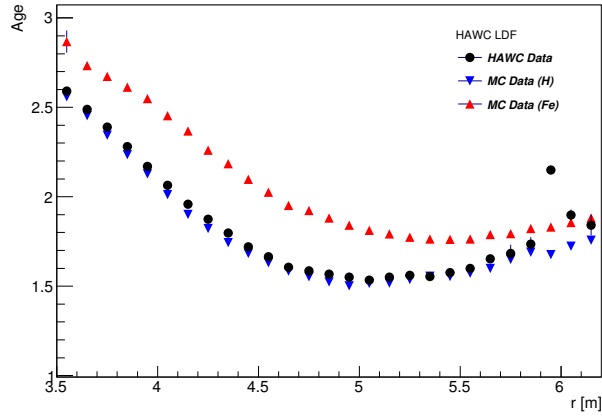


Figure 6.12: Mean lateral age parameter as function of the energy for experimental (circles) and MC (triangles) data estimated from the results of the fit of HAWC LDF (5.15) after a cut on the effective charge,  $\log_{10}(Q_{eff}) < 3$  PE, deposited at each PMT.

## 6.5.2 Dependence of the age parameter on the parameterization of the LDF

Now, the influence of the LDF in the behaviour of the lateral shower age will be analyzed. First, the results of the fits made with the eqs. (5.15), (5.16), (5.18) and (5.20) are shown in fig. 6.5. The observed shower age seems to have the same behaviour with the energy for the eqs. (5.15), (5.16) and (5.18), but not for eq. (5.20). It's important to point out that, due to the way in which the

*age parameter* ( $s$ ) was added in the Modified Scaling Formalism LDF (5.20), it no longer behaves as the lateral shower age parameter. However, it still describes the shape or form of the lateral density distribution of EAS, besides, as it is seen in figs. 6.6, it is still sensitive to the primary mass composition. The  $s$  parameter for the Modified Scaling Formalism LDF (5.20) behaves in an inverse way to the shower age defined by the other LDF's.

As a next step, the mean values of the shower age for measured data are going to be compared with MC predictions, this is done in figs. 6.6. The deviation between the mean lateral shower age for measured air showers and the MC predictions at energies  $E > 10^{5.5}$  GeV doesn't disappear, which indicates that such deviation doesn't depend on the LDF used in the fit of the lateral distribution, but from the data itself.

### 6.5.3 Study of the sensitivity of the age parameter to the composition of cosmic rays

The lateral shower age dependence to the mass composition of cosmic rays is going to be discussed from the results of the figure of merit shown in fig. 5.8.

According to MC simulations, the value of the FOM for the proton and iron populations is greater than 1 for energies  $E > 10^{3.8}$  GeV and reaches its maximum at  $E = 10^{4.8}$  GeV, and then it starts to decrease. At  $E = 10^{5.5}$  GeV the FOM has the value 1.75 (see fig. 5.8). A value of the FOM equal to 1 indicates that the means of the two populations are separated by one standard deviation. The initial behaviour of the FOM distributions for both MC populations is because the values of the error bands of both populations overlap. At high energies it is expected that the value of the FOM would continue to be constant, but it decreases, this may be because the distance between the distribution of both populations becomes smaller, may be due to the size of the detector, which is not able to fully contain air showers at high energies. The FOM values bigger than 1 indicates that the mass composition of cosmic rays measured with HAWC can be well studied in an energy region from  $10^{3.8}$  GeV to approximately  $10^{5.8}$  GeV.

Finally, the comparison of the experimental data with the MC simulations indicates that the light component of cosmic rays at least up to energies of  $E = 10^{5.5}$  GeV is more abundant in the cosmic ray flux because the mean value of the experimental shower age lies in the MC region for light nuclei.

### 6.5.4 Analysis of PINCness as a mass composition parameter

Now, the behaviour of the PINCness will be analyzed. From fig. 6.7 it can be observed that the mean PINCness as a function of the reconstructed energy distribution of the measured EAS with HAWC has approximately a constant behaviour through out the energy range from  $10^{3.5}$  GeV to  $10^{6.2}$  GeV. Also, a strong deviation in the energy regions  $\log_{10}(E/GeV) = [3.5, 4.7]$  and  $\log_{10}(E/GeV) = [5.5, 6.2]$  of the mean measured PINCness from the MC predictions is observed. Therefore, this parameter can not be used for mass composition studies. To find out which radial regions contributes more to the observed deviation, the PINCness as a function of the lateral distance to the shower core was studied as well. The results of the distribution of the PINCness as function of the distance to the shower core for different energy intervals are shown in fig. 6.8. In general, in the low energy regime (from  $10^{3.5}$  GeV to  $10^{4.5}$  GeV) the PINCness values for the experimental data and MC predictions are bigger near the shower core region between  $r = 40$  m and 80 m. On the other hand, in the high energy regime ( $10^{4.5}$  GeV to  $10^{6.5}$  GeV), there is no agreement between the experimental PINCness distribution and the MC predictions, but in a very limited radial range.

### 6.5.5 Test of the predictions of the QGSJET-II-03 hadronic interaction model using the $Q_{eff}(r)$ data

To test the interaction models the measured mean lateral distributions of EAS were compared with MC predictions for protons and iron nuclei at six different energy intervals from  $E = 10^{3.5}$  GeV to  $10^{6.5}$  GeV (see figs. 6.9). In the energy intervals from  $E = 10^{3.5}$  GeV to  $10^{5.5}$  GeV, the measured mean lateral distribution of EAS measured with HAWC lies within the MC predictions. At energies  $E > 10^{5.5}$  GeV, the experimental mean lateral distributions are not in agreement with the predictions of the hadronic interaction model QGSJET-II-03. As we see from the figures, some of the values of the mean lateral distributions of the data are above the expectations.

### 6.5.6 Dependence of the anomaly in the shower age on the $Q_{eff}$ data close to the EAS core region and with large values

From fig. 6.9 (bottom), it was found that the measured data for the mean lateral distribution of EAS deviate from MC predictions near the shower core region at  $E > 10^5$  GeV. This deviation suggests an effect of the shower core region in the deviation of the lateral shower age observed in the same energy regime. In section 6.4, the lateral age shower was estimated again, but leaving out the values of the  $Q_{eff}(r)$  near the shower core in the fits of the lateral distributions with eq. (5.15). The results were presented in fig. 6.11. In this figure it is noticed that there is a better agreement between the expectations and the data for the lateral shower age at high energies which means that in fact the behavior of the lateral distribution near the shower core is contributing to the observed anomaly.

#### 6.10

On the other hand, from figs. 6.9 at high energies, for a given energy interval, it is observed that the experimental data points do not follow the same composition tendency close to the core than outside the core region. One should expect the same tendency regardless of the lateral distance to the shower core. The composition must be unique inside the same energy bin but it is observed that close to the shower core, it is changing because the experimental primaries tend to move from one MC composition curve to another. It was pointed out in section 6.4 that for points near to  $Q_{eff}(r) = 3$  there seems to be some kind of saturation that contributes to the above behaviour of the measured composition near the core. For this purpose to study the influence of this potential effect of saturation the fits were repeated again but applying a cut  $\log_{10}(Q_{eff}) > 3$  PE as explained in section 6.4 and the results are shown in fig. 6.12.

It can be seen that after applying the above cut there is a better agreement between the measured lateral age parameter and the MC predictions up to energies of  $E \sim 10^{5.8}$  GeV, which indicates that the deviation of the age parameter observed in fig. 5.1 may be due to differences in the effective charge for  $\log_{10}(Q_{eff}) > 3$  PE.

# Chapter 7

## Conclusions

From this analysis, it has been found that none of the selected LDFs describes satisfactorily the measured data for all radial ranges and energies. However, it was found that HAWC's LDF gives a good description of the data in the energy range between  $E = 10^{3.5} - 10^{6.2}$  GeV in comparison with the other LDFs. The deviation on the behaviour of the distribution of the age parameter is still present at least at energies  $E > 10^{5.8}$  GeV for the fits with different LDFs of the  $\bar{Q}_{eff}(r)$  data, which shows that this feature at higher energies is independent from the parameterization chosen for the description of the lateral distribution of air shower data measured with HAWC.

The sensitivity of the lateral age parameter to the mass composition of cosmic rays in the energy interval from  $10^{3.5}$  GeV to  $10^{6.2}$  GeV was also studied in this work. From the results of the FOM it can be ensured that it is possible to perform mass composition studies with HAWC's data in an energy interval between  $E = 10^{3.8} - 10^{5.5}$  GeV using the lateral age parameter. The experimental lateral shower age distribution is in the light mass component region, which indicates that the light mass component is more abundant in the cosmic ray flux at energies  $E < 10^{5.5}$  GeV.

It is of great importance to reduce the systematical errors in the reconstruction of the lateral age parameter to apply it in the study of the all particle and light (H + He) energy spectra of cosmic rays with the highest possible precision.

In an attempt to use the PINCness parameter in the study of the mass composition it was found that this observable is not useful for this purpose due to the deviations in PINCness observed between data and simulations.

It was also found that the average  $Q_{eff}(r)$  of an EAS is within the predictions of the hadronic interaction model QGSJET-II-03 in the energy range between  $10^{3.5}$  GeV to  $10^{5.5}$  GeV. In particular, in the energy intervals  $\log_{10}(E/GeV) = [5.5, 6.0]$  and  $\log_{10}(E/GeV) = [6.0, 6.5]$  the average  $\bar{Q}_{eff}(r)$  of an EAS seems to be above the predictions of the hadronic interaction model QGSJET-II-03 in  $r = [20, 110]$  m. In addition to these observations, from the above comparisons between the  $\bar{Q}_{eff}(r)$  for measured and MC data, it can also be seen a deviation in the behaviour of the experimental curves from the MC predictions near the shower core, which increases radially with the energy. The previous analysis over the high energy events helped to suggest a deviation in the  $Q_{eff}$  data from the expectations in the shower core regions and also for data  $Q_{eff} > 10^3$ . The last observations may suggest three hypotheses about the origin of the deviation of the lateral age parameter at high energies: The corresponding deviation may be a consequence of 1) the systematical errors of the measurements in the PMTs near the shower core of high energy events, 2) a problem in the calibration of data or 3) deviations between predictions of the model and the data.

# Bibliography

- [1] C. A. de Coulomb, *Mem. de l'Acad. des Sciences*, p. 612, 1875 (cit. on p. 1).
- [2] M. Bertolotti, “Celestial Messengers.” Springer Berlin Heidelberg, 2013, ISBN: 978-3-642-28370-3 (cit. on pp. 1–4, 7, 9).
- [3] C. V. Boys, “Quartz as an insulator,” *Proceedings of the Physical Society of London*, vol. 10, no. 1, p. 128, 1888 (cit. on pp. 1, 2).
- [4] van Leest antiques. (2017), [Online]. Available: <http://www.vanleestantiques.com/product/kolbes-electrometer-c-1890/> (cit. on p. 3).
- [5] R. G. A. Fricke and K. Schlegel, “Julius elster and hans geitel – dioscuroi of physics and pioneer investigators in atmospheric electricity,” *History of Geo- and Space Sciences*, vol. 8, no. 1, pp. 1–7, 2017. DOI: 10.5194/hgss-8-1-2017 (cit. on pp. 2, 3, 9).
- [6] J. Lacki, “Albert Gockel, a pioneer in atmospheric electricity and cosmic radiation,” *Astroparticle Physics*, vol. 53, pp. 27–32, Jan. 2014, ISSN: 0927-6505. DOI: 10.1016/J.ASTROPARTPHYS.2013.05.006 (cit. on pp. 4, 5).
- [7] A. Gockel, “Luftelektrische beobachtungen bei einer ballonfahrt,” *Physikalische Zeitschrift*, vol. 11, pp. 280–282, 1910 (cit. on p. 4).
- [8] “Luftelektrische beobachtungen bei einer ballonfahrt,” *Phys. Zeit.*, vol. 11, pp. 280–282, 1910 (cit. on p. 5).
- [9] M. Walter and A. W. Wolfendale, “Early history of cosmic particle physics,” *The European Physical Journal H*, vol. 37, no. 3, pp. 323–358, 2012, ISSN: 2102-6467. DOI: 10.1140/epjh/e2012-30020-1 (cit. on pp. 5, 9).
- [10] J. R. Hörandel, “Early cosmic-ray work published in German,” *AIP Conference Proceedings*, vol. 1516, no. June 2012, pp. 52–60, 2013, ISSN: 0094243X. DOI: 10.1063/1.4792540. arXiv: 1212.0706 (cit. on pp. 5, 6, 9).
- [11] D. Pacini, “La radiazione penetrante alla superficie ed in seno alle acque,” *Il Nuovo Cimento (1911-1923)*, vol. 3, no. 1, pp. 93–100, Dec. 1912, ISSN: 1827-6121. DOI: 10.1007/BF02957440 (cit. on p. 5).
- [12] V. F. Hess, *Phys. Zeit.*, vol. 13, 1912 (cit. on pp. 5, 6).
- [13] V. F. Hess, “ÜBER BEOBACHTUNGEN DER DURCHDRINGENDEN STRAHLUNG BEI SIEBEN FREIBALLONFAHRTEN,” *Physikalische Zeitschrift*, vol. 13, pp. 1084–1091, Nov. 1912 (cit. on p. 6).
- [14] M. Kachelrieß, “Lecture notes on high energy cosmic rays,” *17.th Jyväskylä Summer School*, Aug. 2007 (cit. on pp. 6, 9, 10, 29).

- [15] P. Biermann and G. Sigl, “Introduction to Cosmic Rays,” vol. 576, pp. 1–26, 2002. DOI: 10.1007/3-540-45615-5\_1. arXiv: 0202425 [astro-ph] (cit. on pp. 6, 12, 13, 15).
- [16] V. Hess, “On the observations of the penetrating radiation during seven balloon flights,” *arXiv preprint arXiv:1808.02927*, 2018 (cit. on p. 6).
- [17] T. N. Y. Times. (2012), [Online]. Available: <https://www.nytimes.com/2012/08/07/science/space/when-victor-hess-discovered-cosmic-rays-in-a-hydrogen-balloon.html> (cit. on p. 7).
- [18] W. Kolhörster, “Messungen der durchdringenden strahlungen bis in höhen von 9300,” *Verh. deutsche phys. Gesellschaft*, pp. 719–721, 1914 (cit. on p. 6).
- [19] R. A. Millikan and G. H. Cameron, *Phys. Rev.*, vol. 28, p. 856, 1926 (cit. on p. 7).
- [20] R. A. Millikan and G. H. Cameron, “The origin of the cosmic rays,” *Phys. Rev.*, vol. 32, pp. 533–557, 4 Oct. 1928. DOI: 10.1103/PhysRev.32.533 (cit. on p. 7).
- [21] Getty Images. (1999), [Online]. Available: <http://www.pnas.org/content/20/5/259.extract> (cit. on p. 8).
- [22] L. Bonolis, “From cosmic ray physics to cosmic ray astronomy: Bruno Rossi and the opening of new windows on the universe,” *Astroparticle Physics*, vol. 53, no. C, pp. 67–85, 2014, ISSN: 09276505. DOI: 10.1016/j.astropartphys.2013.05.008. arXiv: 1211.4061 (cit. on pp. 7–9, 21).
- [23] B. Rossi, “EARLY DAYS IN COSMIC RAYS,” *Phys. Today*, vol. 34, pp. 34–41, 1981. DOI: 10.1063/1.2914331 (cit. on p. 7).
- [24] L. Alvarez and A. H. Compton, “A positively charged component of cosmic rays,” *Phys. Rev.*, vol. 43, pp. 835–836, 10 May 1933. DOI: 10.1103/PhysRev.43.835 (cit. on p. 8).
- [25] T. H. Johnson, “The azimuthal asymmetry of the cosmic radiation,” *Phys. Rev.*, vol. 43, pp. 834–835, 10 May 1933. DOI: 10.1103/PhysRev.43.834 (cit. on p. 8).
- [26] P. Auger, R. Maze, and T. Grivet-Meyer, “Grandes gerbes cosmiques atmosphériques contenant des corpuscules ultrapénétrants,” *Comptes Rendus de l’Académie des Sciences*, vol. 206, pp. 1721–1723, 1938 (cit. on pp. 8, 22).
- [27] V. Cirkel-bartelt, “History of Astroparticle Physics and its Components Imprint / Terms of Use,” *Living Reviews in Relativity*, 2008, ISSN: 0883-9417 (cit. on p. 9).
- [28] CERN. (2017). Cern timeline, [Online]. Available: <http://timeline.web.cern.ch/timelines/Cosmic-rays> (cit. on p. 9).
- [29] N. Hilberry, “Extensive Cosmic-Ray Showers and the Energy Distribution of Primary Cosmic Rays,” *The Physical Review*, vol. 60, no. 1, 1941 (cit. on p. 10).
- [30] I. S. Bowen, R. A. Millikan, and H. V. Neher, “New light on the nature and origin of the incoming cosmic rays,” *Phys. Rev.*, vol. 53, pp. 855–861, 11 Jun. 1938. DOI: 10.1103/PhysRev.53.855 (cit. on p. 10).
- [31] W. Baade and F. Zwicky, “Cosmic rays from super-novae,” *Proceedings of the National Academy of Sciences*, vol. 20, no. 5, p. 259, 1934. DOI: 10.1073/pnas.20.5.259 (cit. on p. 11).

- [32] A. Bell, “Cosmic ray acceleration,” *Astroparticle Physics*, vol. 43, pp. 56–70, 2013, Seeing the High-Energy Universe with the Cherenkov Telescope Array - The Science Explored with the CTA, ISSN: 0927-6505. DOI: <https://doi.org/10.1016/j.astropartphys.2012.05.022> (cit. on p. 11).
- [33] Auger Collaboration, “Correlation of the highest-energy cosmic rays with nearby extragalactic objects,” *Science*, vol. 318, no. 5852, pp. 938–943, 2007, ISSN: 0036-8075. DOI: [10.1126/science.1151124](https://doi.org/10.1126/science.1151124). eprint: <http://science.sciencemag.org/content/318/5852/938.full.pdf> (cit. on pp. 11, 34, 35).
- [34] The IceCube Collaboration, “Neutrino emission from the direction of the blazar txs 0506+056 prior to the icecube-170922a alert,” *Science*, vol. 361, no. 6398, pp. 147–151, 2018, ISSN: 0036-8075. DOI: [10.1126/science.aat2890](https://doi.org/10.1126/science.aat2890). eprint: <https://science.sciencemag.org/content/361/6398/147.full.pdf> (cit. on pp. 11, 16).
- [35] P. Baerwald, M. Bustamante, and W. Winter, “Are gamma-ray bursts the sources of ultra-high energy cosmic rays?” *Astroparticle Physics*, vol. 62, pp. 66–91, 2015, ISSN: 0927-6505. DOI: <https://doi.org/10.1016/j.astropartphys.2014.07.007> (cit. on p. 11).
- [36] C. D. Dermer and J. M. Holmes, “Cosmic rays from gamma-ray bursts in the galaxy,” *The Astrophysical Journal*, vol. 628, no. 1, pp. L21–L24, Jun. 2005. DOI: [10.1086/432663](https://doi.org/10.1086/432663) (cit. on p. 11).
- [37] L. collaboration *et al.*, “Fermi large area telescope fourth source catalog,” *arXiv preprint arXiv:1902.10045*, 2019 (cit. on p. 11).
- [38] Particle Data Group, C. Patrignani, *et al.*, “Review of Particle Physics,” *Chinese Physics C*, vol. 40, p. 10001, 2016. DOI: [10.1088/1674-1137/40/10/100001](https://doi.org/10.1088/1674-1137/40/10/100001) (cit. on pp. 12, 13, 24).
- [39] E. Fermi, “On the origin of the cosmic radiation,” *Physical Review*, vol. 75, no. 8, 1949 (cit. on p. 12).
- [40] K.-H. Kampert and A. A. Watson, “Extensive air showers and ultra high-energy cosmic rays: a historical review,” *The European Physical Journal H*, vol. 37, no. 3, pp. 359–412, 2012, ISSN: 2102-6467. DOI: [10.1140/epjh/e2012-30013-x](https://doi.org/10.1140/epjh/e2012-30013-x) (cit. on pp. 12, 21).
- [41] Helmholtz Alliance for Astroparticle Physics. (2017), [Online]. Available: <http://www.hap-astroparticle.org/184.php> (cit. on p. 13).
- [42] P. K. F. Grieder, “Extensive Air Showers.” Springer-Verlag Berlin Heidelberg, 2010, vol. 1, p. 1118, ISBN: 978-3-540-76940-8. DOI: [10.1007/978-3-540-76941-5](https://doi.org/10.1007/978-3-540-76941-5) (cit. on pp. 12–15, 28, 29, 32, 34, 35, 48, 49).
- [43] D. R. Bergman and J. W. Belz, “Cosmic rays: The second knee and beyond,” *Journal of Physics G: Nuclear and Particle Physics*, vol. 34, no. 10, R359–R400, Sep. 2007. DOI: [10.1088/0954-3899/34/10/r01](https://doi.org/10.1088/0954-3899/34/10/r01) (cit. on p. 12).
- [44] D.-Y. Chung, “The knees-ankles-toe in cosmic rays and the periodic table of elementary particles,” *Journal of Modern Physics*, vol. 5, pp. 1467–1472, Sep. 2014. DOI: [10.4236/jmp.2014.515148](https://doi.org/10.4236/jmp.2014.515148) (cit. on p. 12).

- [45] S. Thoudam, J. P. Rachen, A. van Vliet, *et al.*, “Cosmic-ray energy spectrum and composition up to the ankle - the case for a second Galactic component,” *Astronomy & Astrophysics*, vol. 595, p. 23, 2016, ISSN: 14320746. DOI: 10.1051/0004-6361/201628894. arXiv: 1605.03111 (cit. on p. 12).
- [46] D. R. Bergman and J. W. Belz, “Cosmic rays: the Second Knee and beyond,” *Journal of Physics G: Nuclear and ...*, vol. 34, no. 1912, 2007, ISSN: 0954-3899. DOI: 10.1088/0954-3899/34/10/R01. arXiv: 0704.3721 (cit. on p. 12).
- [47] V. Souza, W. D. Apel, J. C. Arteaga, *et al.*, “The kascade-grande experiment,” *AIP Conference Proceedings*, vol. 1123, pp. 211–216, Apr. 2009. DOI: 10.1063/1.3141357 (cit. on p. 13).
- [48] T. Antoni, W. Apel, A. Badea, *et al.*, “KASCADE measurements of energy spectra for elemental groups of cosmic rays: Results and open problems,” *Astroparticle Physics*, vol. 24, no. 1–2, pp. 1–25, 2005, ISSN: 0927-6505. DOI: 10.1016/j.astropartphys.2005.04.001 (cit. on p. 13).
- [49] W. D. Apel, J. C. Arteaga-Velázquez, K. Bekk, *et al.*, “Kneelike structure in the spectrum of the heavy component of cosmic rays observed with kascade-grande,” *Physical review letters*, vol. 107, p. 171 104, Oct. 2011. DOI: 10.1103/PhysRevLett.107.171104 (cit. on p. 14).
- [50] W. Apel, J. Arteaga-Velázquez, K. Bekk, *et al.*, “Kascade-grande measurements of energy spectra for elemental groups of cosmic rays,” *Astroparticle Physics*, vol. 47, pp. 54–66, 2013, ISSN: 0927-6505. DOI: <https://doi.org/10.1016/j.astropartphys.2013.06.004> (cit. on p. 14).
- [51] J. C. Arteaga-Velázquez, “The KASCADE-Grande experiment: measurements of the all-particle energy spectrum of cosmic rays,” *XVI International Symposium on Very High Energy Cosmic Ray Interactions ISVHECRI 2010*, arXiv: arXiv:1009.4716v1 (cit. on p. 14).
- [52] S. G. Mashnik, “On solar system and cosmic rays nucleosynthesis and spallation processes,” *Los Alamos National Laboratory Report LA-UR-00-3658*, 2000. arXiv: 0008382v1 [arXiv:astro-ph] (cit. on p. 14).
- [53] P. Maestro, “Cosmic rays: direct measurements,” in *The 34th International Cosmic Ray Conference*, PoS - Proceedings of Science, 2015. arXiv: 1510.07683 (cit. on p. 15).
- [54] A. W. Strong, I. V. Moskalenko, and V. S. Ptuskin, “Cosmic-ray propagation and interactions in the galaxy,” *Annual Review of Nuclear and Particle Science*, vol. 57, no. 1, pp. 285–327, 2007. DOI: 10.1146/annurev.nucl.57.090506.123011. eprint: <https://doi.org/10.1146/annurev.nucl.57.090506.123011> (cit. on p. 15).
- [55] M. Aguilar, D. Aisa, B. Alpat, *et al.*, “Precision Measurement of the Helium Flux in Primary Cosmic Rays of Rigidities 1.9 GV to 3 TV with the Alpha Magnetic Spectrometer on the International Space Station,” vol. 211101, no. November, pp. 1–9, 2015. DOI: 10.1103/PhysRevLett.115.211101 (cit. on pp. 15, 20, 56).
- [56] E. G. Berezhko, “Cosmic rays from active galactic nuclei,” *The Astrophysical Journal*, vol. 684, Sep. 2008. DOI: 10.1086/592233 (cit. on p. 16).

- [57] G. Pelletier and E. Kersalé, “Acceleration of uhe cosmic rays in gamma-ray bursts,” *Astronomy and Astrophysics*, vol. 361, Aug. 2000 (cit. on p. 16).
- [58] by the IceCube Collaboration, Fermi-LAT, MAGIC, AGILE, ASAS-SN, HAWC, H.E.S.S., INTEGRAL, KANATA, KISO, KAPTEYN, LIVERPOOL TELESCOPE, SUBARU, SWIFT/NUSTAR, VERITAS, VLA/17B-403 teams, “Multimessenger observations of a flaring blazar coincident with high-energy neutrino icecube-170922a,” *Science*, vol. 361, no. 6398, 2018, ISSN: 0036-8075. DOI: 10.1126/science.aat1378. eprint: <http://science.sciencemag.org/content/361/6398/eaat1378.full.pdf> (cit. on p. 16).
- [59] C. Grupen, “Astroparticle Physics.” Springer-Verlag Berlin Heidelberg, 2005, vol. 1, ISBN: 978-3-540-25312-9. DOI: 10.1007/3-540-27670-X (cit. on pp. 16, 24).
- [60] E. Fermi, “On the origin of the cosmic radiation,” *Phys. Rev.*, vol. 75, pp. 1169–1174, 8 Apr. 1949. DOI: 10.1103/PhysRev.75.1169 (cit. on p. 16).
- [61] M. S. Longair and Malcolm S. Longair, “High Energy Astrophysics, 3rd edn., by Malcolm S. Longair.” 2011, p. 880, ISBN: 978-0-521-75618-1. DOI: 10.1080/00107514.2011.647089. eprint: 9903263 (astro-ph) (cit. on pp. 16, 17, 48).
- [62] M. Bustamante, G. D. C. Montoya, W. De Paula, *et al.*, “High-energy cosmic-ray acceleration,” *2009 CERN-Latin-American School of High-Energy Physics, CLASHEP 2009 - Proceedings*, pp. 533–539, 2010 (cit. on p. 17).
- [63] B. Dawson, “Ultra-High Energy Cosmic Rays Ultra-High Energy Cosmic Rays,” vol. 35, no. 6, pp. 1845–1861, 2009. DOI: 10.5170/CERN-2015-001.169. arXiv: 1604.07584 (cit. on pp. 18, 20).
- [64] B. Peters, “Primary cosmic radiation and extensive air showers,” *Il Nuovo Cimento (1955-1965)*, vol. 22, no. 4, pp. 800–819, 1961, ISSN: 1827-6121. DOI: 10.1007/BF02783106 (cit. on p. 18).
- [65] A. M. Hillas, “The origin of ultra-high-energy cosmic rays,” *Annual Review of Astronomy and Astrophysics*, vol. 22, pp. 425–444, Sep. 1984 (cit. on p. 18).
- [66] M. Ahlers, L. A. Anchordoqui, J. Becker, *et al.*, *FERMILAB-FN-0847-A, YITP-SB-10-01.*, 2010 (cit. on p. 19).
- [67] T. K. Gaisser, “Spectrum of cosmic-ray nucleons, kaon production, and the atmospheric muon charge ratio,” *Astroparticle Physics*, vol. 35, no. 12, pp. 801–806, 2012, ISSN: 09276505. DOI: 10.1016/j.astropartphys.2012.02.010. arXiv: 1111.6675 (cit. on pp. 18, 19).
- [68] G. Morlino, “High Energy Cosmic Rays From Supernovae,” pp. 1–25, arXiv: arXiv: 1611.10054v1 (cit. on p. 20).
- [69] (). Galprop official web site, [Online]. Available: <https://galprop.stanford.edu/> (cit. on p. 20).
- [70] (). Galprop webrun, [Online]. Available: <https://galprop.stanford.edu/webrun/> (cit. on p. 20).
- [71] B. Rossi, “Misure sulla distribuzione angolare di intensita della radiazione penetrante all’asmara,” *La Ricerca Scientifica Supplemento*, vol. 1, no. 9-10, pp. 579–589, 1934, Cited By :1 (cit. on p. 21).

- [72] W. Kolhörster, I. Matthes, and E. Weber, “Gekoppelte höhenstrahlen,” *Naturwissenschaften*, vol. 26, no. 35, pp. 576–576, 1938, ISSN: 1432-1904. DOI: 10.1007/BF01773491 (cit. on p. 21).
- [73] A. Haungs, J. Blumer, B. Fuchs, *et al.*, “Kcdc—the kascade cosmic-ray data centre,” in *Journal of Physics: Conference Series*, IOP Publishing, vol. 632, 2015, p. 012011 (cit. on p. 22).
- [74] T. Pierog, R. Engel, and D. Heck, “Impact of uncertainties in hadron production on air-shower predictions,” *Czechoslovak Journal of Physics*, vol. 56, no. SUPPL. 1, pp. 1–12, 2006, ISSN: 00114626. DOI: 10.1007/s10582-006-0152-0. arXiv: 0602190 [astro-ph] (cit. on pp. 24–27).
- [75] T. Stanev, “High energy cosmic rays.” Springer Science & Business Media, 2010 (cit. on pp. 26, 32, 33).
- [76] J. Ranft, “DPMJET version II.5, code manual,” 2008. arXiv: 9911232v1 (cit. on p. 27).
- [77] S. Ostapchenko and D. Heck, “Hadronic Interactions in QGSJET-II : Physics and Results,” *29th International Cosmic Ray International COonference*, pp. 135–138, 2005 (cit. on pp. 27, 55).
- [78] F. Riehn and T. K. Gaisser, “A new version of the event generator Sibyll,” 2015. arXiv: arXiv:1510.00568v1 (cit. on p. 27).
- [79] T. Pierog, J. M. Katzy, E. Yatsenko, *et al.*, “EPOS LHC : test of collective hadronization with LHC data,” vol. 5, arXiv: arXiv:1306.0121v2 (cit. on p. 27).
- [80] A. Ferrari, P. R. Sala, and J. Ranft, “Fluka: A multi-particle transport code,” no. October 2005, 2011 (cit. on pp. 28, 55).
- [81] H. Fesefeldt, “The simulation of hadron showers rwth aachen report,” *PITHA*, 1985 (cit. on p. 28).
- [82] P. Lipari, “The Concepts of “Age” and “Universality” in Cosmic Ray Showers,” pp. 1–27, arXiv: arXiv:0809.0190v1 (cit. on p. 29).
- [83] A. De Angelis, O. Mansutti, and M. Persic, “Very-high energy gamma astrophysics,” *arXiv preprint arXiv:0712.0315*, 2007 (cit. on p. 30).
- [84] A. Tapia, D. Melo, F. Sánchez, *et al.*, “The lateral shower age parameter as an estimator of chemical composition,” 2013. arXiv: arXiv:1309.3536v1 (cit. on p. 30).
- [85] K. Kamata and J. Nishimura, “The lateral and the angular structure functions of electron showers,” *Progress of Theoretical Physics Supplement*, vol. 6, pp. 93–155, 1958. DOI: 10.1143/PTPS.6.93. eprint: /oup/backfile/content\_public/journal/ptps/6/10.1143/ptps.6.93/2/6-93.pdf (cit. on pp. 30, 31, 53, 55).
- [86] K. Greisen, “Cosmic ray showers,” *Annual Review of Nuclear Science*, vol. 10, no. 1, pp. 63–108, 1960. DOI: 10.1146/annurev.ns.10.120160.000431. eprint: https://doi.org/10.1146/annurev.ns.10.120160.000431 (cit. on pp. 30, 31, 53).

- [87] T. Antoni, W. D. Apel, F. Badea, *et al.*, “Electron, Muon, and Hadron Lateral Distributions Measured in Air-Showers by the KASCADE Experiment,” no. February, pp. 1–28, 2008. arXiv: arXiv:astro-ph/0004233 (cit. on pp. 31, 37, 38, 40).
- [88] W. Apel, A. Badea, K. Bekk, *et al.*, “Comparison of measured and simulated lateral distributions for electrons and muons with cascade,” *Astroparticle Physics*, vol. 24, no. 6, pp. 467–483, 2006, ISSN: 0927-6505. DOI: <https://doi.org/10.1016/j.astropartphys.2005.10.001> (cit. on pp. 31, 38).
- [89] W. R. Leo, “Techniques for nuclear and particle physics experiments: a how-to approach.” Springer Science & Business Media, 2012 (cit. on p. 33).
- [90] R. J. Wilkes, “Technology of small emulsion chambers: A new review,” *AIP Conference Proceedings*, vol. 49, no. 1, pp. 63–71, 1979. DOI: 10.1063/1.31643. eprint: <https://aip.scitation.org/doi/pdf/10.1063/1.31643> (cit. on p. 33).
- [91] K. Asakimori, T. H. Burnett, M. L. Cherry, *et al.*, “Cosmic-Ray Proton and Helium Spectra: Results from the JACEE Experiment,” *The Astrophysical Journal*, vol. 502, no. 1, pp. 278–283, 1998, ISSN: 0004-637X. DOI: 10.1086/305882 (cit. on p. 33).
- [92] Y. S. Yoon, H. S. Ahn, P. S. Allison, *et al.*, “Cosmic-Ray Proton and Helium Spectra from the First CREAM Flight,” *The Astrophysical Journal*, vol. 728, no. 2, p. 8, Feb. 2011. DOI: 10.1088/0004-637X/728/2/122. arXiv: 1102.2575 (cit. on pp. 33, 56).
- [93] H. S. Ahn, P. Allison, M. G. Bagliesi, *et al.*, “Discrepant Hardening Observed in Cosmic-ray Elemental Spectra,” *The Astrophysical Journal Letters*, vol. 714, no. 1, p. L89, 2010 (cit. on p. 33).
- [94] H. S. Ahn, P. Allison, M. G. Bagliesi, *et al.*, “Energy Spectra of Cosmic-Ray Nuclei At High Energies,” *The Astrophysical Journal*, vol. 707, no. 1, pp. 593–603, 2009, ISSN: 0004-637X. DOI: 10.1088/0004-637X/707/1/593. arXiv: 0911.1889 (cit. on pp. 33, 56).
- [95] A. D. Panov, J. H. Adams, H. S. Ahn, *et al.*, “The energy spectra of heavy nuclei measured by the ATIC experiment,” *Advances in Space Research*, vol. 37, no. 10, pp. 1944–1949, 2006, ISSN: 02731177. DOI: 10.1016/j.asr.2005.07.040 (cit. on p. 33).
- [96] A. D. Panov, J. H. Adams, H. S. Ahn, *et al.*, “Energy spectra of abundant nuclei of primary cosmic rays from the data of ATIC-2 experiment: Final results,” *Bulletin of the Russian Academy of Sciences: Physics*, vol. 73, no. 5, pp. 564–567, 2009, ISSN: 1062-8738. DOI: 10.3103/S1062873809050098. arXiv: 1101.3246 (cit. on p. 33).
- [97] E. Atkin, V. Bulatov, V. Dorokhov, *et al.*, “The nucleon space experiment for direct high energy cosmic rays investigation in tev – pev energy range,” *Nuclear Inst. and Methods in Physics Research, A*, pp. 189–196, ISSN: 0168-9002. DOI: 10.1016/j.nima.2014.09.079 (cit. on p. 33).
- [98] Y. Yu, Z. Sun, H. Su, *et al.*, “The Plastic Scintillator Detector at DAMPE,” 2017. arXiv: 1703.00098 (cit. on p. 33).

- [99] V. S. Gallo, “Studies on helium flux with dampe,” *35<sup>th</sup> International Cosmic Ray Conference*, 2017 (cit. on p. 33).
- [100] P. S. Marrocchesi, “Calet: A calorimeter-based orbital observatory for high energy astroparticle physics for the calet collaboration,” *Nuclear Inst. and Methods in Physics Research, A*, vol. 692, no. 2012, pp. 240–245, 2014, ISSN: 0168-9002 (cit. on p. 33).
- [101] M. Bertaina, G. Battistoni, S. Muraro, *et al.*, “The cosmic ray primary spectrum in the transition region between direct and indirect measurements (10 TeV - 10 PeV),” *Journal of Physics: Conference Series*, vol. 120, no. 6, p. 62023, 2008. DOI: 10.1088/1742-6596/120/6/062023 (cit. on p. 34).
- [102] I. Collaboration *et al.*, “Cosmic ray spectrum and composition from pev to eev using 3 years of data from icetop and icecube,” *arXiv preprint arXiv:1906.04317*, 2019 (cit. on pp. 34, 44).
- [103] L. Kuzmichev, I. Astapov, P. Bezyazeev, *et al.*, “Tunka advanced instrument for cosmic rays and gamma astronomy (taiga): Status, results and perspectives,” *EPJ Web of Conferences*, vol. 145, p. 01001, Jan. 2017. DOI: 10.1051/epjconf/201614501001 (cit. on pp. 34, 35, 39).
- [104] F. Aharonian, A. Akhperjanian, A. Bazer-Bachi, *et al.*, “The hess survey of the inner galaxy in very high energy gamma rays,” *The Astrophysical Journal*, vol. 636, no. 2, p. 777, 2006 (cit. on pp. 35, 44).
- [105] A. Archer, W. Benbow, R. Bird, *et al.*, “Measurement of cosmic-ray electrons at tev energies by veritas,” *Physical Review D*, vol. 98, no. 6, p. 062004, 2018 (cit. on pp. 35, 44).
- [106] M. L. Ahnen, S. Ansoldi, L. Antonelli, *et al.*, “Performance of the magic telescopes under moonlight,” *Astroparticle Physics*, vol. 94, pp. 29–41, 2017 (cit. on pp. 35, 44).
- [107] P. Sokolsky, “Final Results from the High solution Fly’s Eye (HiRes) Experiment,” *Nuclear Physics B - Proceedings Supplements*, vol. 212-213, pp. 74–78, 2011, ISSN: 09205632. DOI: 10.1016/j.nuclphysbps.2011.03.010 (cit. on p. 35).
- [108] J. Petrovic, W. Apel, T. Asch, *et al.*, “Radio emission of highly inclined cosmic ray air showers measured with lopes,” *Astronomy & Astrophysics*, vol. 462, no. 1, pp. 389–395, 2007 (cit. on p. 35).
- [109] M. P. van Haarlem, M. W. Wise, A. Gunst, *et al.*, “Lofar: The low-frequency array,” *Astronomy and Astrophysics*, May 2013. DOI: 10.1051/0004-6361/201220873 (cit. on p. 35).
- [110] B. Bartoli, P. Bernardini, X. J. Bi, *et al.*, “Cosmic ray proton plus helium energy spectrum measured by the ARGO-YBJ experiment in the energy range 3-300 TeV,” *Physical Review D - Particles, Fields, Gravitation and Cosmology*, vol. 91, no. 11, pp. 1–18, 2015, ISSN: 15502368. DOI: 10.1103/PhysRevD.91.112017. arXiv: 1503.07136 (cit. on p. 35).
- [111] IPN. (2017). Institut de physique nucléaire orsay web site, [Online]. Available: <http://ipnwww.in2p3.fr/Astroparticules?date=2017-05&lang=en> (cit. on p. 36).

- [112] M. Iacovacci, “Status of argo-ybj: An overview,” *Nuclear Physics B - Proceedings Supplements*, vol. 175-176, pp. 389–394, 2008, Proceedings of the XIV International Symposium on Very High Energy Cosmic Ray Interactions, ISSN: 0920-5632. DOI: <https://doi.org/10.1016/j.nuclphysbps.2007.11.037> (cit. on p. 36).
- [113] B. Bartoli, P. Bernardini, X. J. Bi, *et al.*, “EAS age determination from the study of the lateral distribution of charged particles near the shower axis with the ARGO-YBJ experiment,” pp. 1–26, 2017. arXiv: [arXiv:1707.01412v1](https://arxiv.org/abs/1707.01412v1) (cit. on pp. 36, 37, 72).
- [114] A. Aloisio, P. Branchini, S. Catalanotti, *et al.*, “The trigger system of the argo-ybj experiment,” *Nuclear Science, IEEE Transactions on*, vol. 51, pp. 1835–1839, Sep. 2004. DOI: [10.1109/TNS.2004.832977](https://doi.org/10.1109/TNS.2004.832977) (cit. on p. 36).
- [115] T. Antoni, W. D. Apel, F. Badea, *et al.*, “The cosmic-ray experiment KASCADE,” *Nuclear Instruments and Methods in Physics Research, Section A: Accelerators, Spectrometers, Detectors and Associated Equipment*, vol. 513, no. 3, pp. 490–510, 2003, ISSN: 01689002. DOI: [10.1016/S0168-9002\(03\)02076-X](https://doi.org/10.1016/S0168-9002(03)02076-X) (cit. on p. 37).
- [116] e. W. Apel, J. Arteaga, A. Badea, *et al.*, “The kascade-grande experiment,” *Nuclear Instruments and Methods in Physics Research Section A: Accelerators, Spectrometers, Detectors and Associated Equipment*, vol. 620, no. 2-3, pp. 202–216, 2010 (cit. on pp. 37, 39).
- [117] Karlsruhe Institute of Technology. (2014). Kascade-grande web site, [Online]. Available: <http://www.ikp.kit.edu/kascade/english/index.php> (cit. on p. 38).
- [118] F. G. Schröder, P. A. Bezyazeev, N. M. Budnev, *et al.*, “Overview on the Tunka-Rex antenna array for cosmic-ray air showers,” 2017. arXiv: [arXiv:1708.00627v1](https://arxiv.org/abs/1708.00627v1) (cit. on pp. 39, 41).
- [119] Y. Kazarina, P. A. Bezyazeev, N. M. Budnev, *et al.*, “The Tunka Radio Extension, an antenna array for high-energy cosmic-ray detection,” pp. 18–21, 2017. arXiv: [1701.04727](https://arxiv.org/abs/1701.04727) (cit. on pp. 40, 42).
- [120] The IceCube Collaboration, “Science Case of a Scintillator and Radio Surface Array at IceCube,” *36<sup>th</sup> International Cosmic Ray Conference*, 2019 (cit. on p. 40).
- [121] The LHAASO Collaboration, “Status and first result of LHAASO-WCDA,” *36<sup>th</sup> International Cosmic Ray Conference*, 2019 (cit. on p. 40).
- [122] G. Di Sciascio, “The LHAASO experiment: From Gamma-Ray Astronomy to Cosmic Rays,” *Nuclear and Particle Physics Proceedings*, vol. 279-281, pp. 166–173, 2016, ISSN: 24056014. DOI: [10.1016/j.nuclphysbps.2016.10.024](https://doi.org/10.1016/j.nuclphysbps.2016.10.024). arXiv: [1602.07600](https://arxiv.org/abs/1602.07600) (cit. on p. 41).
- [123] The Telescope Array Collaboration, “Highlights from the Telescope Array experiment,” *36<sup>th</sup> International Cosmic Ray Conference*, 2019 (cit. on p. 41).
- [124] S. Ogio, for the Telescope Array Collaboration, “Telescope Array Low-energy Extension (TALE) hybrid,” *36<sup>th</sup> International Cosmic Ray Conference*, 2019 (cit. on p. 41).

- [125] A. U. Abeysekara et al, “The Sensitivity of HAWC to Steady and Transient Sources of Gamma Rays: Contributions to ICRC 2013,” 2013. arXiv: arXiv:1310.0071v1 (cit. on p. 43).
- [126] M. Mostafa et al, “The High Altitude Water Cherenkov Observatory,” *Proc. of the 33rd ICRC*, 2013. arXiv: arXiv:1310.7237v1 (cit. on p. 43).
- [127] A. U. Abeysekara et al, “The HAWC Gamma-Ray Observatory: Observations of Cosmic Rays,” 2013. arXiv: arXiv:1310.0072v1 (cit. on p. 43).
- [128] A. U. Abeysekara, “The HAWC Gamma-Ray Observatory: Dark Matter, Cosmology, and Fundamental Physics,” 2013. arXiv: arXiv:1310.0073v1 (cit. on p. 43).
- [129] The ANTARES Collaboration, “Antares: The first undersea neutrino telescope,” *Nuclear Instruments and Methods in Physics Research Section A: Accelerators, Spectrometers, Detectors and Associated Equipment*, vol. 656, no. 1, pp. 11–38, 2011, ISSN: 0168-9002. DOI: <https://doi.org/10.1016/j.nima.2011.06.103> (cit. on p. 44).
- [130] D. N. Burrows, J. Hill, J. Nousek, *et al.*, “The swift x-ray telescope,” *Space science reviews*, vol. 120, 2005 (cit. on p. 44).
- [131] A. U. Abeysekara, A. Archer, W. Benbow, *et al.*, “Veritas and fermi-lat observations of tev gamma-ray sources discovered by hawc in the 2hwc catalog,” *Astrophysical Journal*, vol. 866, 24, p. 24, Oct. 2018. DOI: 10.3847/1538-4357/aade4e. arXiv: 1808.10423 (cit. on p. 44).
- [132] L. S. Collaboration, V. Collaboration, *et al.*, “Gwtc-1: A gravitational-wave transient catalog of compact binary mergers observed by ligo and virgo during the first and second observing runs,” *arXiv preprint arXiv:1811.12907*, 2018 (cit. on p. 44).
- [133] B. P. Abbott, R. Abbott, T. Abbott, *et al.*, “Gw170608: Observation of a 19 solar-mass binary black hole coalescence,” *The Astrophysical Journal Letters*, vol. 851, no. 2, p. L35, 2017 (cit. on p. 44).
- [134] B. P. Abbott, R. Abbott, T. Abbott, *et al.*, “Multi-messenger observations of a binary neutron star merger,” *Astrophys. J. Lett*, vol. 848, no. 2, p. L12, 2017 (cit. on p. 45).
- [135] A. Abeysekara, R. Alfaro, C. Alvarez, *et al.*, “Search for tev gamma-ray emission from point-like sources in the inner galactic plane with a partial configuration of the hawc observatory,” *The Astrophysical Journal*, vol. 817, no. 1, p. 3, 2016 (cit. on p. 45).
- [136] A. Abeysekara, A. Albert, R. Alfaro, *et al.*, “Search for very high energy gamma rays from the northern fermi bubble region with hawc,” *The Astrophysical Journal*, vol. 842, Mar. 2017. DOI: 10.3847/1538-4357/aa751a (cit. on p. 45).
- [137] T. C. Weekes, M. Cawley, D. Fegan, *et al.*, “Observation of tev gamma rays from the crab nebula using the atmospheric cerenkov imaging technique,” *The Astrophysical Journal*, vol. 342, pp. 379–395, Jun. 1989. DOI: 10.1086/167599 (cit. on p. 45).
- [138] HAWC Collaboration. (2017). Hawcwiki, [Online]. Available: [http://private.hawc-observatory.org/wiki/index.php/Main\\_Page](http://private.hawc-observatory.org/wiki/index.php/Main_Page) (cit. on pp. 45, 46, 54).

- [139] J. C. Arteaga-Velázquez, Z. Hampel-Arias, and J. D. Álvarez, “Estimate of the energy spectrum of the light component of cosmic rays in HAWC using the shower age and the fraction of hit PMT’s,” *35<sup>th</sup> International Cosmic Ray Conference*, pp. 1–8, 2017 (cit. on pp. 45, 55, 67).
- [140] Z. Hampel-Arias, “Cosmic ray observations at the tev scale with the hawc observatory,” <https://private.hawc-observatory.org/wiki/images/b/b8/HampelThesis.pdf>, PhD thesis, University of Wisconsin-Madison, 2017 (cit. on pp. 45, 50, 52, 53, 55).
- [141] S. Y. BenZvi and D. Fiorino and S. Westerhoff for the HAWC Collaboration, “Observation of anisotropy in the arrival direction distribution of tev cosmic rays with hawc,” *The Astrophysical Journal*, vol. 796, Aug. 2015 (cit. on p. 45).
- [142] A. Abeysekara, A. Albert, R. Alfaro, *et al.*, “Very-high-energy particle acceleration powered by the jets of the microquasar ss 433,” *Nature*, vol. 562, no. 7725, p. 82, 2018 (cit. on p. 46).
- [143] D. Hooper, I. Cholis, T. Linden, *et al.*, “Hawc observations strongly favor pulsar interpretations of the cosmic-ray positron excess,” *Phys. Rev. D*, vol. 96, p. 103013, 10 Nov. 2017. DOI: 10.1103/PhysRevD.96.103013 (cit. on p. 46).
- [144] A. Abeysekara, A. Albert, R. Alfaro, *et al.*, “The 2hwc hawc observatory gamma ray catalog,” *The Astrophysical Journal*, vol. 843, Feb. 2017 (cit. on p. 46).
- [145] A. Abeysekara, A. Albert, R. Alfaro, *et al.*, “Observation of the crab nebula with the hawc gamma-ray observatory,” 2017. arXiv: arXiv:1701.01778v1 (cit. on pp. 46, 51, 53, 61, 71).
- [146] HAWC Collaboration. (2017). Hawcwiki official plots, [Online]. Available: [https://private.hawc-observatory.org/wiki/index.php/Official\\_Plots](https://private.hawc-observatory.org/wiki/index.php/Official_Plots) (cit. on p. 47).
- [147] A. Abdo, A. Abeysekara, B. Allen, *et al.*, “Milagro observations of potential tev emitters,” *Astroparticle Physics*, vol. 57-58, pp. 16–25, 2014, ISSN: 0927-6505. DOI: <https://doi.org/10.1016/j.astropartphys.2014.03.001> (cit. on pp. 48, 49).
- [148] M. F. L’Annunziata, “Radioactivity: Introduction and History,” M. F. L’Annunziata, Ed. Amsterdam: Elsevier Science B.V., 2007, ISBN: 9780444527158 (cit. on pp. 48, 49).
- [149] O. Heaviside, “The electromagnetic effect of moving point charge,” *The Electrician*, vol. 22, pp. 147–148, 1888 (cit. on p. 48).
- [150] O. Heaviside, “On the electromagnetic effects due to the motion of electrification through a dielectric,” in *Electrical Papers*, ser. Cambridge Library Collection - Technology. Cambridge University Press, 2011, vol. 2, pp. 504–518. DOI: 10.1017/CBO9780511983139.020 (cit. on p. 48).
- [151] P. A. Cherenkov, “Visible emission of clean liquids by action of gamma radiation,” *Doklady Akademii Nauk SSSR*, vol. 2, 1934 (cit. on p. 48).
- [152] Frank, I. and Tamm, Ig., “Coherent visible radiation of fast electrons passing through matter,” in *Selected Papers*. Springer Berlin Heidelberg, 1991, pp. 29–35, ISBN: 978-3-642-74626-0. DOI: 10.1007/978-3-642-74626-0\_2 (cit. on p. 48).

- [153] H. Alaeian. (2014). Imagen radiación cherenkov, [Online]. Available: <http://large.stanford.edu/courses/2014/ph241/alaeian2/> (cit. on p. 48).
- [154] J. R. Wood, “An all-sky search for bursts of very high energy gamma rays with hawc,” <https://private.hawc-observatory.org/wiki/images/8/82/WoodThesis.pdf>, PhD thesis, University of Maryland, 2016 (cit. on pp. 49–51).
- [155] M. Gussert, “A spectral analysis of the crab nebula and other sources with hawc,” <http://private.hawc-observatory.org/wiki/images/c/c2/GussertThesis.pdf>, PhD thesis, Colorado State University, 2016 (cit. on pp. 51, 53).
- [156] D. W. Fiorino, “Observation of tev-energy cosmic-ray anisotropy with the hawc observatory,” <http://www.hawc-observatory.org/publications/#thesis>, PhD thesis, University of Wisconsin-Madison, 2015 (cit. on p. 51).
- [157] J. D. Álvarez, U. Cotti, C. de León. (2012). Quickstart guide for aerie v1.16.00. HAWC internal documents, [Online]. Available: [https://private.hawc-observatory.org/hawc.umd.edu/internal/db/2219\\_02.pdf](https://private.hawc-observatory.org/hawc.umd.edu/internal/db/2219_02.pdf) (cit. on p. 51).
- [158] K. Malone. (2018). Energy estimation via ground parameter. HAWC internal documents, [Online]. Available: [https://private.hawc-observatory.org/hawc.umd.edu/internal/db/2328\\_13.pdf](https://private.hawc-observatory.org/hawc.umd.edu/internal/db/2328_13.pdf) (cit. on pp. 54, 70).
- [159] D. Heck, J. Knapp, J. N. Capdevielle, *et al.*, “CORSIKA: a Monte Carlo code to simulate extensive air showers.” 1998, Provided by the SAO/NASA Astrophysics Data System (cit. on p. 55).
- [160] S. Agostinelli, J. Allison, K. Amako, *et al.*, “Geant4 — a simulation toolkit,” vol. 506, pp. 250–303, 2003. DOI: 10.1016/S0168-9002(03)01368-8 (cit. on p. 55).
- [161] Segev BenZvi. (2015). Review of the sweets project in aerie. HAWC internal documents, [Online]. Available: <https://private.hawc-observatory.org/hawc.umd.edu/internal/doc.php?id=2302> (cit. on p. 56).
- [162] John Pretz, Segev BenZvi, Zhixiang Ren. (2013). Simulation weighting. HAWC internal documents, [Online]. Available: <https://private.hawc-observatory.org/hawc.umd.edu/internal/doc.php?id=2302> (cit. on p. 56).
- [163] O. Adriani, G. C Barbarino, G. Bazilevskaya, *et al.*, “Pamela measurements of cosmic-ray proton and helium spectra,” vol. 332, pp. 69–72, Mar. 2011 (cit. on p. 56).
- [164] R. Alfaro, C. Alvarez, J. Álvarez, *et al.*, “All-particle cosmic ray energy spectrum measured by the hawc experiment from 10 to 500 tev,” *Physical Review D*, vol. 96, no. 12, p. 122001, 2017 (cit. on pp. 56, 67).
- [165] HAWC Collaboration. (2017). Fits to direct measurements, [Online]. Available: [https://private.hawc-observatory.org/wiki/index.php/Fits\\_to\\_Direct\\_Measurements](https://private.hawc-observatory.org/wiki/index.php/Fits_to_Direct_Measurements) (cit. on pp. 56–59).
- [166] John Pretz. (2016). Curvature correction. HAWC Collaboration meeting, [Online]. Available: <https://private.hawc-observatory.org/wiki/images/4/44/Hereyourfile6.pdf> (cit. on p. 56).
- [167] Hugo Ayala. (2014). Core fitter analysis. HAWC internal documents, [Online]. Available: [https://private.hawc-observatory.org/hawc.umd.edu/internal/db/2268\\_01.pdf](https://private.hawc-observatory.org/hawc.umd.edu/internal/db/2268_01.pdf) (cit. on p. 59).

- [168] HAWC Collaboration. (2017). Hawc tranches, [Online]. Available: <http://private.hawc-observatory.org/hawc.umd.edu/tranches/> (cit. on p. 65).
- [169] J. C. Arteaga-Velázquez, J. de Dios Álvarez, and J. A. Morales-Soto. (2017). Cosmic ray group call - update on the analysis of the light component of cr's, [Online]. Available: [https://private.hawc-observatory.org/wiki/images/e/eb/HAWC\\_Weekly\\_CollMeet\\_Arteaga\\_7February2017.pdf](https://private.hawc-observatory.org/wiki/images/e/eb/HAWC_Weekly_CollMeet_Arteaga_7February2017.pdf) (cit. on p. 67).
- [170] A. Smith. (2015). Charge errors and pincness v2 (data and algorithms call), [Online]. Available: <https://private.hawc-observatory.org/wiki/images/b/b9/20150602-andy-charge.pdf> (cit. on p. 70).
- [171] R. Raikin, A. Lagutin, and A. Tyumentsev, “Model-insensitive approach to the cosmic ray primary mass composition deduction,” *Nuclear Physics B - Proceedings Supplements*, vol. 196, pp. 383–386, 2009, Proceedings of the XV International Symposium on Very High Energy Cosmic Ray Interactions (ISVHECRI 2008), ISSN: 0920-5632. DOI: <https://doi.org/10.1016/j.nuclphysbps.2009.09.072> (cit. on p. 72).
- [172] R. Coy, G. Cunningham, C. L. Pryke, *et al.*, “The lateral distribution of extensive air showers produced by cosmic rays above 1019 ev as measured by water-čerenkov detectors,” *Astroparticle Physics*, vol. 6, no. 3-4, pp. 263–270, 1997 (cit. on p. 72).
- [173] E. M. Holt, F. G. Schröder, and A. Haungs, “Enhancing the cosmic-ray mass sensitivity of air-shower arrays by combining radio and muon detectors,” *The European Physical Journal C*, vol. 79, p. 371, Apr. 2019. DOI: [10.1140/epjc/s10052-019-6859-4](https://doi.org/10.1140/epjc/s10052-019-6859-4) (cit. on p. 74).
- [174] S. Müller, R. Engel, T. Pierog, *et al.*, “Impact of muon detection thresholds on the separability of primary cosmic rays,” *Astroparticle Physics*, vol. 97, pp. 174–185, 2018, ISSN: 0927-6505. DOI: <https://doi.org/10.1016/j.astropartphys.2017.11.005> (cit. on p. 74).